Balkan Journal of Electrical & Computer Engineering

An International Peer Reviewed, Referred, Indexed and Open Access Journal

www.bajece.com

Development of Short Forms of Scales with Decision Tree Algorithms

E. AYDEMIR and F. KAYSI

Abstract— **Scales or surveys are among the measurement tools developed to measure the perceptions of individuals on specified topics. In some cases, the length of these measuring tools may negatively affect the response rates of individuals towards these tools. In this regard, this study aimed to development of short forms of scales by decision trees algorithms. In this way, it can be provided to design short-form measuring tools that perform similar functions and to increase the rate of responses to measuring tools. In the study, predictions were made with decision trees, which are data mining methods. In this context, analyzes were made with decision trees algorithms to obtain short forms of three scales. According to the results obtained, a high level of correlation was found between scales' short and long forms. Thus, it can be concluded that short forms of scales are suitable for measuring similar purposes. Instead of using scales consisting of 40, 20 and 20 items, expected measurements can be made with at least three and 10 items with appropriate tree algorithms for each scale. Among the suggestions of the study, it is possible to carry out similar studies for frequently used scales. So high participation rates for scales can be obtain.**

Index Terms— **short form scale, decision trees, mobile phone problem use, mobile device addiction, attitude towards learning.**

I. INTRODUCTION

RESEARCHERS need to take some measurements in order to get results on the topics they are curious about. Whether in science or social sciences, it is stated that measurements are among the basic activities of science [1]. In all these processes, developed measuring tools can be used. Sometimes, specially developed methods and equipment are used for the measurement process. In the social sciences, the relationships between the structures are wondered [2]. Thus, individuals' perceptions in targeted dimensions can be measured.

EMRAH AYDEMIR, is with Department of Computer Engineering University of Kirsehir Ahi Evran University, Kirsehir, Turkey,(e-mail: emrah.aydemir@ahievran.edu.tr).

https://orcid.org/0000-0002-8380-7891

FEYZI KAYSI, is with Department of Vocational School of Technical Sciences, Istanbul University-Cerrahpasa, Istanbul, Turkey, (e-mail: fkaysi@istanbul.edu.tr).

https://orcid.org/0000-0001-6681-4574

One of the conditions taken into consideration in the measurement stages is the efficient realization of the measurement. In order to perform an efficient measurement, a strong measurement tool is required [3]. Otherwise, there may be consequences such as cost, time loss and inability to measure at the expected level. Measurement tools in social sciences can be expressed mostly in the form of surveys and scales.

The length and subject of the measuring tool affect the response rates of individuals. Various problems can be encountered during the response of the measuring instruments prepared by individuals. Among these, problems such as individuals not responding to all or some of the measuring tool and being tightened due to the length of the measuring tool can be mentioned. However, shorter scales are generally good because they load less responses to respondents [3]. Despite this, the use of long measuring instruments may cause negative perceptions of individuals towards measuring instruments. For this reason, researchers sometimes try to compensate for undesirable effects on response rates, using material or immaterial incentives [4]. Experimental studies have shown a strong negative linear relationship between survey length and response rates [5]. Sheehan [6] analyzed 31 studies and found small positive relationships between response rates and length of the surveys. As can be seen from this, the long measurement tools may cause the response rates to decrease. This may lead to underrepresentation of views in the target community in studies.

In some studies, it is seen that monetary incentives can be given for increasing the response rates of the measurement tools [5, 7, 8]. With these financial incentives, it is aimed to increase the response rates of the surveys. It should be ensured that the financial incentives to be given will be enough to compensate for long surveys [4]. The measuring tools can be shortened for increasing the response rates. Shorter surveys have a higher response rate than long surveys [9]. In this context, the scales that are thought to be long and that the response rates may be low can be shortened. The 18-item scale developed by Carlson, Kacmar, Wayne and Grzywacz [10] was shortened to six items by Kacmar et al. [11]. As a result of comparison of these two scales, it was concluded that the desired measurements were realized with both scales [12]. A similar study was performed for Smartphone Addiction Scale which developed by Kwon et al. [13]. There are six factors and 48 items in the long version of this scale. The short form of this scale was developed as 10 items by Kwon, Kim, Cho and Yang [14]. It is concluded that long and short forms of the scales can be used for the same

purpose. In addition, researchers use shortened scales to enable respondents to examine more complex models without the risk of fatigue and boredom [15]. In this way, both participants and researchers can be more comfortable with time. Finally, there is a strong correlation between short form scales and long form scales [16]. In other words, the scales in the short form developed have the same function as the ones in the long form.

In academic studies, it is possible to shorten the scales and thus reach better response rates. In this context, methods that can reduce the number of items can be preferred in some scales which are frequently used. Among these methods, it may be possible to reduce the number of items in the scales by using decision trees. The aim of this study is to reveal the short forms of three measuring tools by using decision trees. In this way, higher scale responses can be obtained with shorter scale forms.

II. METHODOLOGY

In the study, analyzes were carried out using the WEKA (Waikato Environment for Knowledge Analysis) program. With the analysis, it is aimed to prepare short forms of three scales. The scales in the short form that will be revealed by the study are personal. The same scale can be shortened to three items for one of the respondents, while it can be shortened to 10 items for the other respondent. This will change according to the responses of the respondent to the items in the scale. As a result, each respondent would have answered the scale with fewer items instead of the long one. In this context, analyzes were conducted for the scales with decision trees algorithms via WEKA software. First of all, an excel file containing each answer given to the questionnaire in one line was created. While each column of this file contains the answers given to the questions, the last column contains the result obtained from the survey. This file was saved as csv extension and added to the Weka program. Correlation coefficient, mean absolute error and root mean squared error formulas were used in the success analysis of the algorithms used.

$$r = \frac{\sum(xy) - \frac{(\sum x)(\sum y)}{n}}{\sqrt{\left(\sum x^2 - \frac{(\sum x)^2}{n}\right)\left(\sum y^2 - \frac{(\sum y)^2}{n}\right)}} \quad (1)$$

$$Mean\ absolute\ error = \frac{\sum_{i=1}^{n}|\hat{\theta}_i - \theta_i|}{n} \quad (2)$$

$$Root\ mean\ squared\ error = \sqrt{\frac{\sum_{i=1}^{n}(\hat{\theta}_i - \theta_i)^2}{n}} \quad (3)$$

$n = number\ of\ samples$
$\theta_i = i\ sequence\ number\ of\ the\ actual\ demand$
$\hat{\theta}_i = i\ sequence\ number\ of\ the\ predicted\ demand$
$i = sample\ order$
$x = real\ value$
$y = predicted\ value$

The first scale included in the study was the Mobile Phone Problem Usage (MPPU) scale developed by Tekin, Güneş and Çolak [17]. This scale has a structure with three factors and 20 items. The aim of the scale is to measure the mobile phone usages of university students. Data of the MPPU scale which used in this study for prediction was applied to 195 participants in the five-likert [18]. The second scale of the study is the Mobile Device Addiction (MDA) scale developed by Yıldırım, Sumuer, Adnan and Yıldırım [19]. This scale has a structure with four factors and 20 items. The purpose of this scale is to measure the mobile device addiction levels of individuals. For using data of this scale in this study, MDA scale was applied to 363 participants in five-likert. The third scale of the study is Attitude Towards Learning (ATL) scale developed by Kara [20]. The scale of ATL has a structure with four factors and 40 items. In order to use the data in the study, the data of the ATL scale was applied to 164 participants in the five-likert [21]. Permission to use was obtained from scale owners via e-mail. Some information about the scales used is given in Table I.

TABLE I
SOME INFORMATION ABOUT SCALES

Scale	Item Count	Participant Count	Likert Type	Mean ± Std.
ATL	40	164	5 point	3.64 ± 0.32
MDA	20	363	5 point	2.93 ± 0.78
MPPU	20	195	5 point	2.43 ± 0.61

III. DECISION TREES

Although statistic is an important tool in the analysis of data, its use is limited in some cases. In such cases, decision trees may require data mining through data analysis methods [22]. With data mining, predictions can be made on the available data for problems. Decision trees are among the most common and effective methods used in creating prediction models through data mining [23]. With the decision tree model, approximate calculation of target functions is provided. With this model, it helps decision makers to determine the factors to be considered in decision making and to determine the relationship of these factors with decision outputs [24]. Most used decision tree methods are C4.5, REP Tree, Random Forest, CART and Logistic Model Tree algorithm [25]. In this study, the M5P, RandomTree and RepTree algorithms, which are used to estimate the numerical results and output the tree structure together with its branches, are used. RandomTree selects a test based on a given number of random features in each node and does not prune. REPTree creates a decision or regression tree using the information gain / change reduction method and melts this error using reduced error pruning. Optimized for speed and ranks values for numerical attributes only once. Using the M5 model, M5P realizes learning and draws the rules.

IV. FINDINGS

M5P, RandomTree and RepTree, one of the decision trees algorithms, were used to prepare shorter forms of OIT, MDA and MPPU scales. In the analysis made through these algorithms, the scales were aimed to function similarly with fewer items. The analysis results obtained in this context also

http://dergipark.gov.tr/bajece

express the effectiveness levels of the short forms of the scales. As a result of the analyzes, the range where the correlation values that can be found and the interpretation status of these ranges are given in Table II.

TABLE II
INTERPRETATION ACCORDING TO CORRELATION COEFFICIENT VALUE RANGES

Correlation Coefficient Value Ranges	Interpretation
between +0.90 and +1.00	Positive Very High Correlation
between +0.70 and +0.90	Positive High Correlation
between +0.40 and +0.70	Positive Normal Correlation
between +0.20 and +0.40	Positive Low Correlation
between 0.00 and +0.20	Positive Very Low Correlation
between 0.00 and -0.20	Negative Very Low Correlation
between -0.20 and -0.40	Negative Low Correlation
between -0.40 and -0.70	Negative Normal Correlation
between -0.70 and -0.90	Negative High Correlation
between -0.90 and -1.00	Negative Very High Correlation

For the scales in the study with Weka software, the M5P, RandomTree and RepTree algorithms are aimed to estimate the average of responses to the scales. The algorithms used give the tree structure formally as well as showing the conditions in the tree branches as output. The results of the algorithms used for the three scales included in the study are given in Table III.

TABLE III
RESULTS OF PREDICTION SUCCESS OF SCALES

Scale	Used Algorithm	Correlation coefficient	Mean absolute error	Root mean squared error
ATL	M5P	0.8689	0.1191	0.1620
	RandomTree	0.7477	0.1720	0.2397
	RepTree	0.5673	0.2085	0.2803
MDA	M5P	0.9857	0.1055	0.1345
	RandomTree	0.8599	0.3207	0.4118
	RepTree	0.8631	0.3078	0.4006
MPPU	M5P	0.9562	0.1382	0.1785
	RandomTree	0.7620	0.3149	0.4187
	RepTree	0.6295	0.3885	0.4862

Table III shows that the highest success rate for all three scales is obtained in the M5P algorithm. MDA and MPPU scales showed higher success rates compared to the ATL scale. However, the 0.86 correlation coefficient of the ATL scale can be interpreted as showing very high success. As a result of the analyzes, tree structures of the scales were revealed. It has been determined that the total number of branches belonging to decision trees is more than 80. Due to the very large and complex shape of the tree node structures, structures were not visually added to the study.

Considering that the main aim of the study is to developing short forms of the scales, there is a need for findings regarding how many items of the scales can show similar results. In this context, Table IV shows predicted least items for participants' responses for short-form of scales.

TABLE IV
NUMBER OF ITEMS ANSWERED BY PARTICIPANTS IN SHORT FORMS OF SCALES

Number of Items	ATL Participant Number	MDA Participant Number	MPPU Participant Number
3	13	0	10
4	31	10	19
5	32	63	55
6	65	84	48
7	7	93	38
8	8	71	20
9	8	38	5
10	0	4	0
Total	164	363	195

Table IV shows the numbers of items that can be answered in the short forms of ATL consisting of 40 items, MDA consisting of 20 items and MPPU scales consisting of 20 items. In this context, it can be seen that the expected measurement for the entire scale can be realized by answering only three items, provided that it starts with the correct item and is produced with the appropriate algorithm for the scale of ATL. The number of items in other forms of the ATL scale as a result of decision trees ranges between four and nine items. It is seen that the expected measurement can be realized by responding at least four items in MDA scale. However, similar measurements can be obtained with the items to be presented to the participants between five and 10 items for the scale. For the MPPU scale, which is the last scale of the study, it is seen that the expected measurement can be realized by responding the participants with at least three items. However, similar measurements can be obtained with the items to be presented to the participants between four and nine items for the scale. The tree algorithm of the MPPU scale is shown in Fig. 1 below. The section that starts with Q indicates the question number, while the section after colon shows the result value. For example, the first question is the 13th question and those who give the answer less than 4.5 for this question are directed to the 17th question. Those who give the answer greater than 3.5 for the 17th question is directed to the 2nd question. Those who give the answer less than 2.5 for the 2nd question is directed to the 8th question. For these people, the 8th question is the last question. Thus, these people complete the survey in 5 questions.

Fig. 1. The tree algorithm of the MPPU scale

V. Discussion

Scales are often used to scale the levels of participants towards a situation that is curious through scientific studies. This purpose is served with the dimensions and items determined in these scales. In some cases, due to the long scales, it may cause participants to never respond, get bored, leave missing, or not respond in a way that fully reflects their perceptions. Financial or immaterial incentives are among the frequently used methods to prevent such negative situations [4, 5, 7, 8]. Short forms of scales can be preferred to reduce the problems caused by the long scales. Because the scales in short form load the respondents less, they are seen better [3]. However, measuring instruments in short form have higher response rates than long measuring instruments [9]. In addition, it was revealed that the desired measurements were successfully completed in the studies conducted with the long and short forms of the scales [12].

Short forms of the scales can be revealed by choosing the appropriate decision tree and determining the appropriate item to start the measurement process. With the responses that users will give to the first item and the next item is determined by the decision tree, measurements can be made with a minimum of three and a maximum of 10 items for the scales in the study. The number of items to be responded may vary to obtain the highest correlated result for the scales. This is a natural situation in which the participants should have different perceptions. The level of Attitude Towards Learning can be revealed through the responses given by the participants to 40 items with the ATL scale's long form. Instead, according to the findings obtained from the study, this measurement can be obtained by responding at least three and at most nine items with the correct algorithm. Similar results can be seen in Kacmar et al. [11] short form of scale with six-item instead 18-item, Kwon et al. [14] short form of scale with 10-item instead 48-item, and Sendjaya et al. [15] short form of scale with six-item instead 35-item. Similar results are valid for the MDA and MPPU scales in the study in order to reveal the highest level of correlation. These scales can also be shortened by selecting the appropriate decision tree and node.

Scales in the study can be shortened between three and 10 items with appropriate nodes in appropriate algorithm. In the literature, scales in the shortened version, which are more flexible and require less time, are recommended [26, 28]. The length of the measuring tools causes the participants to get tired and bored and is defined as an important research obstacle by increasing the potential of response bias [29]. For this reason, it can be stated that the scales carry out the expected measurements with the number of items between three and 10. Because short forms of scales are suitable tools that can be used effectively for the studies to be carried out [30]. In addition, with the short form scales developed, measurements of expected dimensions can be realized in a shorter time [31].

VI. Conclusions and Recommendations

Short forms of scales can been developed with the preference of appropriate tree algorithm and high correlation level. In this way, instead of applying the scales in long form, participants can work with very few items in order to obtain a similar result. Because there is a strong relationship between short and long forms of scales and therefore short forms can be used reliably [16]. Thus, scale studies with shorter form and higher response rate can be done. This gave the appropriate result for all three scales in the study. As a result, instead of applying 20 or 40 item measurement tools to the participants, correct results can be obtained with at least three and 10 items with the appropriate algorithm. The results obtained in the study were shared with the owners of the scales.

References

[1] O. D. Duncan, "Notes on social measurement: Historical and critical", New York: Russell Sage Foundation, 1984.

[2] F. M., Lord, M. R. Novick, "Statistical theories of mental test scores, Charlotte, NC: Infprmation Age, 2008.

[3] R. F. DeVellis, "Scale development: Theory and applications", Sage publications, 2016.

[4] B., Marcus, M., Bosnjak, S., Lindner, S., Pilischenko, & A. Schütz, "Compensating for low topic interest and long surveys: A field experiment on nonresponse in web surveys", Social Science Computer Review, vol.25, pp.372-383, 2007.

[5] P., Edwards, I. Roberts, M. Clarke, C. DiGuiseppi, S. Pratap, R. Wentz, I. Kwan, "Increasing response rates to postal questionnaires: Systematic review", British Medical Journal, vol.324, 2002, pp.1183–1185.

[6] K. Sheehan, "E-mail survey response rates: A review", Journal of Computer-Mediated Communication, vol.6, 2001.

[7] A. H. Church, "Estimating the effect of incentives on mail survey response rates: A meta-analysis", Public Opinion Quarterly, vol.57, 1993, pp.62–79.

[8] F. J. Yammarino, S. J. Skinner, T. L. Childers, "Understanding mail survey response behavior", Public Opinion Quarterly, vol.55, 1991, pp.613–639.

[9] G. Yetter, K. Capaccioli, "Differences in responses to Web and paper surveys among school professionals", Behavior Research Methods, vol.42, 2010, pp.266-272.

[10] D. S. Carlson, K. M. Kacmar, J. H. Wayne, & J. G. Grzywacz, "Measuring the positive side of the work–family interface: Development and validation of a work–family enrichment scale", Journal of Vocational Behavior, vol.68, 2006, pp.131-164.

[11] K. Kacmar, C. Michele, S. Wayne, D. S. Carlson, M. Ferguson, & D. Whitten, "A short and valid measure of work-family enrichment", Journal of Occupational Health Psychology, vol.19, 2014, pp.32-45.

[12] İ. D. Ülbeği, E. İplik, "İş-Aile Zenginleşmesi Ölçeğinin Geçerlik ve Güvenirlik Çalışması", Journal of Business Research-Turk, vol.10, 2018, pp.722-741.

[13] M. Kwon, J. Y. Lee, W. Y. Won, J. W. Park, J. A. Min, C. Hahn, X. Gu, J. Choi, D. J. Kim, "Development and validation of a smartphone addiction scale (SAS)", PloS one, vol.8, 2013b, e56936. https://doi.org/10.1371/journal.pone.0056936

[14] M. Kwon, D. J. Kim, H. Cho, & S. Yang, "The smartphone addiction scale: development and validation of a short version for adolescents", PloS one, vol.8, 2013a, e83558.

[15] S. Sendjaya, N. Eva, I. B. Butar, M. Robin & S. Castles, "SLBS-6: Validation of a short form of the servant leadership behavior scale", Journal of Business Ethics, vol.156, 2019, pp.941-956.

[16] C. Maggiori, J. Rossier, & M. L. Savickas, "Career adapt-abilities scale–short form (CAAS-SF) construction and validation", Journal of career assessment, vol.25, 2017, pp.312-325.

[17] Ç. Tekin, G. Güneş, C. Çolak, "Cep Telefonu Problemli Kullanım (Pu) Ölçeğinin Türkçe'ye Uyarlanması: Geçerlik ve Güvenilirlik Çalışması", Medicine Science, vol.3, 2014, pp.1361-1381.

[18] F. Kaysi, E. Aydemir & M. Yavuz, "Meslek Lisesi Öğrencilerinin Akıllı Cihaz Problemli Kullanımlarının İncelenmesi", X. Uluslararası Eğitim Araştırmaları Kongresi, Nevşehir, Türkiye, Nisan, 2018.

[19] C. Yildirim, E. Sumuer, M. Adnan, S. Yildirim, "A growing fear: Prevalence of nomophobia among Turkish college students", Information Development, vol.32, 2016, pp.1322-1331.

[20] A. Kara, "Öğrenmeye ilişkin tutum ölçeğinin geliştirilmesi", Elektronik Sosyal Bilimler Dergisi, vol.32, 2010, pp.49-62.
[21] M. Dikmen, M. Şimşek, M. Tuncer, "Öğrenme stilleri ile öğrenmeye yönelik tutum arasındaki ilişki", Uluslararası Sosyal Araştırmalar Dergisi, vol.11, 2018, pp.388-400.
[22] T. W. Ryu, C. F. Eick, "A Database Clustering Methodology and Tool", Information Sciences, vol.171, 2004, pp.29-59.
[23] G. G. Emel, & Ç. Taşkın, "Veri madenciliğinde karar ağaçları ve bir satış analizi uygulaması", Sosyal Bilimler Dergisi, vol.6, 2005, pp.221-239.
[24] C. Bounsaythip, & R. R. Esa, "Overview of Data Mining For Customer Behavior Modeling", VTT Information Technology Research Report, vol.1, 2001, pp.1-53.
[25] M. Ç. Aksu, & E. Karaman, "Karar Ağaçları ile Bir Web Sitesinde Link Analizi ve Tespiti", ACTA Infologica, vol.1, 2017, pp.84-91.
[26] B. K. Hamre & R. C. Pianta, "Early teacher–child relationships and the trajectory of children's school outcomes through eighth grade", Child development, vol.72, 2001, pp.625-638.
[27] R. C. Pianta, & M. W. Stuhlman, "Teacher-child relationships and children's success in the first years of school", School psychology review, vol.33, 2004, pp.444.
[28] N. Tsigilis, & A. Gregoriadis, "Measuring teacher–child relationships in the Greek kindergarten setting: A validity study of the Student–Teacher Relationship Scale–Short Form", Early Education and Development, vol.19, 2008, pp.816-835.
[29] A. Anastasi, S. Urbina, "Psychological testing (7th ed.)", Upper Saddle River, NJ: Prentice Hall, 1997.
[30] S. A. Nelemans, W. H. Meeus, S. J. Branje, K. Van Leeuwen, H. Colpin, K. Verschueren & L. Goossens, "Social Anxiety Scale for Adolescents (SAS-A) Short Form: Longitudinal measurement invariance in two community samples of youth", Assessment, vol.26, 2019, pp.235-248.
[31] M. A. Rogers, A. J. Hickey, J. Wiener, N. Heath & R. Noble, "Factor structure, reliability and validity of the Parental Support for Learning Scale: Adolescent Short Form (PSLS-AS)", Learning Environments Research, vol.21, 2018, pp.423-431.

BIOGRAPHIES

EMRAH AYDEMIR Elazig, in 1987. He received the M.S. degrees in computer teaching from the University of Elazig Firat, in 2012 and the Ph.D. degree in informatics from Istanbul University, Turkey, TR, in 2017.

From 2012 to 2015, he was an Expert with the Istanbul Commerce University. Since 2017, he has been an Assistant Professor with the Computer Engineering Department, Kirsehir Ahi Evran University. He is the author of three books, more than 10 articles, and more than 40 conference presentation. His research interests include artificial intelligence, microcontroller, database and software.

FEYZİ KAYSİ Siirt, in 1986. He graduated from Computer Teacher programme from Firat University. His master's degree on Curriculum and Instruction from Firat University, Educational Sciences Institute. His doctorate degree completed on Yildiz Technical University, Social Sciences Institute from 2014 to 2018. From 2010 to 2019, he has been working as a research assistant at the Istanbul University, Vocational School of Technical Sciences. Currently he is an assistant professor at the Istanbul University-Cerrahpasa, Vocational School of Technical Sciences. His research interests are distance education, distance learning, e-learning, qualitative research and vocational training.

Design and Implementation of a Network Based Multi-Axis Motion Control System for Laboratory Studies

Y. GÜVEN and S. ATİŞ

Abstract— **In this study, an open source network based three axis motion control system has been designed and implemented to be used within motion control courses at engineering and technical branches for applicational studies. This system has been developed by using open source code and suitable physical structure for engineering studies. This experimental set has been evaluated by 107 students in related courses which are electrical machines and servo systems. Students have conducted various experiments by using single, two and three axes respectively. These students have been subjected to a Learner Satisfaction Survey which focuses on cognitive, affective and psychomotor extend of experimental studies in the laboratory with the designed motion control system. It has been observed from the results of this survey that learner-centered approach with the experimental set contribute in learning process positively.**

Index Terms— **Brushless motor, servo system, fieldbus, CAN, Multi-Axis Motion.**

I. INTRODUCTION

In the field of industrial automation, multi-axis motion control systems (MAMCS) which have two or more synchronized axis are being used in robotics, CNC, printing machines and industrial plants for cutting and packing processes. Compatibility and integration of these systems are essential for production processes which need fast response and flexibility. In order to achieve best coordination, MAMCS's components should have an appropriate communication environment.

Fieldbus technologies are being used for different industrial applications for communication [1, 2]. The fieldbus is a component that transforms the motion control system into network-based structure. When works on communication and control techniques for motion control system are analysed [3-8], they indicate that some field bus technologies are made for these particular systems. It also shows that these communication technologies are being consistently developed parallel to other technological developments.

YILMAZ GÜVEN, is with Department of Electronic and Automation University of Kırklareli, Kırklareli, Turkey,(e-mail: ylmzguven@hotmail.com).

https://orcid.org/0000-0002-8205-2490

SELÇUK ATİŞ, is with Department of Electrical and Energy, University of Marmara, İstanbul, Turkey, (e-mail: satis@marmara.edu.tr).

https://orcid.org/0000-0002-2912-9487

Besides communication, many other subjects such as power electronics, kinematics, control theory, artificial intelligence, electrical motors and computer programming are also related with the motion control systems. This relationship with many other fields shows that teaching of motion control systems in engineering and other technical branch is really crucial. Especially in electrics, mechatronics and automation engineering, motion control has become one of the main courses.

Previous studies show how important is teaching of motion control. For example, in long distance education, virtual laboratories are really important. Some works on that can be listed as virtual laboratory structure and its development to show delays on a distributed network based motion control system [9], application to the fuzzy control of a DC Motor [10], motor control demonstration laboratory [11], design and installation of a motion control laboratory that was accessible from web for distance education [12], design of a laboratory which users connected from distance and work with actual hardware [13], connecting to a virtual laboratory from multiple location for saving space and time [14], development of a prototype to control low power brushless DC motor from distance location within server-client structure [15], research and study on educational methods of motion control systems courses [16].

It can be seen that the virtual laboratories have been preferred commonly instead of actual working systems. Virtualization is efficient to some point however it is deficient to solve problems that occurs in actual applications. On the other hand, present systems like robotic arms have unique codes that don't allow users for different application. These structures prevent theoretical and practical studies to come together. We believe that building a MAMCS with open source code is going to help getting over these problems.

In this work, a network based three-axial motion control system has been developed by using open source codes. System is shown in Fig. 1 below.
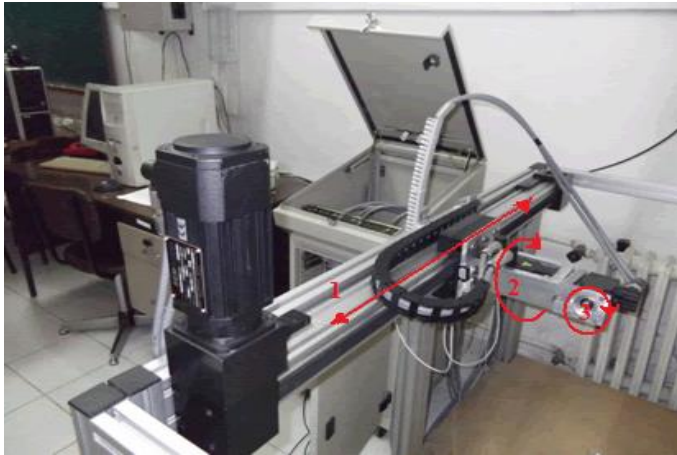
Fig. 1. The network based multi-axial motion control system

The experimental set has brushless servo motors with drivers for each axis and these drivers are being controlled by a network based multi-axis motion controller through CAN-open protocol. Users can access to controller through Ethernet. Controller can be programmed by using a "C" based programming language and it can be accessed through Telnet as well. Motions can be defined for each axis separately for asynchronous motion and interpolation methods can be used for three axial synchronous linear and circular motions. Parameters of the system can be observed over a web browser and they can be graphically recorded.

Driver can be operated with proportional-integral (PI) control techniques in speed-mode and proportional-integral-plus (PIP) control techniques in position-mode. Both techniques can be used together in speed-position-mode and current-control-mode is also active for all these modes. Studies and graphics show that adjusting of parameters of these modes improves stability during applications.

This multi-axial motion control system has been designed to improve success and satisfaction of students in motion control courses as a part of motion control laboratory. A student-centred approach was used in the design and implementation. The students have been subjected to a Learner Satisfaction Survey which focuses on cognitive, affective and psychomotor extend of experimental studies in the laboratory with the designed motion control system. It has been observed from the results of this survey that learner-centred approach with the experimental set contribute in learning process positively.

II. DESGN AND IMPLEMANTATION

A. Design of the system

The designed MAMCS has three axes with different linear and circular motion ability. The most important requirements of a motion control system are speed and stability. Besides that, production cost and compatibility are other important requirements. Due to these requirements, the brushless direct current motors (BLDC) is selected for their high characteristic specifications. These motors are being driven by high performance digital servo drivers. These drives are also

connected to a multi-axis controller for synchronous motions. Communication between drivers and multi-axis controller is established by using CAN-open protocol. Components and connections of network based MAMCS are revealed in Fig. 2.
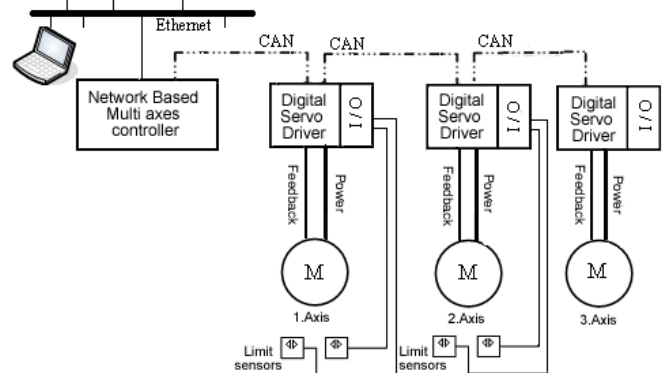

Fig. 2. Components of the MAMCS

The designed mechanical system is defining the main characteristic of the motion. Motion can be continuous or discontinuous as well as it can be linear or circular. Because of that, mechanical system should be designed along with actuator system and sensors. Fig. 3 shows the mechanical system which is designed for different motions both linear and circular. First axis is for converting circular motion of servo motor into linear motion by using high torque geared linear motion module. Second axis is placed with 90° right angle over this module. Third axis is placed over the second one with same 90° angle as well to create a three-axial platform.
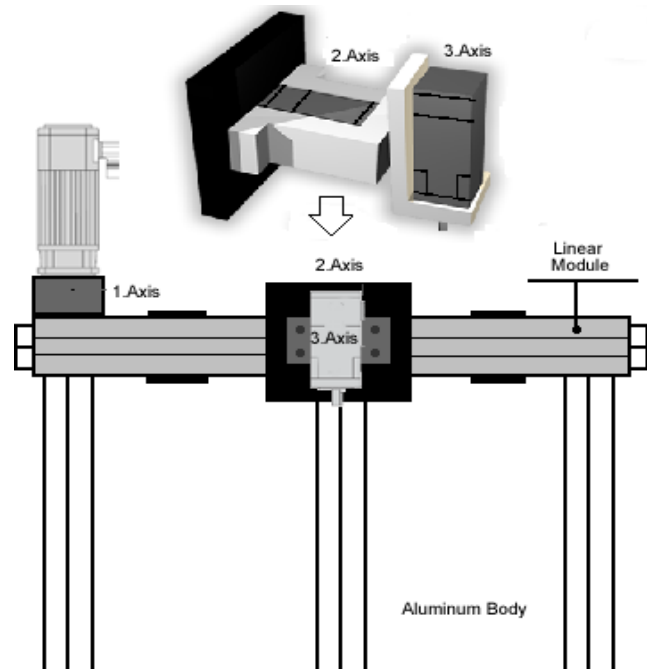

Fig. 3. Schematic of mechanical system.

Because of weight and vibration issues, aluminium material for main body and flexible strap for the linear motion module is preferred. On the other hand, weight of the module and other mechanism highly effective over power consumption of the system and they also effect response times of the system. Fig. 4 shows the linear motion module and its moving force and moment values are given in Table 1 [17].
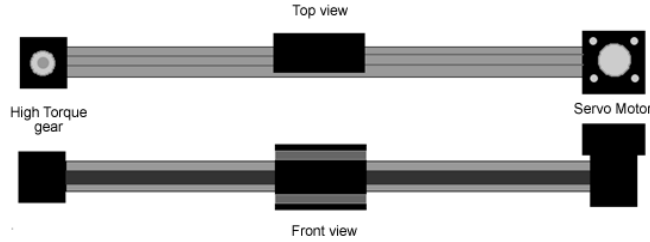

Fig. 4. Top and front view of linear motion module.

Table 1. Dynamic motion values of the linear axis.

	Unit	Value
Fx (Force)	N	650
Fy (Force)	N	400
Fz (Force)	N	1000
Mx (Moment)	Nm	45
My (Moment)	Nm	65
Mz (Moment)	Nm	90
v (Speed)	*m/s*	*3*

As it is shown in Fig. 1 motion platform was placed over aluminium cage and mechanical limits of the system was determined by optical sensors. Placement of optical sensors is shown in Fig. 5.
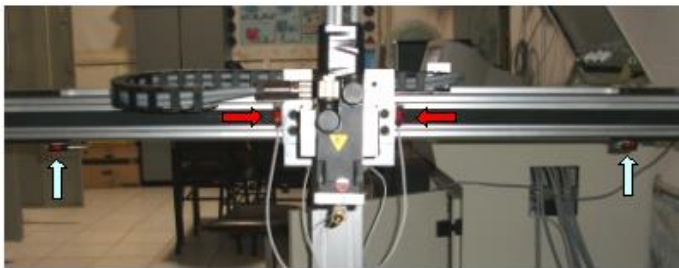

Fig. 5. Optical Sensor placement.

B. Brushless servo motors

BLDC motors are being widely used in motion control systems because of their high-power capacity within small sizes. Their brushless designs improve their stability and service life. They also have low inertia moment and noise level so they are perfect for robotics and motion control systems [18]. Only disadvantage of these motors is that they need high resolution feedback devices and complicated driver circuits for electronic commutation.

Mathematical model for the system has been created by using mathematical model for brushless servo motor. In this model, some values are accepted as constant value such as space between rotor and stator, magnetic interference, sinusoidal electromagnetic force, friction constant and inertia moment. By this mean, mathematical equation for brushless servo motor is written as shown at Equation (1) and block diagram of the motor is also shown in Fig. 6.

$$\begin{bmatrix} \frac{di_d}{dt} \\ \frac{d\omega_m}{dt} \end{bmatrix} = \begin{bmatrix} \frac{-R_a}{L_a} & -K_e \\ \frac{-B}{J} & \frac{1.5K_t}{J} \end{bmatrix}\begin{bmatrix} i_d \\ \omega_m \end{bmatrix} + \begin{bmatrix} \frac{1}{L_a} \\ 0 \end{bmatrix}\cdot V_d + \begin{bmatrix} 0 \\ \frac{-1}{J} \end{bmatrix}\cdot T_1 \qquad (1)$$

Where:

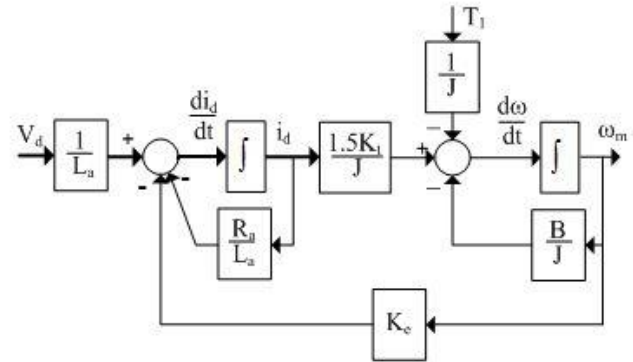|			
i_d	: d-axis current	K_e	: Voltage Constant
V_d	: d-axis voltage	K_t	: Moment Constant
ω_m	: Angular speed	B	: Friction Constant
R_a	: Coil resistance	J	: Motor inertia
L_a	: Coil Inductance	T_1	: Load moment

Fig. 6. The block diagram of brushless servo motor

C. Servo driver

Brushless motors need a driver circuits to operate. These drivers control electronic commutation, current, speed and position of the motor. Beside that they ensure communication and protection duties [19]. We have preferred to use Digital Signal Processor based servo drivers with high resolution encoder feedback. These drivers have fieldbus communication interface onboard and they support CAN open protocol.

D. Multi-Axis motion supervisor

Servo drivers can be connected to a controller for defining synchronous movement with interpolation technique over an open architecture network. We have used a multi-axis motion controller with CAN open protocol support so all device can communicate over an Ethernet network.

E. Communication

CAN open communication protocol is preferred for this system because of its open architecture. This way all servo drivers can be connected to a single network. CAN open is an open source fieldbus technology that is developed for industrial devices. Communication between multi-axis motion controller and servo drivers has been established by using CAN open protocol. Devices have been connected to each other with line topology and each device has a different node address.
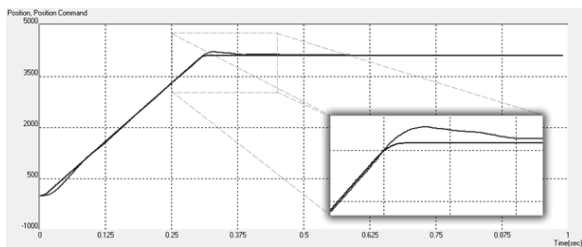
F. System tunings

Before defining movement of the axis, initial parameters of the drivers such as proportional (Kp) and Integral gain (Ki) can be assigned by some experiments. For this purpose, the motors have been operated in current, speed and position control mode, respectively. Kp, Ki and other system parameters were tuned in this process. System's responses to input commands have been observed graphically. Motor's response of third axis is shown in Fig. 7.

System parameters have been set to get best response, apex point, rising and settlement time. In this point, the most important thing is that system can be set according to applicational requirements such as precision, speed and stability. While determining these parameters, effect of each axis should be also considered in multi-axis motion control systems.
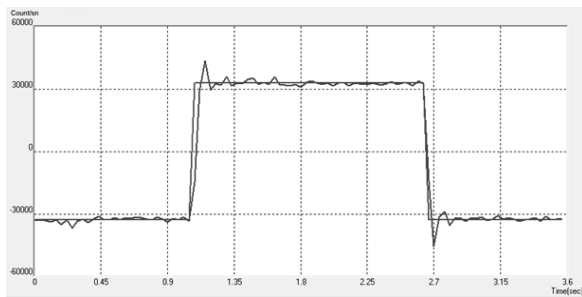
(a)

(b)

Fig. 7. Response of the system after tunings

a) speed   b) position

III. EXPERIMENTS

The experimental set have been evaluated by 107 students in laboratory of motion control systems. Characteristic of these participants can be seen on Table 2 below. As can be seen on the table 2, two different courses which both have application related to servo motors and motion control were subjected to this study. The method was "Experiment in six steps" that is a learner-centred approach as following:

1. In first week, students are informed about the teaching strategies according to learning outputs of the course in the laboratory.
   - Experiment groups consist of 3 students
   - Establishment of a discussion environment between students and teaching staff during the experiment.
   - Preparation and submission of the experiment report as a group.
   - Discussion of the experiment results as a group.

2. The students are informed about experiment, laboratory report paper and research topics related to the experiment on the web page.

3. A quiz exam that consist of question about research issues and job security is carried out.

4. Application and experiment.

5. After one week from experiment date, the report is delivered to the lecturer. The report is discussed between groups and teaching staffs. Discussion consists of question and answer covering the whole experiment. Preparation of the report as a group is essential.

6. The total score of a student is sum of four different evaluations (quiz exam, performance during the experiment, group score and presentation score of the experiment report)
All the stated steps above have been carried out for each experiment in the laboratory. A survey was also applied to measure the effects of the "Experiment in Six Step" approach over students.

Table 2. Participant characteristics.

Course	Participant	Sex	Age	Program	Department
Control of Electrical Machinery	97	10 Female 87 Male	19-22	Associate degree Bachelor's degree	Electrical and Energy
Brushless Servo Motors	10	10 Male	23-25	Master's degree	Electrical Eng.

IV. RESULTS AND DISCUSSIONS

PI parameters of the system can be seen at Table 3. These values have been determined while tuning process. They may be changed according to application needs. These parameters are stored in controller's gain table block. Proportional and integral gains are divided by DC voltage value because of PWM duty cycle. This means DC voltage value is used for current controller's gain as well [20]. That is why gain values are high at Table 3.

The students have performed single, two and three axes motion control experiments in the laboratory. Since single axis motion control is the first step of multi-axis motion control, experiments with single axis were excluded in the article.

Table 3. PI parameters for three axes

Axis	Name	Proportional gain (K_p)	Integral gain (K_i)
1	a1	12.618	14363
2	a2	6.581	11657
3	a3	6.782	12257

The next experimental application with MAMCS was two-dimensional interpolated circular movement. Before the experiment some parameters such as synchronization time, maximum acceleration and deceleration values, maximum and minimum speed, smoothness and operation mode should be set. After these settings, a circular movement was defined by its radius, starting angle and trajectory. Fig. 8 shows that a1 as y-axis and a3 as x-axis for this interpolated circular movement. Position changes and position errors of these two axes are shown in Fig. 9.
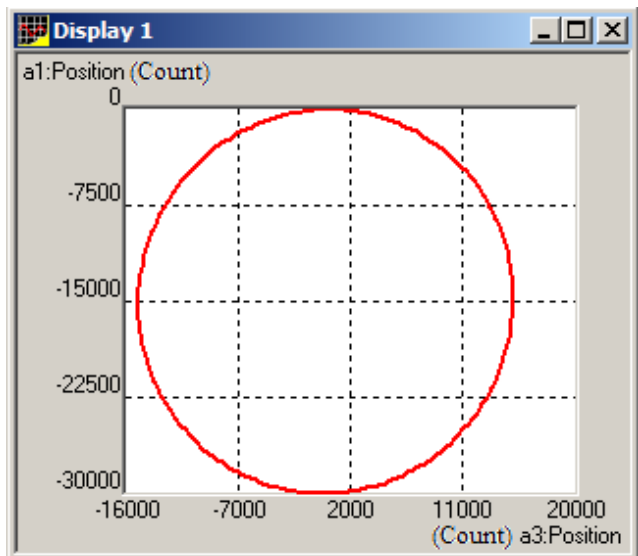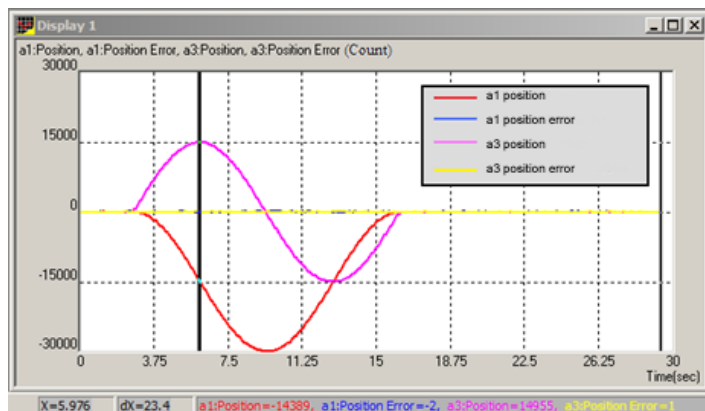

Fig. 8. Circle trajectory.

Fig. 9. The position and position error of the a1 and a3 axis for circle trajectory.

Another experiment with MAMCS was creating a three-dimensional vector with linear interpolation. Same parameters such as synchronization time, maximum acceleration and deceleration, maximum and minimum speed, smoothness and operation mode have set for this movement as well. Two different trajectories have been defined for this linear movement as it is shown at Table 4.

Table 4. The trajectory plane of three-dimensional linear interpolation.

Axis No	Axis Name	Starting Trajectory (Count)	First Target Trajectory (Count)	Second Target Trajectory (Count)
1	a1	0	15000	0
2	a2	3850	-3000	0
3	a3	0	3000	0

Different experiments have been conducted by using different axes. Fig. **10** shows that a1 as x-axis and a2 as x-axis, Fig. **12** shows that a1 as y-axis and a2 as x-axis and Fig. **14** shows that a1 as y-axis and a3 as x-axis for changing linear position. Fig. 11, Fig. **13** and Fig. **15** show position and position errors of a1, a2 and a3. These figures show that position errors for all three axes are very small.
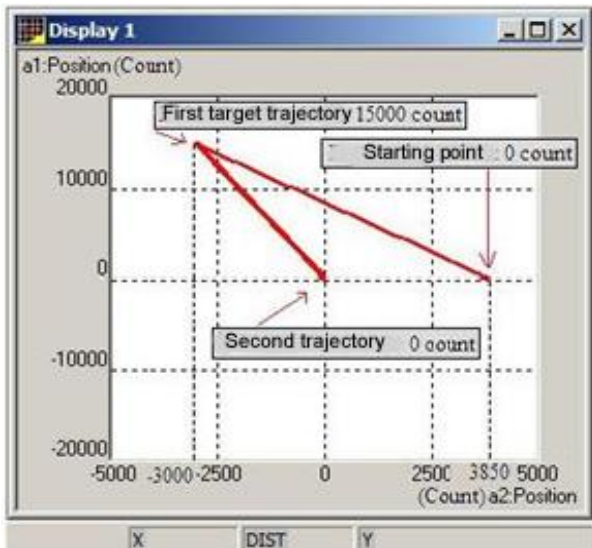
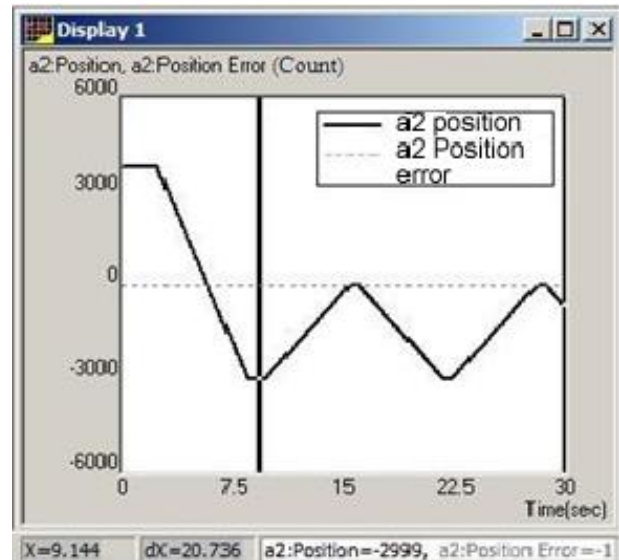**Fig. 10.** The line trajectory of the a1-axis.

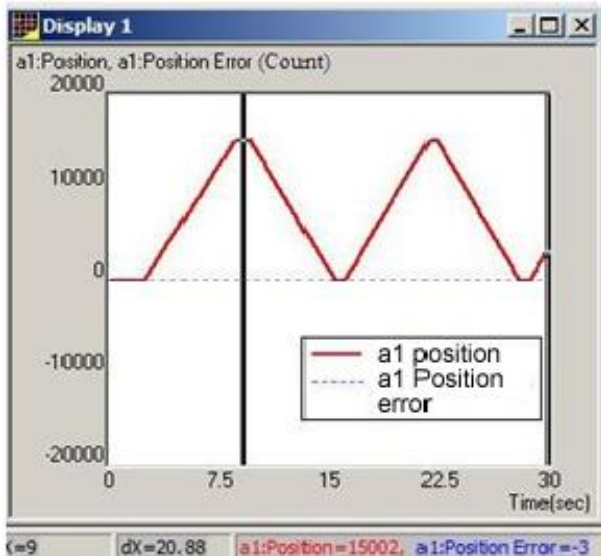**Fig. 13.** The position error and position of the a2-axis.

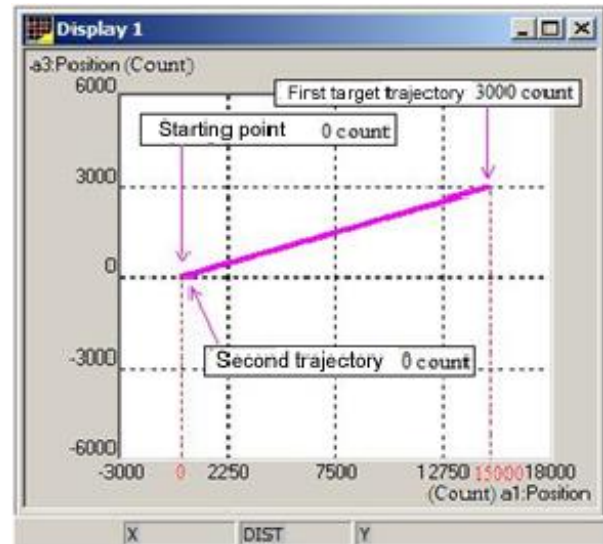**Fig. 11.** The position error and position of the a1-axis.

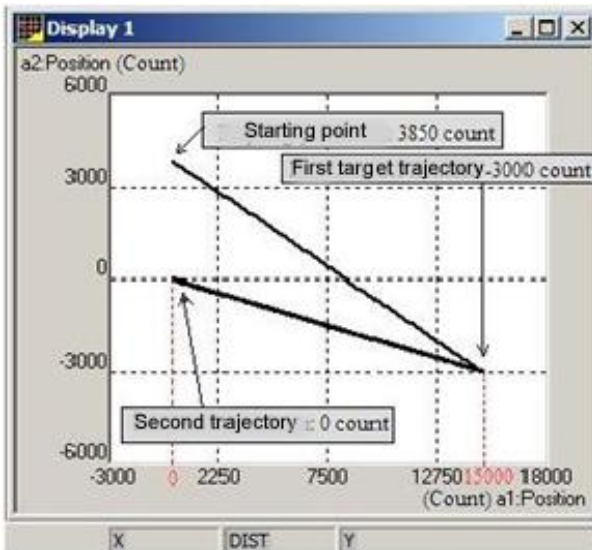**Fig. 14.** The line trajectory of the a3-axis.

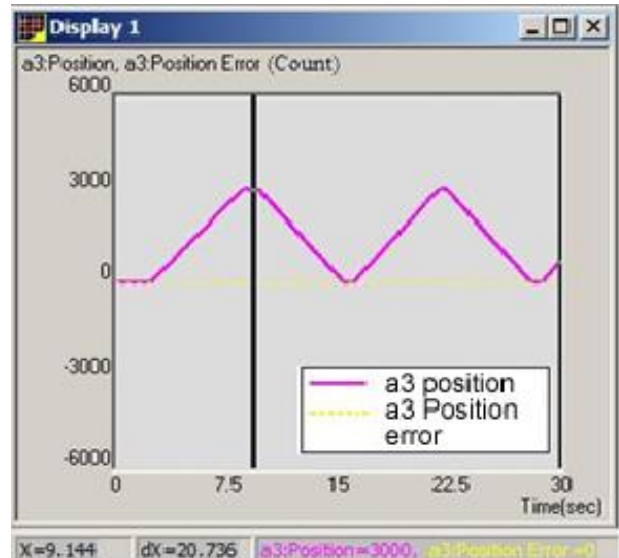**Fig. 12.** The line trajectory of the a2-axis.

Fig. 15. The position error and position of the a3-axis.

The last experiment with MAMCS was defined movement trajectory for each axis separately. Application defined in real-time and movement of each axis synchronized. In trajectory planning, parameters like operation modes, speed, acceleration and deceleration, delay time and target trajectory points have been set. Result of this application is revealed in Fig. 16. It shows position commands and errors of all three axis. Graphical data indicates that system settings of MAMCS can be set up within experimental works. This way system works more efficiently and steady compatible with the mechanical system. Accuracy of the systems can be improved by performing different experiments.

The learner-centred approach and the effect of the experimental set on learning process have been measured by questionnaire. Before the survey,

- Single, biaxial and triaxial motion experiments have been conducted. (Excuse week was announced for those who cannot participate on time)
- A technical trip was organized to the production band consisting of robotic arms for Mechatronic engineering students. (Trip were carried out in 5 groups)

A total of 21 question were asked to the students. Students have answered all question on the survey and the result of this survey can be seen through table 5 to 8.
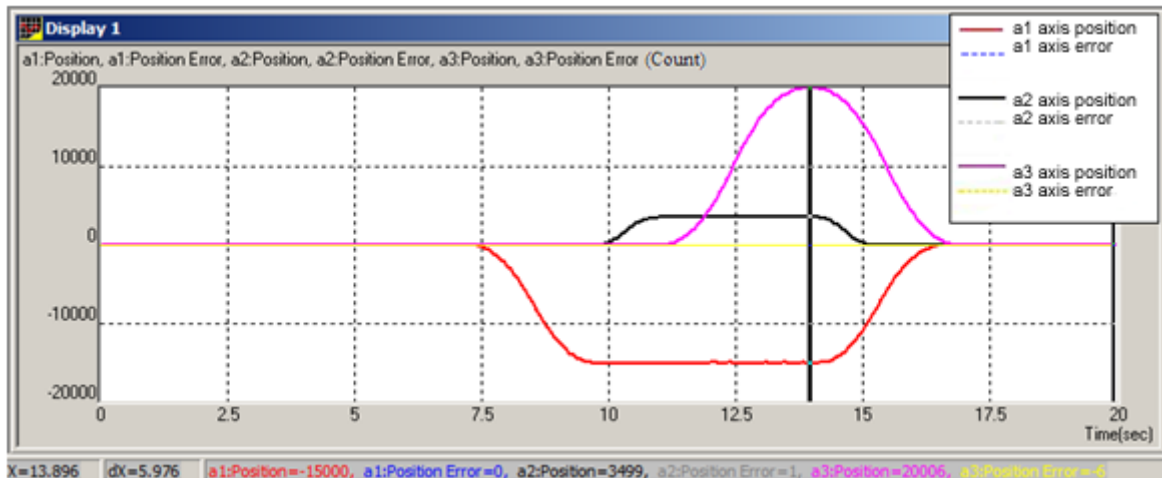

Fig. 16. The position and position error of the a1-a2-a3 axis for the line trajectory.

Table 5. Results of the learner satisfaction questionnaire 1.

Questions (About the "Experiment in six steps" approach)	Agree	Undecided	Disagree
1." Experiment in six steps" approach showed the importance of continuity in learning process.	83%	14%	3%
2." Experiment in six steps" approach has increased my motivation in the laboratory.	86%	10%	4%
3." Experiment in six steps" approach has increased awareness in the laboratory.	87%	10%	3%
4." Experiment in six steps" approach showed the importance of sharing task in a professional group work.	87%	9%	4%
5." Experiment in six steps" provided clear and understandable documents	90%	4%	6%

Table 6. Results of the learner satisfaction questionnaire 2.

Questions (During experiments)	Agree	Undecided	Disagree
6. The physical structure of the system is open for user and establishment of the system as a group work is the basis for engineering applications.	95	5%	-
7. The system has open source code and programming the system in a group work were basis for engineering applications.	93	7%	-
8. The relationship between theory and application is clear because of open source codes and physical structure of the system.	96	4%	-

Table 7. Results of the learner satisfaction questionnaire 3.

Question (after experiments)	1 axis	2 axes	3 axes
9. I prefer …………… motion control experiment to understand the brushless servo motor system.	84%	4%	12%
10. I prefer ………….. motion control experiment to explain brushless servo motors.	85%	4%	11%
11. ……………… motion control experiment affected my learning performance more positively.	12%	8%	80%
12. ………… motion control experiment increased my motivation to lesson and the laboratory.	11%	8%	81%
13. …………. motion control experiment makes me understand the importance of task sharing in group work.	6%	4%	90%
14. After ………… motion control experiment, I can combine the axis.	3%	5%	92%
15. After …………. motion control experiment, I can connect drivers and controller in a multi-axis system.	3%	3%	94%
16. After …………. motion control experiment, I can do linear and circular trajectory planning.	4%	4%	92%

Table 8. Results of the learner satisfaction questionnaire 4.

Questions (About after the experiments and technical tour)	1 axis	2 axes	3 axes
17. I prefer ……… motion control experiment to explain the robotic systems.	3%	4%	93%
18. I prefer ……… motion control experiment to plan a robotic system.	9%	2%	89%
19. I prefer ……… motion control experiment to apply a robotic system.	5%	3%	92%
20. I prefer ……… motion control experiment to interpret a robotic system.	5%	2%	93%
21. I prefer ……… motion control experiment to analyse a robotic system.	4%	3%	93%

Although the "Experiment in six steps" approach led students to a challenging work process, they adopted and found it acceptable for education. That is obvious from the result of the survey (Table 5). This process is up to learner's understanding of importance of continuity, increasing of the motivation and performance of the lecturer.

When the literature is examined, it has been seen that the laboratory of motion control systems was virtual or physically closed to users. This study has shown that the experimental set can easily be used by the students in the laboratory unlike the experiment set in the literature. Table 6 shows the ease of use regarding to experiment set as follows:

- Open source code programming,
- Being physically open to user,
- Studying as a group,
- Students can use their skills and abilities by themselves.

Moreover, the experimental set is completely user-friendly and it reduces the uncertainties to establish strong relationship between theory and practice.

Particularly, it has been understood that observation of robotic system in the technical touring plays a leading role in design and implementation of multi-axis motion control systems as industrial applications. Indication of this guidance can be explained by the fact stated in the previous paragraph and opinions of the students can be seen on table 8.

The result of the survey has shown that single axis experiments were more useful in understanding the theoretical basis of brushless motors and servo systems. Starting with single axis experiment increases the comprehensibility of the subject. On the other hand, it has been seen that multi-axis experiments were more useful to understand the theoretical basis of multi-axis motion control systems and their industrial application such as CNC machines and robotics. The system can be operated within various industrial modes and students can perform single or multi-axis motion control experiments with interpolation techniques. These abilities play a trigger role in the development of the skills over the students. The preference of the students has been shown in table 7.

V. CONCLUSION

In this study, an experimental set has been developed to provide a strong link between theoretical knowledge and application in laboratory of motion control system for engineering and other technical branches. The designed network based multi-axis motion control system is suitable for engineering studies and it has physically visible structure and open source code programming.

This user-friendly open source system has been adopted by the students. It has been found that experimental studies with the system are useful for understanding the theoretical basis of multi-axis motion control systems such as CNC machines and robotic arms. The students will not encounter with such a system which is totally open for user both hardware and software. In this point, it is necessary to avoid using completely closed pre-set systems.

The "Experiment in six steps" approach has influenced the motivation of students positively and provided continuity for the experimental process. The awareness and sense of responsibility has increased in the laboratory. The results of the "Experiment in six steps" approach have been questioned by a survey and it has been observed that the experimental set has contributed positively to the cognitive, psychological and psychomotor dimensions of the learning process.

ACKNOWLEDGMENT

REFERENCES

[1]   W. Haifang, R. Yu, L. Shengtao, and C. Jinhua, Fieldbus technology and rolling process automation, *Computer Design and Applications (ICCDA), 2010 International Conference on*, 25-27 June 2010, 2010, pp. 73-76.

[2]   Y. Bian, X. Xu, and L. Zhu, Variable frequency hydraulic speed control system based on CANopen, *Education Technology and Computer (ICETC), 2010 2nd International Conference on*, 22-24 June 2010, 2010, pp. 264-268.

[3]   J. Yang, Z. Y. Liu, X. Bi, and Y. Sun, 'The Research and Design of High Precision Contour Machining for Multi-Axis Motion Control', *2015 Chinese Automation Congress (CAC)*, 2015, pp. 1594-1599.

[4]   C. L. Lin, W. H. Chu, and W. Gai, Research on the Synchronization Motion Control Technology for Multi-axis System, *2016 Ieee Information Technology, Networking, Electronic and Automation Control Conference (Itnec)*, 2016, pp. 672-679.

[5]   S. Vitturi, L. Peretti, L. Seno, M. Zigliotto, and C. Zunino, Real-time Ethernet networks for motion control, *Computer Standards & Interfaces*, **33**(5), 2011, pp. 465-476.

[6]   M. R. Jathar, RS-485 based multi axis motor controller, *Electronics Computer Technology (ICECT), 2011 3rd International Conference on*, 8-10 April 2011, 2011, pp. 104-106.

[7]   G. GuoYing, Z. LiMin, X. Zhenhua, and D. Han, Design of a Distributed Multiaxis Motion Control System Using the IEEE-1394 Bus, *IEEE Transactions on Industrial Electronics*, **57**(12), 2010, pp. 4209-4218.

[8]   C. Bing, C. You-Ping, X. Jing-Ming, Z. Zu-De, and S. Ji-Ming, Control methodologies in networked motion control systems, *Machine Learning and Cybernetics, 2005. Proceedings of 2005 International Conference on*, 18-21 Aug. 2005, 2005, pp. 1088-1093.

[9]   O. Mirabella, M. Brischetto, and A. Raucea, A network based virtual lab for motion control applications, *Advanced Motion Control, 2008. AMC '08. 10th IEEE International Workshop on*, 26-28 March 2008, 2008, pp. 342-347.

[10]   M. Valles, J. L. Diez, J. L. Navarro, and A. Valera, Remote Access to MATLAB-based Laboratories: Application to the Fuzzy Control of a DC Motor, *International Journal of Engineering Education*, **26**(6), 2010, pp. 1343-1353.

[11]   J. Sibigtroth and E. Montanez, Motor control demonstration lab, *International Journal of Engineering Education*, **21**(1), 2005, pp. 84-93.

[12]   A. Rojko, D. Hercog, and K. Jezernik, Power Engineering and Motion Control Web Laboratory: Design, Implementation, and Evaluation of Mechatronics Course, *IEEE Transactions on Industrial Electronics*, **57**(10), 2010, pp. 3343-3354.

[13]   M. A. Vogelsberger, P. Macheiner, P. Bauer, and T. M. Wolbank, Drives and Motion Control Teaching based on Distance Laboratory and Remote Experiments, *Journal of Power Electronics*, **10**(6), 2010, pp. 579-586.

[14]   N. Zhibo, W. Kexin, and D. Chao, Modeling Virtual Laboratory of Motion Control, *Computing, Communication, Control, and Management, 2008. CCCM '08. ISECS International Colloquium on*, 3-4 Aug. 2008, 2008, pp. 203-205.

[15]   T. Kikuchi, T. Kenjo, and S. Fukuda, Remote laboratory for a brushless DC motor, *Education, IEEE Transactions on*, **44**(2), 2001, p. 12 pp.

[16]   G. Lin and C. Fengjun, Research and Discussion on Teaching Methods of Motion Control Systems Course, *Circuits, Communications and System (PACCS), 2011 Third Pacific-Asia Conference on*, 17-18 July 2011, 2011, pp. 1-4.

[17]   Catalog- Linear Modules, Mekatronik Robotik ve Otomasyon Teknolojileri Tic. ve San. Ltd. Sti., 2007.

[18]   P. Ki-Hong, K. Tae-Sung, A. Sung-Chan, and H. Dong-Seok, Speed control of high-performance brushless DC motor drives by load torque estimation, *Power Electronics Specialist Conference, 2003. PESC '03. 2003 IEEE 34th Annual*, 15-19 June 2003, 2003, pp. 1677-1681.

[19]   Y. Guven, Three Axial Motion Control with Fieldbus, Master, University of Marmara, 2010.

[20]   Elmo Motion Control Ltd, http://www.elmomc.com, Accessed September 2018.

BIOGRAPHIES

YILMAZ GÜVEN İstanbul, in 1981. He received the B.S. and M.S. degrees in Electrical Education from the University of Marmara, İstanbul, in 2010 and the Ph.D. degree in Electrical Education from Marmara University, İstanbul, in 2018.

From 2012 to 2019, he was a Lecturer with the Vocational School of Technical Science in University of Kirklareli. Since 2019, he has been an Assistant Professor with the Electronic and Automation Department, Kırklareli University. He works on embedded system, data analyses, automation system and electrical machines.

SELÇUK ATİŞ Üsküdar, İstanbul, in 1970. He received the B.S. and M.S. degrees in Electrical Education from the University of Marmara, İstanbul, in 1997 and the Ph.D. degree in Electrical Education from Marmara University, İstanbul, in 2007.

From 1994 to 1998, he was a Research Assistant with the Marmara University. From 1998 to 2009, he was a Lecturer with the Marmara University Since 2009, he has been an Assistant Professor with the Electrical and Energy Department, Marmara University. He works on smart lightning system, expert system and embedded devices.

Damage Detection in Ceramic Materials Using Bicoherence Analysis

O. AKGUN

Abstract— **In this study, Bicoherence method was applied to analyze the state of 6 ceramic plates made from the same material is cracked or not. Of all six plates, while 1 consisted of an undamaged plate, the other 5 comprised of cracked plates. Cracks in damages plates have non-identical deformations. The centre points of the plates were applied to shock at equal severity by means of the pendulum. The sound, which emerged as a result of the impact, was recorded and transferred to the data processing environment. A single bicoherence peak was observed at the centre of the durable plate and more than one peak was seen in the cracked plates by the analysis conducted, in addition, their magnitudes were so much smaller than those of durable plates. While large rising magnitudes were formed at the centre on the bi-coherence plane of the durable ceramic plate, more than one bicoherence peaks, with low magnitudes, were formed on the cracked ceramic plates. Differentiation and feature extraction can clearly be identified in the feature diagonal slice analysis of the cracked plates with the bicoherence analysis carried out. While maximum bicoherence coordinates were formed in the coordinate centre of the durable ceramic plate, deviation from the centre presented itself in the cracked ceramic plates.**

Index Terms— **Acoustic vibration method, Bicoherence, Ceramic Plate, Crack Analysis.**

I. INTRODUCTION

Ceramic materials were acquired from the inorganic components and their raw materials consist of clay and its derivatives [1]. Nowadays, ceramic materials are frequently used in industrial and structural product applications [1,2]. They take shape by applying heating and cooling processes during the production stage. They display demeanour hard, brittle, chemically corrosion-resistant, and insulating in terms of electrical and thermal features [3,4]. They are also resistant to high temperatures, lighter than other materials and their raw materials are plentifully and economically found in nature [1,2,5]. In addition to all these advantages, ceramic materials gain brittleness due to baking processes. Cracking and

OMER AKGUN, is with Department of Computer Engineering University of Marmara, Istanbul, Turkey,(e-mail: oakgun@marmara.edu.tr).

https://orcid.org/ 0000-0003-3486-2197

breakage are their most important drawback due to this feature. Their electrical and thermal insulation is high, chemically stable and has high melting temperatures. However, the provision of raw materials is easy and economical, they also have low production costs and their usage and processing are quite easy [3-7].

The biggest risks in ceramic production are deformations and cracks as a result of improper stacking and storage of ceramic materials. These deformations and cracks cannot be distinguished when covered by enamel and they only turn into marketing problems with feedbacks by users. Many marker-based different methods are being used in the determination of micro-cracks and deformations occurring in ceramics [1,8,16]. Mark-based works, used by developing an acoustic measurement method, have been quite effective in determining deformations [1-4]. In this study, data, taken from the measurement system developed by Akinci [1], were analyzed by using the bicoherence method.

II. EXPERIMENTAL MEASUREMENT AND DATA COLLECTION SYSTEM

Testing set, developed by Akinci [1], was used in this study and the data were obtained from this testing set. The pendulum was used in order to produce an impact on experimental measurement and data collection systems [1,12]. The experimental application was designed within the framework of the analysis of sound resulting from a pulse effect. The pendulum in the pendulum was collected and recorded by the sound data acquisition system spreading to the environment as a result of the impact on the ceramic plate [1-4, 17,18].
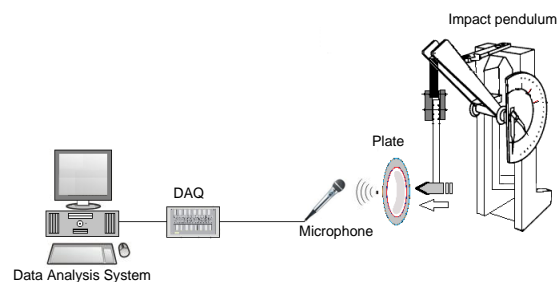

Fig.1. Data acquisition and measurement systems [1-4]

The POE 2000 type Impact Pendulum was used in the experimental data collection system. Impacts in the same

severity were applied to the ceramic plates of the same type and model through pendulum and the sound data, which emerged as a result of the impact, had been recorded. The output audio signal of the amplifier is transmitted to the computer at a sampling rate of 0.00001 seconds via Advantech 1716 L Multifunction PCI card and data processing is performed by using Matlab © (Fig. 1) [1-4,18].

III.   BI-COHERENCE

The phase relationships between frequency components are not taken into consideration in signal processing techniques which utilize from second-order statistics and/or power spectrum. Therefore, these techniques are blind against the phase information. Also, the second-order statistics and power spectrum are not enough to define the non-Gaussian process completely in terms of statistics. In recent years, studies on high-order statistics and power spectrum have been conducted in order random processes to be defined more delicately and phase information to be processed [19].

The second-order statistics, like autocorrelation and power spectrum, are quite effective in the analysis of gauss, static and linear processes. The higher-ordered statistics are used in the examination of gauss, static and non-linear processes and in the attainment of significant results. In other words, a random process, like Gaussian distribution X(n), can be completely defined by autocorrelation function (ACF). ACF is not enough for non-Gaussian processes. Therefore, more information can be obtained from these processes with HOS. While the first-degree torque was given in Equation (1), the second-degree torque and autocorrelation were given in Equation (2) [19,20].

$$m_X = E(X), \ \sigma_X^2 = E\left[\left(X - m_X\right)^2\right] \tag{1}$$

$$m_X^2(i) = E\{X(n).X(n+i)\} \tag{2}$$

The higher-ordered statistics can be found by calculating with higher degree torques like (m3, m4…). The non-linear combinations of these higher degree torques can be defined as (c1, c2, c3…) cumulant. The third-level torques were given in Equation 2. The collective equation for the zero-mean process was given in Equations 4,5 and 6 [20].

$$m_X^3(i, j) = E\{X(n).X(n+i).X(n+j)\} \tag{3}$$

$$c^2(i) = m(i) \tag{4}$$

$$c^3(i, j) = m(i, j) \tag{5}$$

$$c^4(i,j,k) =$$
$$m^4(i,j,k) - m^2(i).m^2(j,k) - m^2(j).m^2(i,k) - m^2(k).m^2(i,j) \tag{6}$$

Torques provide more accurate results in the analysis of deterministic signals, whereas cumulative provides more accurate results in the analysis of random signals. If the power spectrum of random signals is defined by DFT in Equation (7);

$$P_2^x(f) = DFT(C_2^x(m).e^{-j2\pi nf} \tag{7}$$

Bispectrum reveals signals resulting from the non-linear process in addition to suppressing Gaussian probability distribution of events. The cumulative spectrum of 3rd degree is called bispectrum and is shown in Equation (8). The signal is real-valued stationary random process is shown as follows [21,22].

$$B^x(f_1, f_2) = \sum_{m=-\infty}^{\infty} \sum_{n=-\infty}^{\infty} C_3^x(m,n).e^{-j2\pi(mf_1+nf_2)} \tag{8}$$

$$B(w_1, w_2) = X(w_1).X(w_2).X^*(w_1 + w_2) \tag{9}$$

Unlike the power spectrum, in addition to presenting information on non-linear or gauss distributed non-indicated data, bispectrum also provides the phase information of the sign as an important feature. Peaks in bispectrum show frequency components and phase overlap in the signal. While peaks with two same frequencies show the frequency components in the signal, peaks with different frequencies indicate that there is a phase conflict in these frequencies. For the special case in which w1 and w2 are equal, the diagonal slices (DS) of one-variable bispectrum is given in Equation (10) [21,24].

$$B(w) = X^2(w).X^*(2w) \tag{10}$$

The system, which was located between input and output signals of the coherence, has linearity deviation measurement, it is a size based on the calculation of a cross-spectrum and two auto-spectra and is shown as in Equation (11). Bicoherence is the energy ratio of a single sign-on any two frequencies. In other words, it is the quadratic normalized version of the bispectrum. It can be expressed by Equation (12) [21,24].
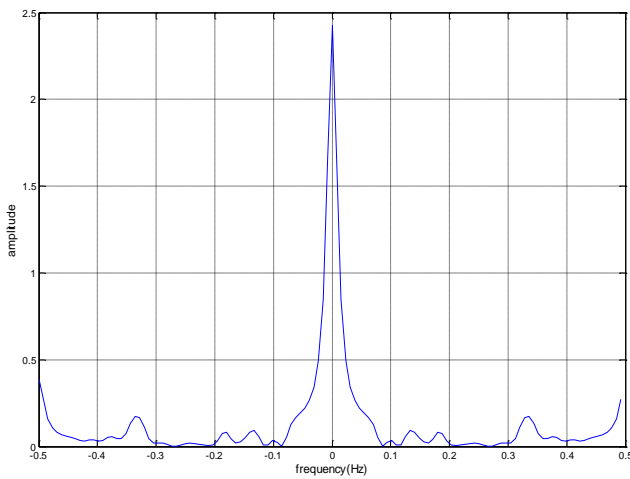
$$C_{XY}(f) = \frac{\left|P_{xy}(f)\right|^2}{P_{xx}(f)P_{yy}(f)} \tag{11}$$

$$Bic(f_1, f_2) = \frac{B(f_1, f_2)}{\sqrt{P(f_1)P(f_2)P(f_1 + f_2)}} \tag{12}$$

IV.   APPLICATION OF METHODS
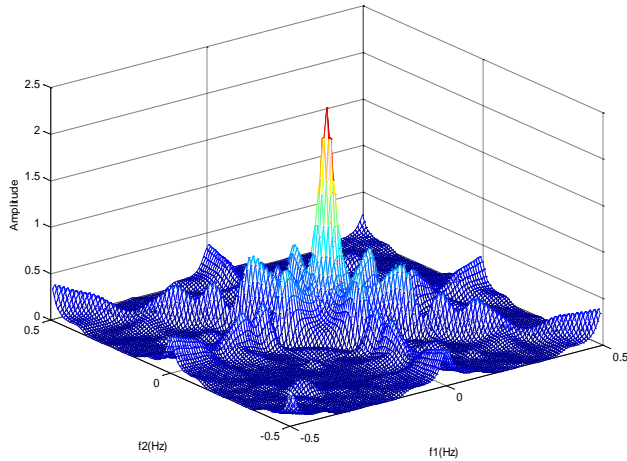
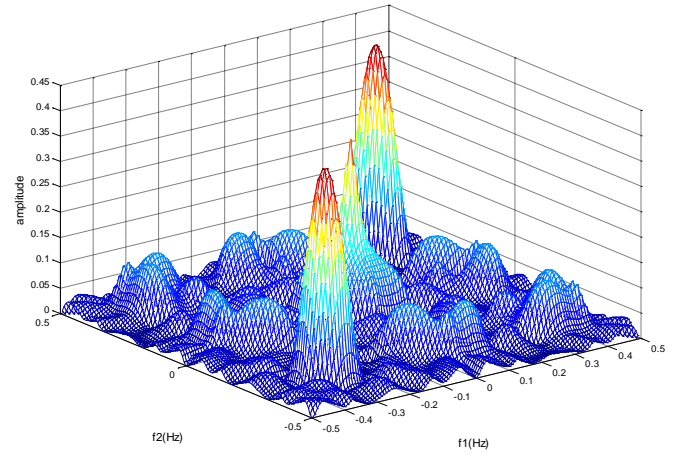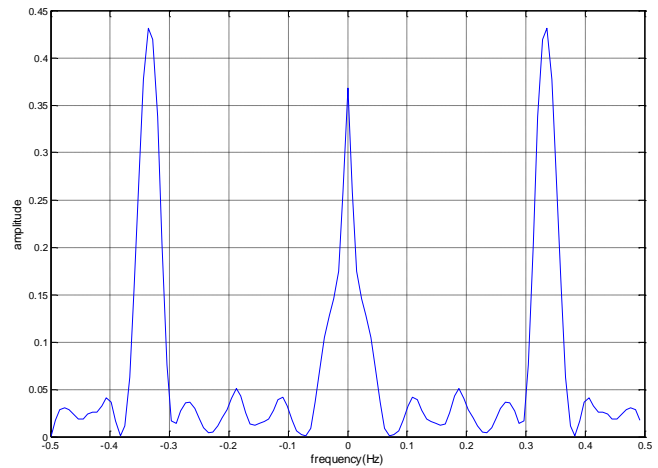Fig.2. Durable plate a) bicoherence b) diagonal slice graphics

Fig.3. Damaged plate 1 a) bicoherence b) diagonal slice graphics

The only one salient peak was observed in durable ceramic material and maximum bicoherence peak is in the magnitude size of bic(0,0) = 2.4263. According to this, other fairly small peaks are scattered on the surface (Figure2a). This case is also clearly observed in diagonal slice (Fig.2b).

As can be seen in Figure 3, the unrelatedness is increased around -0.3 and +0.3 in the analysis conducted for the damaged ceramic plate. In other words, distinctive features can be seen to increase. This case appears to be different from the durable ceramic material.

The centrally-spreading bicoherence peak and two bicoherence peaks bigger in size can be observed in this damaged ceramic material. Maximum bicoherence size is in the coordinates of bic(-0.33594,-0.33594) = 0.43121(Fig.3a,b).

a)

b)

Fig.4. Damaged plate 1 a) bicoherence b) diagonal slice graphics
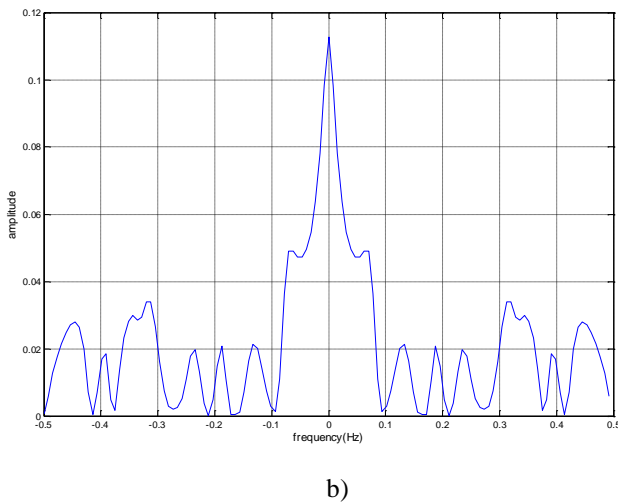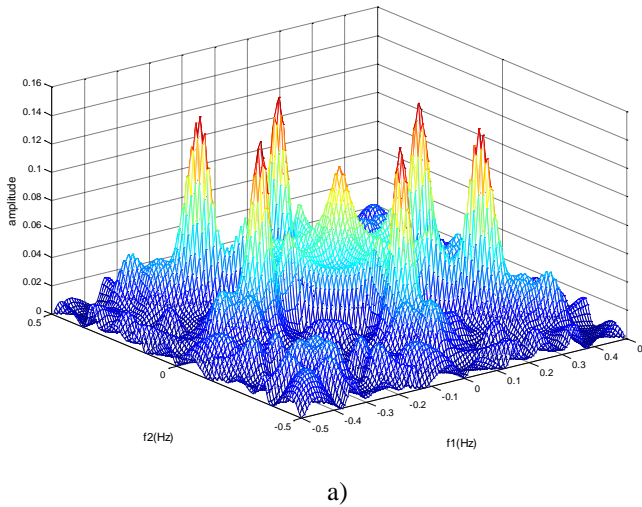

a)

b)

Fig.5. Damaged plate 1 a) bicoherence b) diagonal slice graphics

Bicoherence peak, which spreads in the state of two different peaks, and 6 larger bicoherence peaks around can be observed at the centre for other damaged ceramic material and maximum bicoherence value is in the size of bic(0,-0.24219) = 0.14369 (Figure4a). There are a maximum and two adjacent peaks at the centre in diagonal slice and there are also peaks in high frequencies and in smaller magnitudes (Fig.4b).
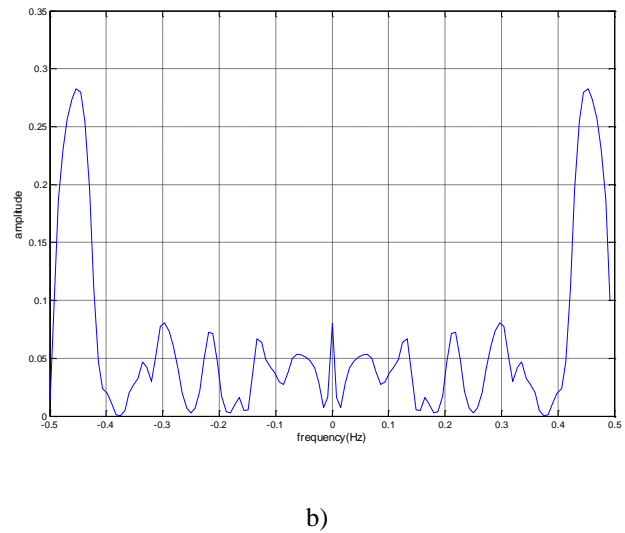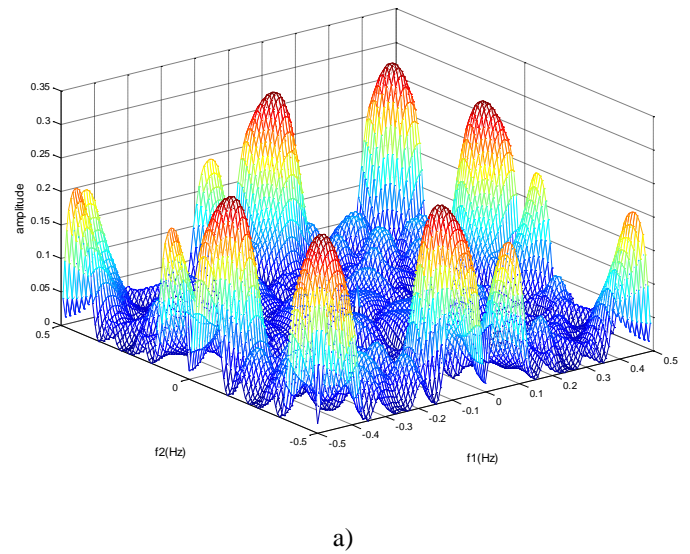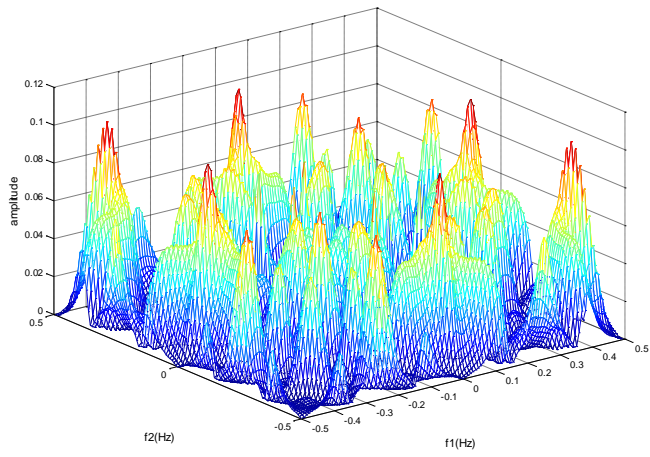
This example emphasizes bicoherence peaks observed at high frequencies and still, two peaks in the diagonal slice draw attention at high frequencies (Fig.5a, b). Maximum bicoherence is bic(-0.45313,-0.45313) = 0.2827.

a)
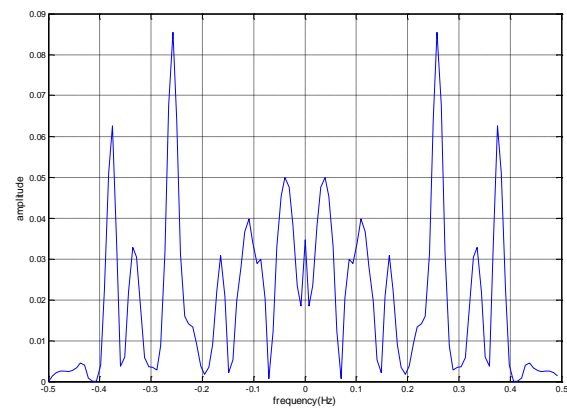
b)

Fig.6. Damaged plate 1 a) bicoherence b) diagonal slice graphics

a)

b)

Fig.7. Damaged plate 1 a) bicoherence b) diagonal slice graphics

This damaged ceramic material contains numerous bicoherence peaks (Fig.6a). The same case can also be observed in diagonal slice including 4 large peaks and other smaller peaks (Figure 6b). Maximum bicoherence is bic(0,-0.40625) = 0.10309.
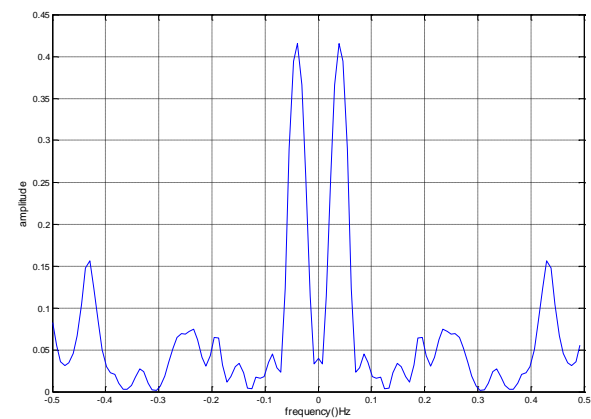
The final damaged plate example consists of 4 bicoherence peaks (Figure 7a). Two large diagonal peaks can be seen in the diagonal slice (Fig.7b). Maximum bicoherence was calculated as bic(0.039063,-0.078125) = 0.41517.

TABLE I
MAXIMUM BICOHERENCE COORDINATES AND
MAGNITUDES OF PLATES

Ceramic Material	Max. Bic.Coordinates	Max. Bic. Magnitudes
Durable	(0,0)	2,4263
Damaged 1	(-0.33594, -0.33594)	0,43121
Damaged 2	(0,-0.24219)	0,14369
Damaged 3	(-0.45313, -0.45313)	0,2827
Damaged 4	(0,-0,40625)	0,10309
Damaged 5	(0,039063, -0,078125)	0,41517

V. CONCLUSION

In this experimental study, the durability and crackness of ceramic plates were determined by using the bi-coherence analysis method. 6 same types of ceramic plates were used in the study. Of the plates used in the study, one of the plates was selected from durable plates for controlling purposes and the other 5 damaged plates were selected from the cracked plates. This study is the product of a project study which determines damages in ceramic plates by using an acoustic method. In the analysis, the impact was applied at the centre points of ceramic plates by using a pendulum and the sound occurred as a result of the impact, was analyzed by the data collection system. When analyzing the sound data obtained from the experimental data collection system, one bicoherence peak, with rising large magnitude, was observed at the centre on the bicoherence plane of the durable plate. More than one bicoherence peaks were formed in cracked ceramic plates and their magnitudes were quite smaller compared to those of durable plates (Table 1). While maximum bicoherence coordinates were formed at the coordinate centre in the durable material, deviation from the centre can be observed in damaged material (Table 1). These features can also be observed in two-dimensional diagonal slices in a simple way. The study can be considered quite determinative for distinguishing the state of durability and crackness of the ceramic plates.

REFERENCES

[1]   T.C. Akinci, "The Defect Detection in Ceramic Materials Based on Time-Frequency Analysis by Using the Method of Impulse Noise" Archives of Acoustics, Vol.36, No.1, 2011, pp.1–9.

[2]   T.C. Akinci, H.S. Nogay, O. Yilmaz, "Application of Artificial Neural Networks for Defect Detection in Ceramic Materials Archieves of Acoustics", Vol. 37, No.3, 2012, pp.279-286.

[3]   T.C. Akinci, S. Seker, R. Gurbuz, E. Guseinoviene, E., "Spectral and Statistical Analysis for Ceramic Plate Specimens Subjected to Impact", Solid State Phenomena .199, 2013, pp.621-626.

[4]   O. Akgun, T.C. Akinci, H.S. Nogay, S. Seker, "The defect detection in ceramic materials based on wavelet analysis by using the method of impulse noise", JVE Journal of Vibroengineering, Vol.15, No.2, 2013, pp.818-825.

[5]   L. Montanaro, N. Bianchini, J.Ma Rincon, M. Romero, "Sintering Behaviour of Pressed Red Mud Wastes from Zinc Hydrometallurgy", Ceram. Int., 27, 2001, pp. 29-37.

[6]   M. Romero, J. Ma Rincón, S. Musik, V. Kozhukharov, "Mössbauer Effect and X-ray Distribution Function Analysis in Complex Na2O-CaO-ZnO-PbO-Fe2O3-Al2O3-SiO2 Glasses and Glass-Ceramics" Mater. Res. Bull., 34, 1998, pp. 1107-1115.

[7]   A. Karamanov, M. Pelino, G. Taglieri, C. Cantalani, "Sintered Building Glass-Ceramics Based on Jarosite", XVIII International Congress on Glass, San Francisco (USA), July 5-10, 1998, The American Ceramic Society, Ohio, M. K. Choudhary, N. T. Huff and Ch. H. Drummond III (Eds.).

[8]   C. Barry Carter, M. Grant Norton, "Ceramic Materials", Springer Science+Business Media, LLC., 2007, pp.4-10.

[9]   R. Brian, "Lawn Indentation of Ceramics with Spheres: A Century after Hertz", J. Am. Ceram. Soc., Vol. 81, No.8, 1998, pp. 1977–94 .

[10]   R.O. Ritchie, "Mechanisms of fatigue-crack propagation in ductile and brittle solids", International Journal of Fracture, 100, 1999, pp. 55–83.

[11]   P.D. Zavattieri, H.D. Espinosa, "Grain Level Analysis Of Crack Initiation And Propagation In Brittle Materials", Acta mater., 49, 2001, pp. 4291–4311.

[12]   M. Suzuki, K. Ogawa, T. Shoji, "Quantitative NDE of Surface Cracks in Ceramic Materials by means of a High-Frequency Electromagnetic Wave", Materials Transactions, Vol.47, No.6, 2006, pp. 1605-1610.

[13]   J.J. Kruzic, O.R. Robert, "Determining the Toughness of Ceramics from Vickers Indentations Using the Crack-Opening Displacements: An Experimental Study", J. Am. Ceram. Soc., Vol.86, No.8, 2003, pp. 1433–36.

[14]   M.A. Aswad, "Comparison of the Fracture Toughness of High Temperature Ceramic measured by Digital Image Correlation and Indentation Method", Journal of Babylon University/Engineering Sciences, Vol. 22,No.4, 2014.

[15]   F. Mignard, C. Olagnon, G. Fantozzi, "Acoustic emission monitoring of damage evaluation in ceramics submitted to thermal shock" Journal of the European Ceramic Society, Vol.15, No.7, 1995, pp. 651–653.

[16]   K. Ito, S. Ohmata, S., K. Kobayashi, M. Watanabe, S. Kuroda, M. Enoki, "Crack Monitoring during Plasma Spraying of Ceramic Coatings by Non-Contact Acoustic Emission Method", Materials Transactions, Vol.51, No.7, 2010, pp. 1272- 1276.

[17]   W.P. Ganley, "Simple pendulum approximation", Am. J. Phys. Vol.53, No.1, 1985, pp.73–76.

[18]   T.C. Akinci, O. Yilmaz, T. Kaynas, M. Ozgiray, S. Seker, "Defect Detection for Ceramic Materials bey Continuous Wavelet Analysis Mechanika", Prooceedings of the 16th International Conference, 7-8 April 2011, Kaunas Lithuania, pp.9-14.

[19]   R. Başar, Ü. Artan, A. Akan, "Higher-Order Evolutionary Spectral Analysis", IEEE ICASSP 6, 2003, pp. 633-636.

[20]   B. Ergen, Y. Tatar, "The Bispectral Analysis of Phonocardiogram Signals", Biomedical Engineering National Meeting Biyomut Istanbul, Turkey , 2004, pp. 11-14.

[21]   J.M. Nichols, C.C. Olson, J.V. Michalowicz, F. Bucholtz, "The Bispectrum and Bicoherence for Quadratically Nonlinear Systems Subject to Non-Gaussian Inputs", Signal Processing, IEEE Transactions on, Vol. 57, No.10, 2009, pp. 3879-3890.

[22]   C.L. Nikias, "Higher-OrderSpectra Analysis", Prentice-Hall, Englewood Cliffs, 1993

[23]   B. Jang, C. Shin, E.J. Powers, W.M. Grady, "Machine fault detection using bicoherence spectra", Instrumentation and Measurement Technology Conference, IMTC 04. Proceedings of the 21st IEEE 3 2004, pp. 1661-1666

[24]   K. Han, K.R. Tinsley, J. Aguilar-Torrentera, "Identification of high speed jittered digital interconnects using bicoherence spectra", Devices, Circuits and Systems,. ICCDCS 2008. 7th International Caribbean Conference on, 2008, pp. 1- 4.

BIOGRAPHIES

OMER AKGUN is an assistant professor at the, Department of Computer Engineering, Technology Faculty, Marmara University. He received his first Ph.D. in the Communication Engineering in 2009 from Yildiz Technical University and the second Ph.D. in the Electronic and Communication Education Department in 2011 from Marmara University. His current research interests are signal processing, biomedical signal processing, signal modelling and communication systems.

Microwave Spectroscopy Based Classification of Rat Hepatic Tissues: On the Significance of Dataset

T. YILMAZ

Abstract—**With the advancements in machine learning (ML) algorithms, microwave dielectric spectroscopy emerged as a potential new technology for biological tissue and material categorization. Recent studies reported the successful utilization of dielectric properties and Cole-Cole parameters. However, the role of the dataset was not investigated. Particularly, both dielectric properties and Cole-Cole parameters are derived from the S parameter response. This work investigates the possibility of using S parameters as a dataset to categorize the rat hepatic tissues into cirrhosis, malignant, and healthy categories. Using S parameters can potentially remove the need to derive the dielectric properties and enable the utilization of microwave structures such as narrow or wideband antennas or resonators. To this end, *in vivo* dielectric properties and S parameters collected from hepatic tissues were classified using logistic regression (LR) and adaptive boosting (AdaBoost) algorithms. Cole-Cole parameters and a reproduced dielectric property data set were also investigated. Data preprocessing is performed by using standardization a principal component analysis (PCA). Using the AdaBoost algorithm over 93% and 88% accuracy is obtained for dielectric properties and S parameters, respectively. These results indicate that the classification can be performed with a 5% accuracy decrease indicating that S parameters can be an alternative dataset for tissue classification.**

Index Terms—**Cole-Cole parameters, dielectric properties, *in vivo* measurements, machine learning, rat hepatic tissues.**

I. INTRODUCTION

DIELECTRIC PROPERTY discrepancy between healthy and diseased biological tissues enabled many different applications of electromagnetics in medicine including but not limited to microwave hyperthermia, microwave breast cancer imaging, and microwave blood glucose detection [1-3]. Microwave dielectric properties can be characterized using different methods. The characterization method is determined based on different features including the frequency of operation, nature of sample, and temperature range. One such technique that has been used for broadband dielectric property

TUBA YILMAZ, is with Department of Electronics and Communication Engineering, Istanbul Technical University, Istanbul, Turkey, (e-mail: tuba.yilmaz@itu.edu.tr).

https://orcid.org/0000-0003-3052-2945

measurements of high permittivity and high loss materials is the open-ended coaxial probe technique. Open-ended coaxial probes are commercially available for laboratory use; therefore, the technique has been widely utilized for dielectric property characterization of different materials including liquids, gel-like materials, along with biological tissues [4]. Being a broadband method, it is known that the technique suffers from large error rates. The source of error can be user, sample, technique based or a combination of those.

It is recommended that during the laboratory use, the user should follow a calibration scheme before measurement and the calibration should be repeated after completion of a number of measurements, measurement set-up should be fixed and sample should be brought to the tip of the probe and tight contact between the probe and the measurement sample should be ensured. Even when the listed conditions are met during a measurement, the commercial probes reports ±5% error [5].

In the reported literature, despite the reported high measurement error, different potential applications of the technique have been proposed. An example of a practical application is the utilization of the probe for kidney stone classification [6]. Another practical realization is using the probe for biopsy or surgical margin determination or a biopsy probe [7,8]. In a practical setting, the error rate is expected to increase up to 30% [4]. To mitigate the error, several approaches can be applied including hardware and mathematical updates. However, previously reported studies proved that, without costly updates on the method, the accuracy of tissue classification can be increased by adopting machine learning (ML) based classification algorithms [6-8]. Such algorithms are not necessarily concerned with determining the dielectric properties of the samples; however, they determine the type of the sample under test. Based on the reported classification results in previous studies, the accuracy can be improved approximately 10% to 30% with this approach.

The reported accuracy advancements were obtained by application of classification algorithms to two types of datasets the first and mostly used one is the dielectric property data and the second one is the parameters of mathematical models [6-8]. The mathematical models are widely used to represent the dispersive dielectric property behavior with respect to frequency. The goal is to use fewer parameters that can later be generalized to obtain dielectric properties at the desired frequencies. Mathematical models have been widely

used in the literature to report the measured dielectric properties of biological tissues as well as several different liquids [9]. One of the commonly used mathematical model is the single pole Cole-Cole equation.

Both dielectric properties and Cole-Cole parameters are calculated parameters. The dielectric properties are calculated from the S parameters which are directly measurable quantities. The Cole-Cole parameters are fitted to calculated dielectric properties. Although the performance of classification algorithms was evaluated for both dielectric properties and Cole-Cole parameters in the literature, classification with S parameters have not been explored. This work presents a comparison of the multi-class classification results based on four datasets, namely dielectric properties, Cole-Cole parameters, S parameters, and reproduced dielectric properties from Cole-Cole parameters. All data sets are obtained from same rat hepatic tissue samples and in some cases, they are reproduced from one another. Classification with these datasets investigated to explore the role of the data type on classification accuracy. More significantly this work investigates S parameter-based classification that can potentially eliminate the need for dielectric property retrieval and Cole-Cole parameter calculation.

The remainder of this paper is organized as follows: In section II the measurement set-up, *in vivo* data collection, data curation and the ML algorithms are detailed, the raw data for each group, data obtained through modelling and classification results for each data type are given in section III, conclusions are drawn in section IV.

II. METHODOLOGY

A detailed description of the dielectric property measurement, as well as the description of samples, were given in [7-10]. Therefore, we briefly explain the sample preparation and dielectric property measurements in this section.

A. Measurement Set-up and Calibration

The measurement set-up included an open-ended coaxial probe connected to a Fieldfox N9923A Network Analyzer (NA) with an RF cable. Type of the probe was a slim-form with 2.2 mm aperture diameter. Agilent 85070 software was utilized for dielectric property data collection. The calibration was performed by following standard open-short-deionized water calibration procedure. Deionized water temperature was measured before the calibration and entered to the software. The probe tip was air dried after completion of the calibration.

B. *In vivo Data Collection*

Female Wistar Albino rats were obtained from the Istanbul University, Institute of Experimental Medicine at 120 days old. The number of experiment animals were 30. The animals were divided into two groups namely control and experiment. The experiment group received 50 (mg/kg) Diethylnitrosamine (Sigma Chemical Company, St. Louis, MO, USA)- solution once a week via intraperitoneal injection. The control group received an intraperitoneal injection of 0.1M saline solution. After 10 weeks the animals were left to rest for 6 weeks.

Throughout the experiments the animals were kept in 12-hour light/dark cycle and had ad libitum access to tap water and standard pellet food. During the chemical induction period of 10 weeks, 8 animals died from the experiment group. After the rest period is completed measurements were taken and the animals were immediately sacrificed upon completion of the measurements. Before measurements the animals were anesthetized via intraperitoneal injection of 80 (mg/kg) ketamine + 10 (mg/kg) xylazine mixture. The experiments were in accordance with the Istanbul University, Animal Experiments Local Research Ethics Committee. To collect the measurements, anesthetized animal's liver is accessed via intraperitoneal incision. Two sets of measurements were taken; that is, wet and dry. The wet measurements were taken immediately after incision. Dry measurements were taken after the wet measurement area is wiped with a 0.1M saline solution. This procedure is performed to clean the area from accumulated blood. The procedure is also widely practiced during surgeries. The number of collected measurements varied based on the sample availability.

C. Cole-Cole Fitting

Cole-Cole equation is widely used in the literature to represent the dispersive dielectric property behavior of many different materials including but not limited to biological tissues, biological fluids, and polar liquids such as alcohols. The variables in Cole-Cole equation are $\Delta\varepsilon$ dielectric constant difference between lower and higher frequencies ($\Delta\varepsilon=\varepsilon_s-\varepsilon_\infty$), τ is the relaxation time, α relaxation constant, and σ_i ionic conductivity. These variables are named Cole-Cole parameters. Cole-Cole parameters are fitted to the measured dielectric properties with various curve fitting techniques. In this work, the parameters were fitted with Particle Swarm Optimization (PSO) algorithm, the details of the technique were described in [6,10]; therefore, it is briefly given in this article. The Cole-Cole equation is given below,

$$\varepsilon' - i\varepsilon'' = \varepsilon_\infty + \frac{\Delta\varepsilon}{1+(i\omega\tau)^{(1-\alpha)}} + \frac{\sigma_i}{i\omega\varepsilon_0} \tag{1}$$

where ε' is dielectric constant, ε'' is dielectric loss factor, ω is angular frequency ($\omega=2\pi f$). The PSO algorithm searches a pre-determined solution space to reach an optimal solution. The pre-determined solution domain is constructed by defining intervals to the listed five Cole-Cole parameters. The intervals are given in Table I. PSO is a stochastic optimization technique developed based on the swarm behavior. In a swarm each member's next location is determined through a combination of the experience of the individual and the swarm. These individuals are named particles and in this work their locations, namely the Cole-Cole parameters, are kept as a vector. 20 particles were used in this work, the particles evaluate their locations on each iteration and determine the next location based on the best value obtained by all particles and the best value obtained by each particle. The goodness of a location is determined by reproducing dielectric properties

between 0.5 to 6 GHz with 0.5 GHz resolution and finding the Euclidean distance between the reproduced and measured dielectric properties. The Euclidean distance is given with equation (2),

$$error = \frac{1}{N}\sum_{i=1}^{N}\left[\left(\frac{\varepsilon'_{\omega_i} - \hat{\varepsilon}'_{\omega_i}}{median(\varepsilon'_{\omega i})}\right)^2 - \left(\frac{\varepsilon''_{\omega_i} - \hat{\varepsilon}''_{\omega_i}}{median(\varepsilon''_{\omega i})}\right)^2\right] \qquad (2)$$

N is the number of frequency points used during the measurements (N=12). ε'_{ω_i} and ε''_{ω_i} represents the measured dielectric constant and loss factor, respectively. $\hat{\varepsilon}'_{\omega_i}$ and $\hat{\varepsilon}''_{\omega_i}$ represents the calculated dielectric constant and loss factor, respectively. Maximum iteration number is set to 50. If a solution reached a Euclidean distance smaller than the threshold of 0.001 otherwise the algorithm keeps trying to find the best location until the iteration limit is reached.

TABLE I
COLE-COLE PARAMETER SOLUTION INTERVALS

Cole-Cole Parameters	ε_∞	$\Delta\varepsilon$	τ (ps)	α	σ_i (S/m)
Min	1	1	1	0.01	0.01
Max	80	80	20	1	3

After fitting the Cole-Cole parameters a new dataset was reproduced from the fitted Cole- Cole values. This step was taken in order to reduce dielectric property discrepancy between the frequency points. Though smoothing the dielectric properties with respect to frequency, the measurement errors can be potentially mitigated. The Cole-Cole fitting results as well as the reproduced data is given in Section III.

D. Data Pre-processing

Four sets of data obtained from dielectric properties, S parameter measurements, Cole-Cole parameters and reproduced dielectric properties were used in three different forms to train and test the ML algorithms. The raw data is used without pre-processing.

The second set was the standardized datasets. Standardization is known to re-distribute the data to resemble a Gaussian distribution. Some algorithms are known to perform well on standardized data such as linear learners. In fact, standardization is a requirement for many ML algorithms. The standardization is performed on each feature by subtracting the mean (u) from each data point (x) and dividing it by the standard deviation (s) (z=(x-u)/s).

Third kind of data sets were obtained by applying principal component analysis (PCA) to the standardized data. PCA is used for dimensionality reduction purposes and to transform the data in order to maximize the discrepancy between the classes [11]. In this work, we used the PCA to exploit the difference between the classes since the dimensionality reduction was not a concern. PCA works by calculating new set of features, called eigenvalues, computed from the

covariance matrix. This matrix describes the correlations between features. Eigenvalues does not represent a physically meaningful quantity; however, geometrically it represents the independent dimensions with maximum variances. Both the PCA and standardization were applied separately to the train and test groups to avoid peeking.

E. Machine Learning Algorithms

Performances of two ML algorithms namely logistic regression (LR) and adaptive boosting (AdaBoost) were investigated. These algorithms were selected based on the previously reported research since the dielectric properties were successfully classified using the linear and ensemble methods. Both LR and AdaBoost algorithm designed for binary classification problems. One-vs-Rest (OvR) scheme is used to adopt the algorithms for multiclass classification. OvR is the most commonly used scheme for multiclass classification. It works by separating the original data to number of classes and applies the classifier to each set. One drawback is the computational cost specifically if the number of classes are large.

LR, a linear algorithm, performs the classification based on the calculated probabilities [12]. LR uses sigmoid function to estimate the probability of a sample belonging to one of two classes. Sigmoid function is given in equation (3).

$$p = \frac{1}{1 + e^x} \qquad (3)$$

Sigmoid function is an S shaped curve limited between 0 and 1. Using maximum likelihood (ML) during training the LR algorithm adjusts the curve to obtain the optimum fitting. This work uses the L2 regularized cost function to solve the classification problem. One advantage of the LR algorithm is the ability to decrease the weights of the irrelevant features. That is, the algorithms tune itself to increase the weight of significant features. In earlier studies it was proven that the linear methods tend to perform well on dielectric property data classification.

AdaBoost algorithm is an ensemble method and uses weak classifiers to obtain a strong classifier [13]. This work used decision tree classifiers as weak classifiers. Typically, AdaBoost stars by training a weak classifier with the given training set by giving a weight of 1 to each data on the training set. Next, AdaBoost increases the weight of the misclassified training data and trains another classifier with the weighted training set. This process iteratively continues until the maximum iteration number is reached; the iteration number is set to 100 for this work. The trained classifiers receive a score and base on the score weighted combination of the classifiers is linearly combined to form a strong classifier.

Pre-processing and classification of the data are performed in Python language using scikit-learn libraries [14].

III. RESULTS AND DISCUSSION

A. Dielectric properties

Total measurements collected from healthy, malignant and cirrhosis tissues are 395, 285, and 95, respectively. To form balanced classes the number of data points are deduced to 95

for healthy and malignant tissue classes. This is performed by randomly selecting data points from the two data points.
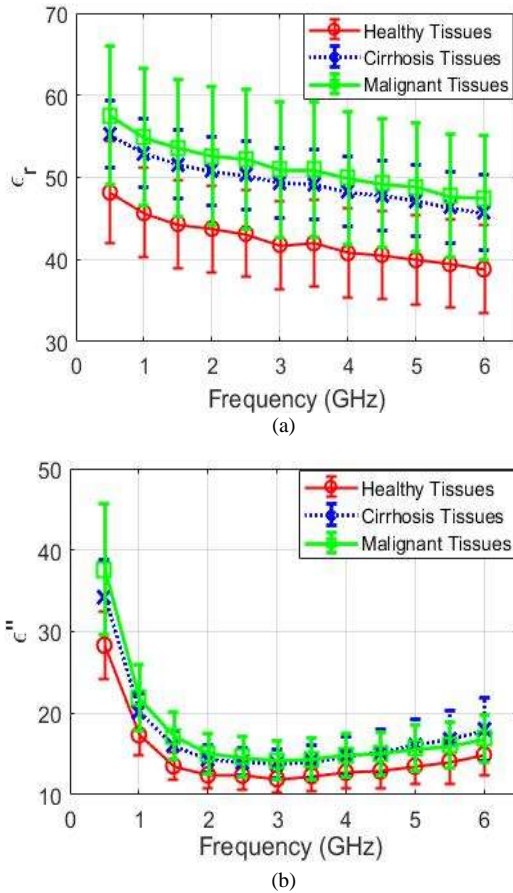

(a)

(b)

Fig.1. Mean and standard deviation of *in vivo* dielectric properties of healthy, cirrhotic, and malignant rat hepatic tissues; (a) Relative dielectric constant comparison, (b) Dielectric loss comparison.

The measurements are performed between 0.5 GHz to 6 GHz with 0.5 GHz resolution. It should be noted that in this work the whole data set is used and the measurements are not categorized as dry and wet. Mean as well as the standard deviation of dielectric constant and dielectric loss is given in Figure 1(a) and Figure 1(b), respectively, for each of the balanced tissue classes. Mean dielectric constant and loss discrepancy between healthy and malignant, healthy and cirrhosis, cirrhosis and malignant tissues are less than 21.2% and 19.9%, 17% and 17.3%, 3.6% and 4.6% for the whole frequency band, respectively.

B. S-parameter Measurements

The S parameters associated with the dielectric properties were also recorded during measurements. As noted, before, dielectric properties are essentially derived from the S parameter measurements. Figure 2(a) and Figure 2(b) shows the measured real and imaginary parts of S_{11} parameters corresponding to dielectric properties given with Figure 1.

Percent difference for mean real and imaginary parts of S_{11} response between healthy and malignant, healthy and cirrhosis, cirrhosis and malignant tissues are less than 20.5% and 11.1%, 18% and 9.1%, 3.4% and 1.8% for the whole
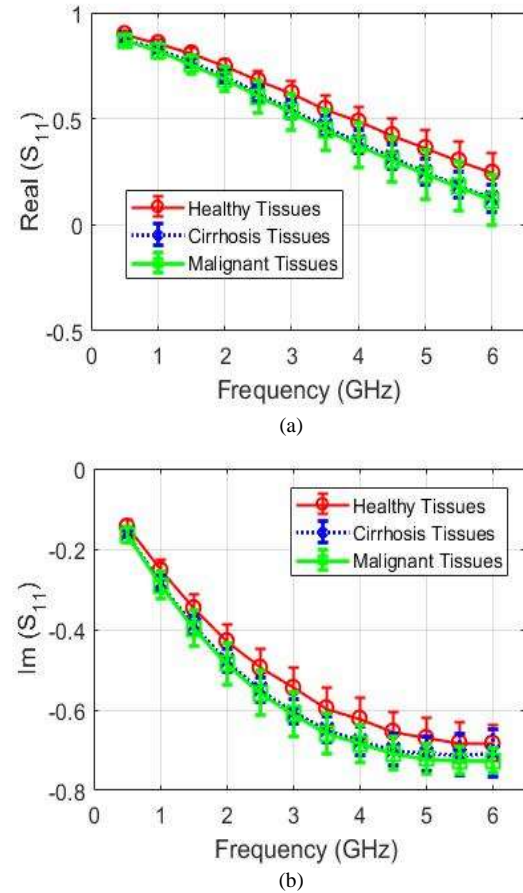
frequency band, respectively. The percent discrepancies are slightly lower than dielectric property discrepancies.

(a)

(b)

Fig.2. Mean and standard deviation of *in vivo* measured S_{11} response of the probe when the open end is terminated with healthy, cirrhotic, and malignant rat hepatic tissues; (a) Real part of S_{11} response comparison, (b) Imaginary part of S_{11} response comparison.

C. Cole-Cole parameters

Cole-Cole parameters were fitted to each 95 measurements collected from healthy, cirrhosis, and malignant rat tissue samples.   Comparisons of sample measurements collected from healthy rat hepatic tissues with the fitted Cole-Cole parameters are shown in Figure 3.
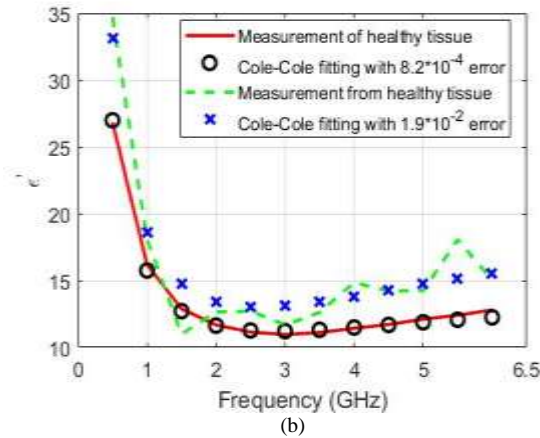

(a)

(b)
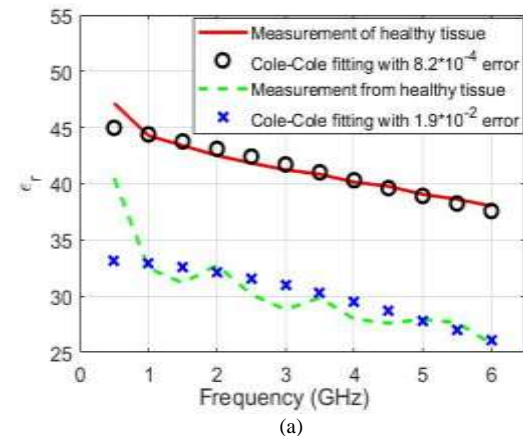
Fig.3. Comparison of measured dielectric properties collected from healthy rat hepatic tissues and the Cole-Cole fittings with minimum and maximum error; (a) Two dielectric constants and the corresponding Cole-Cole fittings, (b) Two dielectric loss and the corresponding Cole-Cole fittings

TABLE II
SAMPLES OF THE FITTED COLE-COLE PARAMETERS TO THE MEASURED DIELECTRIC PROPERTIES OF EACH GROUP WITH MAXIMUM AND MINIMUM ERROR RATES

Cole-Cole Parameters	ε_∞	$\Delta\varepsilon$	τ (ps)	α	σ_i (S/m)	error
Healthy	15.37	30.15	12.51	0.15	0.7	8.2e-04
	1.63	31.56	14.05	0.01	0.88	1.9e-02
Cirrhosis	14.7	51.01	10.16	0.04	1.31	4.8e-04
	7.72	42.07	14.67	0.01	0.77	4.3e-03
Malignant	12.15	57.29	7.67	0.09	1.5	5.5e-04
	25.4	41.74	13.89	0.32	1.09	8.1e-03

Figure 3 (a) and Figure 3 (b) gives the dielectric constant and loss values, respectively, obtained from measurements and Cole-Cole fittings with maximum and minimum errors. As it can be seen from Figure 3, Cole-Cole fitting errors depends on the quality of the measurement.
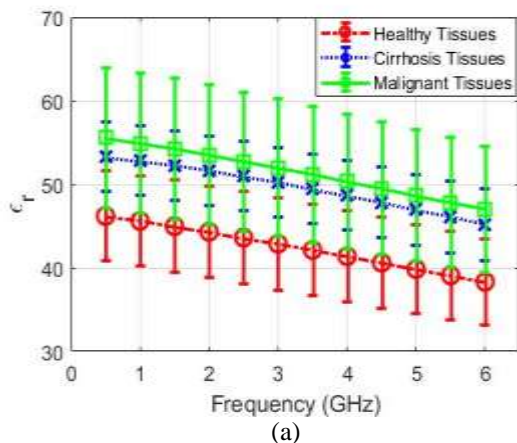

(a)

(b)

Fig.4. Mean and standard deviation of dielectric properties of healthy, cirrhotic, and malignant rat hepatic tissues obtained from the Cole-Cole fittings; (a) Relative dielectric constant comparison, (b) Dielectric loss comparison.

Fitted Cole-Cole parameters with maximum and minimum error for each tissue class is given in Table II. Fitted Cole-Cole parameters were used to produce dielectric property dataset. The goal was to reproduce the dielectric properties to minimize the measurement error. Mean and standard deviation of the reproduced dielectric property dataset for relative dielectric constant and dielectric loss are given in Figure 4(a) and Figure 4(b), respectively. Mean dielectric constant and loss discrepancy between healthy and malignant, healthy and cirrhosis, cirrhosis and malignant tissues are less than 21.3% and 19.9%, 17.0% and 17.5%, 3.7% and 4.3% for the whole frequency band, respectively.

D. Classification Performances

Leave-one-out (LOO) cross validation (CV) scheme was used for classification due to the limited number of the data (95 data from each class). Over 80% accuracy was obtained using LR algorithm along with raw dielectric properties. LR did not perform as well on raw S_{11} data set. LR seems to be sensitive to standardization since the accuracy loss reached up to10 % for raw dielectric property data and it improved over 10% for S_{11} data when applied after the standardization. AdaBoost on the other hand is not sensitive to the standardization of the data the accuracies did not significantly changed after standardization. Both Cole-Cole parameters and the reproduced dielectric properties from Cole-Cole parameter datasets did not perform well with both algorithms. This indicates that despite the low error fittings part of the data is corrupted during the process. It should also be noted that the classification with Cole-Cole parameters can be achieved with high accuracy when the dielectric property data are collected under ideal conditions with low standard deviation [6].

AdaBoost performs with over 93% accuracy after the PCS is applied to the standardized dielectric property data. Similarly, AdaBoost is able to active 88% accuracy after the application of PCA to standardized S_{11} data. Having said that, hyperparameter optimization was not performed in this work We can state that further potential improvement of the accuracy results is possible with hyperparameter optimization.
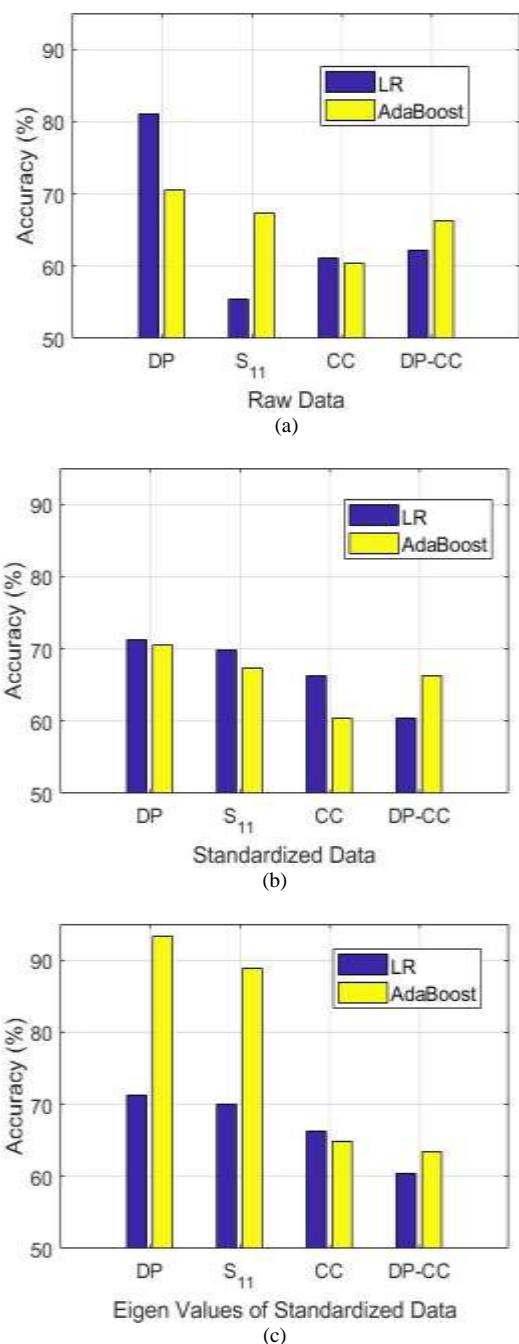
Figure 5. Accuracy results obtained from application of Logistic Regression (LR) and Adaptive Boosting (AdaBoost) algorithms to dielectric properties (DP), measured S11 parameters, Cole-Cole (CC) parameters fitted to the DP, and DP reproduced by using the fitted CC (DP-CC): (a) Accuracy results obtained from the raw data, (b) Accuracy results obtained from the standardized data ,(c) Accuracy results obtained through the application of Principal Component Analysis to the standardized data.

IV. CONCLUSIONS

This work investigated the significance of dataset for microwave measurement-based classification of the rat hepatic malignancies. In the literature, different microwave spectroscopy datasets were utilized to classify different biological tissue types and materials. Dielectric properties, S parameters, fitted Cole-Cole parameters, and dielectric

properties reproduced from the Cole-Cole parameters were investigated to understand the classification accuracy performances. Two common classifiers LR and AdaBoost were used. Note that the classification based on S_{11} parameters have not bee investigated in the literature. It was concluded that the classification accuracies can be increased by employing PCA and ensemble methods tend to reach over 88% accuracies for S_{11} and dielectric property datasets. By using S_{11} the accuracy decreases by 5% indicating that S_{11} parameter-based classification can produce reliable results.

REFERENCES

[1]   T. U. Gürbüz, B. Aslanyürek, A. Yapar, H. Şahintürk I. Akduman. "A Nonlinear Microwave Breast Cancer Imaging Approach Through Realistic Body–Breast Modeling." IEEE Transactions on Antennas and Propagation, vol. 62. 5, 2014, pp. 2596-2605.

[2]   M. Converse, E. J. Bond, S. C. Hagness, B. D. Van Veen. "Ultrawide-band microwave space-time beamforming for hyperthermia treatment of breast cancer: a computational feasibility study." IEEE Transactions on Microwave Theory and Techniques, vol. 52. 8, 2004, pp. 1876-1889.

[3]   T. Yilmaz, R. Foster, Y. Hao. "Radio-Frequency and Microwave Techniques for Non-Invasive Measurement of Blood Glucose Levels. " Diagnostics, vol 9.1, 2019, pp. 1-34.

[4]   D. Popovic, L. McCartney, C. Beasley, M. Lazebnik, M. Okoniewski, S. C. Hagness, J. H. Booske."Precision open-ended coaxial probes for in vivo and ex vivo dielectric spectroscopy of biological tissues at microwave frequencies." IEEE Transactions on Microwave Theory and Techniques, vol. 53.5, 2005, pp. 1713-1722.

[5]   Keysight Technologies. Probe Characteristics and Specifications, Keysight N1501A, Dielectric Probe Kit 10 MHz to 50 GHz. Available online:https://literature.cdn.keysight.com/litweb/pdf/5992-0264EN.pdf?id=2605692 (accessed on 25 July 2020).

[6]   B. Saçlı, C. Aydınalp, G. Cansız, S. Joof, T. Yilmaz, M. Çayören, B. Önal, I. Akduman. "Microwave dielectric property based classification of renal calculi: Application of a kNN algorithm." Computers in biology and medicine, vol. 112. 2019, pp. 103366.

[7]   T. Yilmaz. "Multiclass Classification of Hepatic Anomalies with Dielectric Properties: From Phantom Materials to Rat Hepatic Tissues. " Sensors, vol. 20, 2020, pp. 530.

[8]   T. Yilmaz, M. A. Kılıç, M. Erdoğan, M. Çayören, D. Tunaoğlu, İ. Kurtoğlu, Y. Yaslan et al. "Machine learning aided diagnosis of hepatic malignancies through in vivo dielectric measurements with microwaves." Physics in medicine & biology, vol 61.13, 2016, pp. 5089.

[9]   S. Gabriel, R. W. Lau, C. Gabriel. "The dielectric properties of biological tissues: III. Parametric models for the dielectric spectrum of tissues." Physics in medicine & biology, vol. 41.11, 1996, pp. 2271.

[10]   T. Yilmaz, F. Ates Alkan. "In Vivo Dielectric Properties of Healthy and Benign Rat Mammary Tissues from 500 MHz to 18 GHz." Sensor, vol. 20, pp. 2214.

[11]   T. Jolliffe, J. Cadima. "Principal component analysis: a review and recent developments." Philosophical Transactions of the Royal Society A: Mathematical, Physical and Engineering Sciences, vol. 374, pp. 2065, 2016.

[12]   L. Shen, E.C. Tan. "Dimension reduction-based penalized logistic regression for cancer classification using microarray data." IEEE/ACM Transactions on computational biology and bioinformatics, vol. 2.2, 2005, pp. 166-175.

[13]   T. Hastie, R. Saharon, J. Zhu, H. Zou. "Multi-class adaboost." Statistics and its Interface, vol 2.3, 2009, pp. 349-360.

[14]   Scikit-learn: Machine Learning in Python, Pedregosa et al., JMLR 12, 2011, pp. 2825-2830.

BIOGRAPHIES

TUBA YILMAZ received the B.S. degree from Istanbul Technical University, Istanbul, Turkey, M.S. degree in Electrical Engineering from Mississippi State University, Mississippi State, MS, USA, in 2009, and the Ph.D. degree in electronic engineering and computer science from Queen Mary, University of London, London, U.K., in 2013.

She is currently an Assistant Professor and a Marie Sklodowska Curie Research Fellow in Department of Electronics and Communication Engineering at Istanbul Technical University (ITU). Prior to her appointment at ITU, she spent a year at Mitos Medical Technologies as an Associate Research Fellow. From 2013 – 2014, Dr. Yilmaz was with Utah State University (USU) as a Postdoctoral Research Fellow. She is a member of Eta Kappa Nu Electrical and Computer Engineering Honor Society. She has received multiple awards including URSI Young Scientist Award and IBM Best Poster Award. Her research interests include wearable and implantable antennas, RF sensing, dielectric spectroscopy, evolutionary optimization techniques, application of supervised learning algorithms, wireless power transfer, and microwave imaging.

Comparing of Some Convolutional Neural Network (CNN) Architectures for Lane Detection

O. T. EKŞİ and G. GÖKMEN

Abstract— **Advanced driver assistance functions help us prevent the human-based accidents and reduce the damage and costs. One of the most important functions is the lane keeping assist which keeps the car safely in its lane by preventing careless lane changes. Therefore, many researches focused on the lane detection using an onboard camera on the car as a cost-effective sensor solution and used conventional computer vision techniques. Even though these techniques provided successful outputs regarding lane detection, they were time-consuming and required hand-crafted stuff in scenario-based parameter tuning.**

Deep learning-based techniques have been used in lane detection in the last decade. More successful results were obtained with fewer parameter tuning and hand-crafted things. The most popular deep learning method for lane detection is convolutional neural networks (CNN). In this study, some reputed CNN architectures were used as a basis for developing a deep neural network. This network outputs were the lane line coefficients to fit a second order polynomial. In the experiments, the developed network was investigated by comparing the performance of the CNN architectures. The results showed that the deeper architectures with bigger batch size are stronger than the shallow ones.

Index Terms— **Deep learning, convolutional neural network, lane detection**

I. INTRODUCTION

LANE DETECTION using computer vision techniques has been getting more attention for decades. Conventional computer vision techniques have addressed the lane detection system using three procedures as the following: 1) preprocessing, 2) feature extraction and model fitting, 3) lane tracking. These techniques generally are represented by two categories: feature-based, and model-based [1].

O. T. EKŞİ, Department of Mechatronics Engineering, Technology Faculty, University of Marmara, Istanbul, Turkey, (e-mail: osmantahireksi@gmail.com).

https://orcid.org/0000-0002-8994-0474

G. GÖKMEN, Department of Mechatronics Engineering, Technology Faculty, University of Marmara, Istanbul, Turkey, (e-mail: gokhang@marmara.edu.tr).

http://orcid.org/0000-0001-6054-5844

Feature-based techniques depend on feature extraction regarding the lane such as edges and colors of the lane lines [1]. Kreucher and Lakshmanan [2] developed an algorithm called LANA (Lane-finding in Another domAin) which represented the features in the frequency domain and combined them with a deformable template to detect the lane markers. Collado et al. [3] created a bird-view of the camera images showing the road to eliminate the perspective view. They also utilized spatial lane features and Hough transform on this view to detect the lane adaptively. Borkar et al. [4] proposed a layered approach for lane detection in the night vision. They used a temporal blurred technique on the video frames to reduce the noise, and a local adaptive thresholding technique to take the binary images on which Hough transform implemented to find the lane markers. Lane detection process may fail, since the on-road vehicles can occlude the lane partially or completely. Satzoda and Trivedi [5] came up with ELVIS (Efficient Lane and Vehicle detection with Integrated Synergies) algorithm to handle this problem by detecting the on-road vehicles along with the lane. Mammeri et al. [6] used Maximally Stable Extremal Region technique with Hough transform for lane detection, and Kalman filter to track the detected lane. Jung et al. [7] introduced a spatiotemporal lane detection algorithm to take the advantage of some specific row pixels of the past images. In lane detection step, Hough transform was preferred.

Model-based techniques try to represent the lanes with some geometric models such as a linear model, a parabolic model, or most of the time spline models [1]. In [8], Catmull-Rom spline-based model was proposed to detect the lane boundary. This model, which has control points, enabled the detection system to represent arbitrary road shapes in a wider range compared to the previous models. Lim et al. [9] utilized Hough transform for lane detection within the near-field of the image. Since this model could not estimate the curvatures successfully at the far-field, a river flow method was proposed. To track the lane in the consecutive frames, a B-spline based Kalman filter system presented. Another two-field study was conducted by Tan et al. [10], and for the near-field, Hough transform was implemented. A hyperbolic model and RANSAC algorithm were used for creating the curved lines in the far-field. The coefficients for these lines were found by an improved river flow method. In [11], a method was proposed called Lane Detection with Two-stage Feature Extraction (LDTFE) against the challenges in lane detection due to lighting conditions and background clutters in the images. A modified Hough transform was applied

to extract small line segments of the lane, and then these segments are divided into two different classes by Density Based Spatial Clustering of Applications with Noise (DBSCAN) algorithm in this method. Lastly, the lane identified by curve fitting.

Deep learning using convolutional neural network (CNN) for lane detection has been on the rise for the last decade as an alternative to the conventional computer vision techniques. Various CNN architectures have been developed, as the computer hardware improved.

In this paper, we proposed a CNN-based deep neural network model to detect the lane by representing the lines with second order polynomial's coefficients. We used some reputed CNN architectures in this model to compare their performance on lane detection. Fully connected neural network layers were built on the CNN part in a parallel way to find the coefficients.

This paper is organized as follows: In section two, a literature review about CNN-based lane detection works was presented. Section three describes CNN with its components and explain the designed architecture for the study. In section four, the experimental steps are explained using TuSimple dataset. Finally, the experimental results are compared and discussed at the conclusion section.

II. RELATED WORKS

Gurghian et al. [12] put a down-facing camera on each side of a car for lane detection. This detection was an end-to-end process depending on a CNN model without any preprocessing or postprocessing. The model was trained using the collected real data and synthesized data. In the test, the model could estimate the lane with sub-centimeter accuracy. He et al. [13] proposed a Dual-View Convolutional Neutral Network (DVCNN) for lane detection. The images taken from the front-view camera of the car was transformed to bird-view using IPM. Then those images were sent to a CNN-based model with the original ones. The inputs of the model proceeded in a parallel way inside, and at the end, they merged with each other as an output. Finally, by a global optimization technique where the lane line probabilities, lengths, widths, orientations and the amount are considered, true lane lines could be detected. In [14], VPGNet that could detect the lane under harsh weather and lighting conditions was introduced. This architecture enabled the authors to identify and classify the lane and road signs and estimate the vanishing point. Pizzati et al. [15] modeled an end-to-end CNN architecture which was in a cascaded form. They trained it by 14336 lane boundaries from TuSimple dataset. In this way, the lane boundaries in the images were detected, clustered, and classified.

III. METHOD

In this section, we described convolutional neural network (CNN). We also gave a deep neural network in which the most reputed CNN architectures were utilized for lane detection.

A. Convolutional Neural Network

Convolutional neural network (CNN) is a subset of deep neural networks and specialized to process grid-like topological data. For instance, taken at regular intervals time series data can be thought of as a 1D grid, on the other hand, image data consisting of pixels can be thought of as a 2D grid. The name of this network comes from a linear mathematical operation called convolution which is implemented on the input data through the convolutional layers of the network [16].

Basically, CNN models include an input layer, an output layer and hidden layers as in deep neural networks. The layers can be in different forms as well except for the convolutional one to fulfill the objective of the application or to improve the performance of the network. Pooling layer, dropout layer, batch normalization layer, flatten layer, and fully connected layer are examples for these layers.

The pooling layers usually are placed after the convolutional layers to condense feature maps which are created during the convolution operations. Even though there are different kinds of pooling operations, the most common one is max-pooling. In max-pooling, a predefined pooling unit moves along the feature map and outputs the maximum activation in its region [17].

Dropout is a popular regularization technique to prevent the network from memorization of the data called overfitting. The dropout layer sets some feature outputs to zero during the training process with a given dropout rate [18, 19].

In CNN models, each layer input's distribution changes depending on the previous layer outputs. This situation causes a slow training step, since it requires a small learning rate for the optimizer and the parameter initialization carefully. At this point, the batch normalization layer enables the input of a layer to normalize the data before processing it. Thus, the requirements are dealt with substantially by provided generalization [20].

The flatten layer is used for transforming the feature maps, which are in a multidimensional matrix form, to one dimensional vector for the fully connected layers [21].

At the end of a CNN model, generally, the fully connected layers (dense layers) are used for classification of the input. Each neuron at each fully connected layer was linked to the neurons in the prior and following layers [21].

Another component of CNN is activation functions. These functions add nonlinearity to the model to represent the complex problems and catch the nontrivial relationships in the data. Many activation functions could be used in accordance with the target of the model like sigmoid, tanh, relu, elu, etc [19].

Evaluation of the difference between the target value and the estimated value from a CNN model is shown by a loss function, predefined by the designer. The model tries to minimize this function during the training process.

B. Network Architecture

In the following, we describe our deep neural network architecture for lane detection as depicted in Figure 1. The basis of this architecture is composed of one of reputed CNN architectures which are Lenet5, AlexNet, VGG16, VGG19, ResNet50. After the CNN architecture, the fully connected

layers are available to estimate the line coefficients of the lane to fit second order polynomials.

In 1998, Yann Lecun et al. [22] developed LeNet5 to classify the handwritten digits. It took 32x32 input images and included two convolutional layers. These layers were individually followed by the average pooling layer, and finally there exist fully connected layers. tanh performed as the activation function.

AlexNet, which has five convolutional layers, max-pooling layers, and batch normalization layers, was trained on GPU in
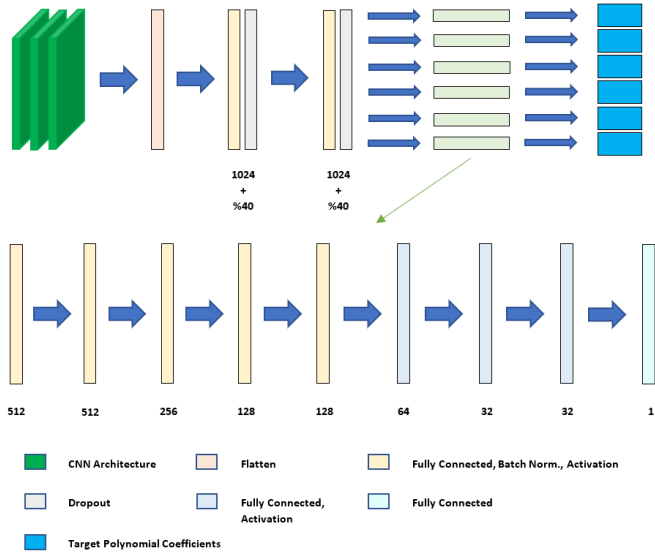

Figure 1. The developed architecture for lane detection

a parallel way using 224x224 input images. This architecture won first place by classifying different objects into 1000 categories with the highest accuracy in the 2012 ImageNet Large Scale Visual Recognition Competition (ILSVRC). relu activation function was used here for the first time [23].

Vision Geometry Group from the University of Oxford invented VGG Net in 2014. Because this CNN architecture has small filters in the convolutional layers compared to previous ones, the network was able to be deeper to extract features from the complex input images without increasing the parameters extremely. The most common VGG Net architectures are VGG16 and VGG19 which are named regarding the total number of the convolutional and fully connected layers [24].

ResNet architecture came up with residual blocks to solve the vanishing gradient problem in the optimization and to get very deep CNN models with fewer parameters, in 2015 [25]. In this study, ResNet architecture with 50 layers is preferred to use.

The designed network architecture had fully connected layers after the CNN part. The first two fully connected layers were followed by the dropout layer with a 40% dropout rate. Then, six parallel fully connected branches process the data to estimate the lane coefficients for each line to fit a second order polynomial. As the activation function relu and elu were chosen for the CNN side and the fully connected side, respectively.

IV. Experiments

In this section, we examined the success of the CNN architectures with the developed fully connected architecture in terms of lane detection.

A. Dataset

To train and test our approach, we did experiments on TuSimple dataset. This dataset was collected from highways in daylight. Figure 2 shows some images from the dataset. The weather was usually sunny and sometimes cloudy. It consisted of 3626 images for the training and 2782 images for the testing [26].

In the experiments, we divided the training set into two parts to make a validation after each training epoch. This validation set was 10% of the training set. The labels of the dataset showed the point coordinates of the lane lines with respect to the image origin.

Figure 2. Some images from TuSimple dataset

B. Preprocess

The original images in the dataset had a resolution of 1280x720. We reduced the size of the images to 160x160 since the original resolution was too high to process in the network regarding the computational cost. The lane line points were scaled with the same ratio of the resolution change due to the change in the size of the images. The points were used for getting the target coefficients for a second order polynomial.

The dataset had images from highway. Thus, multilane lines ranging from two to five existed. In the scope of this study, only the ego lane was examined and so filtered out from the other lanes. Figure 3 demonstrated the ego lane lines with red and blue polylines.

Figure 3. Acquired ego lane lines for TuSimple dataset

Most of the images were taken in clear conditions such as in daylight, without shadows or extreme illumination changes. This situation was not good for the generalization of the training process, since it would be biased to a clear view of the camera. Hence, we implemented data augmentation for the input images by changing their brightness in some limits before they go into the network as illustrated in Figure 4.
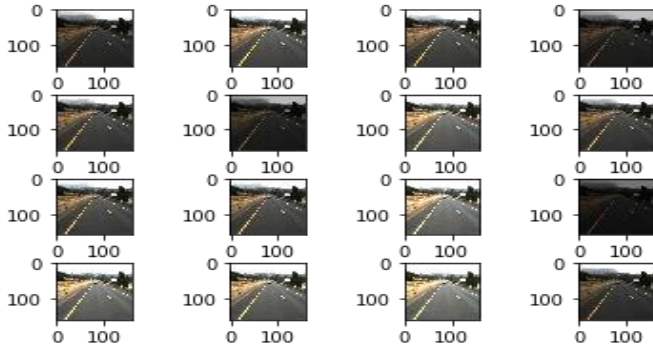

Figure 4. The augmented input data for the developed architecture

C. Training the Network

The designed deep neural network was composed of two parts which were the CNN architecture and the parallel fully connected architectures. The abovementioned CNN architectures were put into the first part for each training process. They were compared in terms of performance and accuracy. Estimation of the designed network was compared with the target coefficients with mean squared error loss function using RMSprop optimizer. The loss function represented the average of all the coefficients error. The learning rate of the optimizer was initialized with 0.001 and decreased after each epoch by 5%. The total number for the epoch was set at 100. If the no changes were observed by a callback function that follows the changes in the loss function during the predefined period, training could be discontinued without waiting for the end of the epochs.

Besides, the effect of batch size was also investigated in this study choosing them of 8, 16 and 32. The loss function changing were depicted in Figure 5 regarding the mentioned batch sizes, respectively.

D. Evaluation Metric

The result of the data testing after the training phase was evaluated by intersection over union (IoU) to measure the similarity between the targets and the test outputs [27]. In this metric, the lane area between the lines, which were represented by second order polynomial's coefficients by the designed architecture, was segmented with white pixels. The region outside the lane was segmented with black pixels as illustrated in Figure 6.
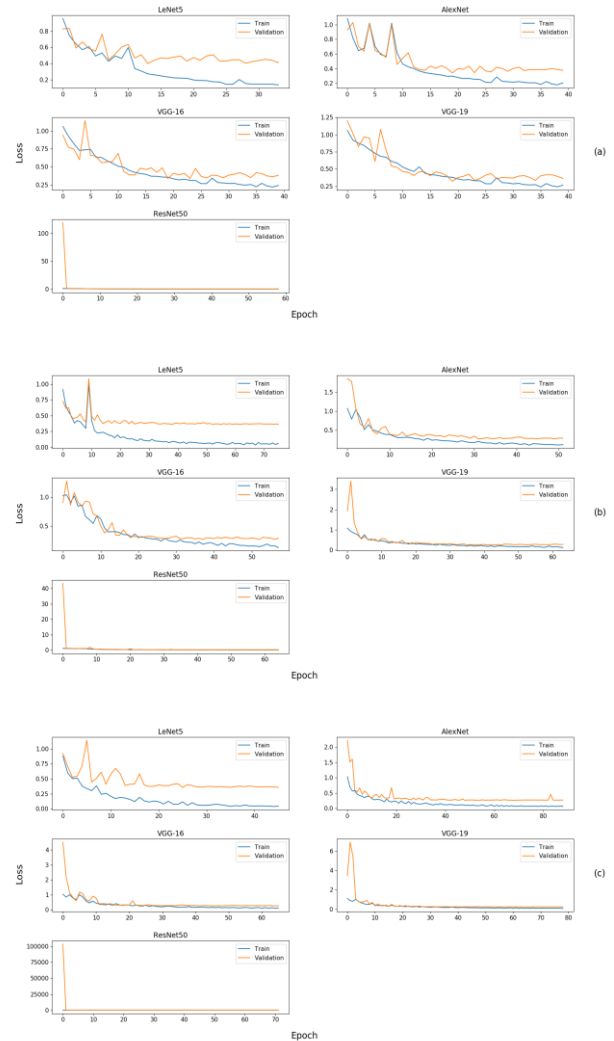

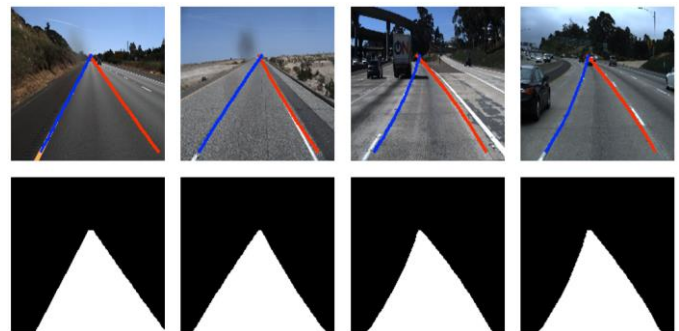Figure 5. Loss function change depending on batch sizes of (a) 8, (b) 16, (c) 32, respectively

Figure 6. Segmented lanes which colored with white pixels

V. EXPERIMENTAL RESULTS

The designed model based on reputed CNN architectures was tested on 2782 test images of TuSimple dataset. The performance of this model was calculated by taking the average of the evaluation metric for all the test images. In addition to this, the effect of batch size was considered for the CNN architectures individually. The results were compared with each

other in Table 1. The most successful experiment results, which belong to ResNet50 architecture base by a batch size of 32, were depicted in Figure 7 as the detected lane area using green color.

TABLE I
COMPARATIVE RESULTS of CNN ARCHITECTURES

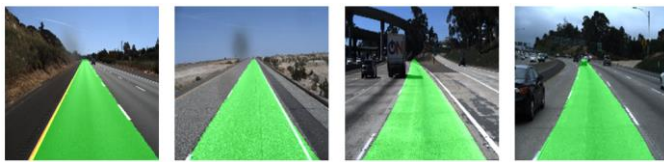| CNN BASE	Batch Size	Epoch Number	IoU Score
Lenet5	8	34	**0.86518**
AlexNet	8	40	0.84630
VGG16	8	40	0.85010
VGG19	8	40	0.85531
ResNet50	8	59	0.85607
Lenet5	16	76	0.85135
AlexNet	16	52	0.84399
VGG16	16	58	0.87786
VGG19	16	64	**0.89115**
ResNet50	16	65	0.87930
Lenet5	32	46	0.87737
AlexNet	32	89	0.82226
VGG16	32	66	0.87183
VGG19	32	79	0.87273
ResNet50	32	72	**0.89570**

Figure 7. ResNet50 outputs for lane detection by the batch size of 32

VI. CONCLUSIONS

In this paper, a CNN-based lane detection deep neural network model was proposed. In comparison with most deep learning-based lane detection methods, which output the lane area by segmentation, the developed model gives more crucial lane line coefficients for advanced driver assistance keeping the care safely in the lane. Our experiments showed that CNN architectures played an active role in lane detection regarding their complexity to extract more sophisticated image features. Even though LeNet5 is an outdated architecture, it gave good results for some cases. Deeper architectures such as VGGNet and ResNet could detect the lane more accurately. It was observed that the batch size influenced the detection accuracy, and about 90% IoU score was taken with ResNet50 by the batch size of 32. The batch size also affected the number of epochs, which was limited to 100, utilizing an early stop callback function in a direct proportion.

Future studies extending to multi-lane detection and adding on other CNN architectures are required to develop a real-time application on a car with a computer like NVIDIA TX2.

REFERENCES

[1] Y. Xing, C. Lv, L. Chen, H. Wang, H. Wang, D. Cao, E. Velenis, F. Wang, "Advances in vision-based lane detection: Algorithms, integration, assessment, and perspectives on ACP-based parallel vision," IEEE/CAA Journal of Automatica Sinica, Vol. 5, No. 3, 2018, pp. 645-661.

[2] C. Kreucher, S. Lakshmanan, "LANA: A lane extraction algorithm that uses frequency domain features," IEEE Transactions on Robotics and Automation, Vol. 15, No. 2, 1999, pp. 343-350.

[3] J. M. Collado, C. Hilario, A. de la Escalera, J. M. Armingol, "Adaptative road lanes detection and classification," Advanced Concepts for Intelligent Vision Systems: 8th International Conference, Antwerp, Belgium, 2006.

[4] A. Borkar, M. Hayes, M. T. Smith, S. Pankanti, "A layered approach to robust lane detection at night," 2009 IEEE Workshop on Computational Intelligence in Vehicles and Vehicular Systems, Nashville, US, 2009, pp. 51-57.

[5] R. K. Satzoda, M. M. Trivedi, "Efficient lane and vehicle detection with integrated synergies (ELVIS)," 2014 IEEE Conference on Computer Vision and Pattern Recognition Workshops, Columbus, US, 2014, pp. 708-713.

[6] A. Mammeri, A. Boukerche, Z. Tang, "A real-time lane marking localization, tracking and communication system," Computer Communications, Vol. 73, 2016, pp. 132-143.

[7] S. Jung, J. Youn, S. Sull., "Efficient Lane Detection Based on Spatiotemporal Images," in IEEE Transactions on Intelligent Transportation Systems, Vol. 17, No. 1, 2016, pp. 289-295.

[8] Y. Wang, D. Shen, E. K. Teoh, "Lane detection using spline model," Pattern Recognition Letters, Vol. 21, No. 8, 2000, pp. 677-689.

[9] K. H. Lim, K. P. Seng, L. Ang, "River Flow Lane Detection and Kalman Filtering-Based B-Spline Lane Tracking," International Journal of Vehicular Technology, Vol. 2012, 2012, pp. 1-10.

[10] H. Tan, Y. Zhou, Y. Zhu, D. Yao, J. Wang, "Improved river flow and random sample consensus for curve lane detection," Advances in Mechanical Engineering, Vol. 7, No. 7, 2015.

[11] J. Niu, J. Lu, M. Xu, P. Lv, X. Zhao, "Robust lane detection using two-stage feature extraction with curve fitting," Pattern Recognition, Vol. 59, 2016, pp. 225-233.

[12] A. Gurghian, T. Koduri, S. V. Bailur, K. J. Carey, V. N. Murali, "DeepLanes: End-to-end lane position estimation using deep neural networks," 2016 IEEE Conference on Computer Vision and Pattern Recognition Workshops, Las Vegas, US, 2016, pp. 38-45.

[13] B. He, R. Ai, Y. Yan, X. Lang, "Accurate and robust lane detection based on Dual-View Convolutional Neutral Network," 2016 IEEE Intelligent Vehicles Symposium (IV), Gothenburg, Sweden, 2016, pp. 1041-1046.

[14] S. Lee, J. Kim, J. S. Yoon, S. Shin, O. Bailo, N. Kim, T. Lee, H. S. Hong, S. Han, I. S. Kweon, "VPGNet: Vanishing Point Guided Network for lane and road marking detection and recognition," 2017 IEEE International Conference on Computer Vision (ICCV), Venice, Italy, 2017, pp. 1965-1973.

[15] F. Pizzati, M. Allodi, A. Barrera, F. Garcia, "Lane detection and classification using cascaded CNNs," Computer Aided Systems Theory – EUROCAST 2019, 2020, pp. 95-103.

[16] I. Goodfellow, Y. Bengio and A. Courville, Deep learning, The MIT Press, 2017, p. 330.

[17] M. Nielson, Neural Networks and Deep Learning, Determination press, 2015, p. 174.

[18] N. Srivastava, G. Hinton, A. Krizhevsky, I. Sutskever, R. Salakhutdinov, "{Dropout: A simple way to prevent neural networks from overfitting," Journal of Machine Learning Research, Vol. 15, No. 1, 2014, pp. 1929-1958.

[19] F. Chollet, Deep Learning with Python, Manning, 2017, p.109.

[20] S. Ioffe, C. Szegedy, "Batch Normalization: Accelerating deep network training by reducing internal covariate shift," Proceedings of the 32nd International Conference on International Conference on Machine Learning – Volume 37, Lille, France, 2015, pp. 448-456.

[21] D. Foster, Generative Deep Learning, O'Reilly Media, 2019, p. 38.

[22] Y. Lecun, L. Bottou, Y. Bengio, P. Haffner, "Gradient-based learning applied to document recognition," in Proceedings of the IEEE, Vol. 86, No. 11, 1998, pp. 2278-2324.

[23] A. Krizhevsky, I. Sutskever, G. E. Hinton, "ImageNet classification with deep convolutional neural networks," Proceedings of the 25th

     http://dergipark.gov.tr/bajece

International Conference on Neural Information Processing Systems, Lake Tahoe, US, 2012, pp. 1097-1105.

[24] K. Simonyan, A. Zisserman, "Very deep convolutional networks for large-scale image recognition," International Conference on Learning Representations, 2015.

[25] K. He, X. Zhang, S. Ren and J. Sun, "Deep residual learning for image recognition," 2016 IEEE Conference on Computer Vision and Pattern Recognition (CVPR), Las Vegas, US, 2016, pp. 770-778.

[26] "TuSimple/tusimple-benchmark", GitHub, 2020. [Online]. Available: https://github.com/TuSimple/tusimple-benchmark. Accessed: 17- May-2020

[27] F. V. Beers, A. Lindström, E. Okafor, M. A. Wiering, "Deep neural networks with intersection over union loss for binary image segmentation," Proceedings of the 8th International Conference on Pattern Recognition Applications and Methods, 2019

BIOGRAPHIES

Osman Tahir EKŞİ was born in 1991, in Düzce, Turkey. He received the B.S. degree in Mechatronic Engineering from the University of Kocaeli, Kocaeli, Turkey in 2013. From 2015 and 2017, he worked as a research and development engineer at Semiz Elektronik. In 2018 July, he joined to AVL Turkey and still works here as an autonomous driving development engineer.

G. Gökmen, was born in 1974. He received B.S, M.S and PhD degrees from Marmara University, Istanbul, Turkey. He has been working as a full professor at Marmara University. His current interests are measurement method, signal processing and artificial intelligence techniques.

Circular Antenna Array Synthesis Using Salp Swarm Optimization

A. DURMUŞ

Abstract— **Salp Swarm Algorithm (SSA) is used to design an optimal non uniform circular antenna arrays. Salp Swarm Algorithm which mimics the swarming behavior of salps in oceans is a nature-inspired optimization method. As it is simple and easy to apply, it has been applied to many different problems in the literature. SSA method optimally determined the positions and amplitudes of the circular antenna array elements to obtain radiation patterns with a low maximum sidelobe level (MSL) and narrow half power beam width (HPBW). Different sizes of antennas with 8, 10 and 12 elements are discussed to demonstrate the capability of the SSA algorithm. The results of MSL and HPBW obtained by SSA for the synthesis of circular antenna arrays are better than other compared optimization methods.**

Index Terms— **Salp swarm algorithm, synthesis of antenna array, circular arrays, maximum sidelobe levels.**

I. INTRODUCTION

IN RECENT years, the interest in antenna arrays with high-directionality and gain used in different areas such as wireless communication, mobile, sonar, radar has been increasing. The communication systems performance used in many different applications is highly dependent on the design of the antenna array used. Antenna arrays can be in different structures such as circular, linear and elliptic depending on their geometric structure. Circular Antenna Arrays (CAAs) among these antenna types have become very popular especially in radar, wireless and mobile communication systems. Unlike linear antenna arrays, circular antenna arrays cover all 360° of azimuth coverage [1]. CAAs can scan the main beam in any direction without a major change. Also, CAAs are not affected by the mutual effect because they do not have edge elements [2]. Due to these advantages, the optimum design of CAAs is of great interest in the literature. There has been a lot of research in the last decade on CAAs synthesis, an important computational electromagnetic problem. In [3], a genetic algorithm is used for sidelobes reduction of circular antenna arrays by amplitude and position control. Shihab et al. proposed a particle swarm optimization method for design of CAAs with low sidelobes level [4]. A firefly algorithm is applied for circular array optimization in [5]. In [6], seeker optimization algorithm used

for designing of circular and concentric circular antenna array for sidelobe reduction. Babayigit et.al. implemented Taguchi's optimization method to the synthesis of circular antenna arrays [7]. Hamza et.al. proposed a genetic algorithm to perform the beam steering and null placement in circular arrays [8]. In [9], moth flame optimization used for designing of linear and circular antenna array for sidelobe reduction. Jamunaa et.al proposed a symbiotic organisms search optimisation algorithm to design of a reconfigurable concentric circular array with phase-only controls differentiating the beams [10]. In [11] Multiverse Optimizer (MVO) and modified MVO are used to perform circular antenna array synthesis. Das et.al. proposed gray wolf optimization and particle swarm optimization with a distribution based update mechanism to design of circular arrays [12]. In [13], Electric Charged Particles Optimization is applied to optimal design of circular antenna array for sidelobe level reduction.

In this paper, Salp Swarm Algorithm (SSA) is used to the synthesis of optimum circular antenna arrays. SSA which mimics the swarming behavior of salps in oceans is a nature-inspired optimization method [14]. Since SSA method is an up-to-date optimization technique, there are different studies for SSA in the literature in recent years [14-19]. The amplitudes of the circular antenna array elements are determined by SSA in order to obtain optimum radiation pattern with maximum sidelobe level (MSL) reduction and narrow half power beam width (HPBW). The problem of antenna array synthesis consist of HPBW and MSL constraints. SSA has achieved very good results that meet the constraints. HPBW and MSL values of the array patterns can be easily controlled by using SSA. The results obtained with SSA are compared with the results of other well-known optimization methods. SSA demonstrates better performance to synthesizing circular antenna arrays than the other compared optimization techniques.

The rest of the paper is organized as follows: The problem formulation for circular antenna design is examined in Section 2. In Section 3, the SSA method is explained. Section 4 presents numerical results and conclusions are presented in Section 5.

Ali DURMUŞ, is with Department of Electricity and Energy, Vocational College, Kayseri University, Turkey (e-mail: alidurmus@kayseri.edu.tr).

https://orcid.org/ 0000-0001-8283-8496

II.   PROBLEM FORMULATION FOR CIRCULAR ANTENNA DESIGN

The circular antenna array with M elements is illustrated in Fig. 1. The antenna array elements are non-uniformly placed in a circle with radius a in the x-y plane In Fig. 1.
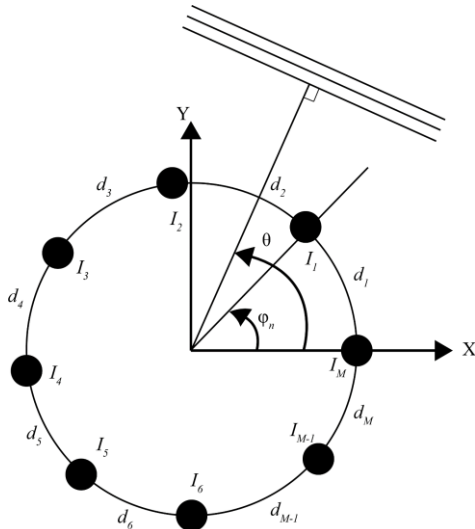

Fig.1: M-elements circular antenna array

Circular antenna array elements are assumed to be isotropic sources with similar properties. The circular antenna array factor is given by [1].

$$AF(\theta) = \sum_{n=1}^{M} I_n \cdot e^{(j.ka.\cos(\theta - \varphi_n) + \alpha_n)} \quad (1)$$

$$ka = \sum_{i=1}^{M} d_i \quad (2)$$

$$\varphi_n = (2\pi \cdot \sum_{i=1}^{n} d_i)/ka \quad (3)$$

$$\alpha_n = -ka \cdot \cos(\theta_0 - \varphi_n) \quad (4)$$

where α_n and I_n are the phase and amplitude values of the n-th array element, respectively. The distance between the two antenna arrays elements is indicated by d_i. k is the number of wave. The angular position of the n-th array element in x-y plane is denoted by φ_n.

The cost function given in Equation 5 is used to designing circular antenna arrays with the decreased HPBW and low MSL values.

$$T_{cost} = W_{SLL} \cdot T_{SLL} + W_{HPBW} \cdot T_{HPBW} \quad (5)$$

where W_{SLL} and W_{HPBW} are the weight factors. T_{SLL} and T_{HPBW} are the functions used for suppressing the MSL and decreasing HPBW values respectively. The function of T_{SLL} can be formulated as follows,

$$T_{SLL} = \int_{-\pi}^{\varphi_{n1}} \beta_{SLL}(\varphi) \cdot d\varphi + \int_{\varphi_{n2}}^{\pi} \beta_{SLL}(\varphi) \cdot d\varphi \quad (6)$$

where φ_{n1} and φ_{n2} are the two angles at the first nulls on each side of the main beam. $\beta_{SLL}(\varphi)$ can be given as follows,

$$\beta_{SLL}(\varphi) = \begin{cases} \gamma_0(\varphi) - SLL_d, & \gamma_0(\varphi) > SLL_d \\ 0, & elsewhere \end{cases} \quad (7)$$

where SLL_d is the desired value of MSL. $\gamma_0(\varphi)$ is the array factor in dB. The function T_{HPBW} can be formulated by

$$T_{HPBW} = \begin{cases} T_o - T_{HPBWmax}, & T_o > T_{HPBWmax} \\ 0, & elsewhere \end{cases} \quad (8)$$

where $T_{HPBWmax}$ and T_o are the desired maximum HPBW and the value of HPBW obtained by SSA, respectively.

III.   SALP SWARM ALGORITHM

The Salp Swarm Algorithm (SSA) is a novel optimization methods proposed by S. Mirjalili, et al. SSA optimization method simulate the swarming behavior of salps in ocean. Salps are living creatures that move by pumping the water in their bodies. The salps move in the depths of the ocean as flocks and these structures are called salp chains. According to the position of the individuals in the salp chain, the salps are divided into two as followers and leaders. The chain of salps is shown in Fig. 2.
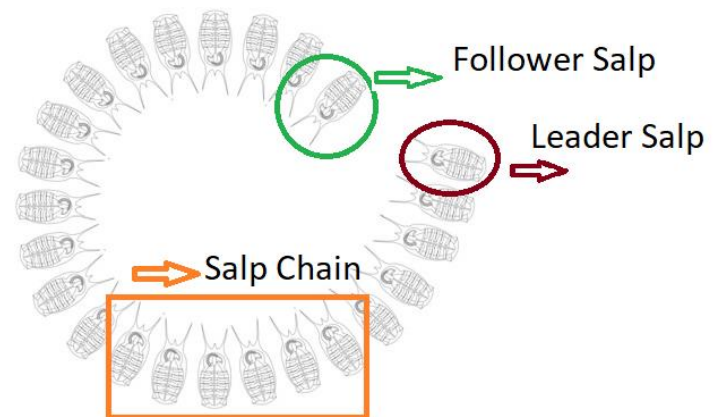

Fig. 2: The chain of salps

The position of each individual in the salps chain is defined in the *n* dimensional solution space. *n* is the number of variables to be solved in the optimization problems. The position of leader salp is updated by using Equation 9 [8].

$$k_i^1 = \begin{cases} x_i + f_1\big((u_i - l_i)f_2 + l_i\big) & f_3 \geq 0 \\ x_i - f_1\big((u_i - l_i)f_2 + l_i\big) & f_3 < 0 \end{cases} \quad (9)$$

where x_i and k_i^1 are the food position and the first salp position in the i-th dimension respectively. l_i and u_i corresponds to lower and upper bound of the i-th dimension. The f_2 and f_3 coefficients are random numbers generated in the range [0,1]. The f_1 coefficient is calculated from the expression below

$$f_1 = 2e^{-\left(\frac{4d}{D}\right)^2} \quad (10)$$

where D and d represent the maximum iterations number and the current iteration number, respectively. The position of the followers are updated by using equation 11.

$$k_i^j = \frac{1}{2}(k_i^j + k_i^{j-1}) \quad (11)$$

Detailed information about SSA is given in the reference [8].

IV. NUMERICAL RESULTS

All simulation studies in this paper were done on a computer with 16 Gb RAM and 2.6 GHz i7 processor. MATLAB is the software program to implement SSA. The population parameter of SSA is fixed to 40. The main goal of circular antenna array synthesis problems is to achieve the lowest MSL and narrowest HPBW values to improve radiation pattern quality. Both position and amplitude values of circular antenna array elements are determined using SSA to achieve the desired radiation pattern with low MSL and narrow HPBW values. Circular antenna arrays with 8, 10 and 12 elements are examined to demonstrate the flexibility and performance of the SSA method.

In the first example, the amplitudes and positions values of circular antenna array with 8 elements are achieved by SSA. The number of maximum iteration is 1000. The radiation pattern obtained by SSA is shown in Fig. 3. The pattern achieved by other four optimization algorithms are also given in Fig. 3.
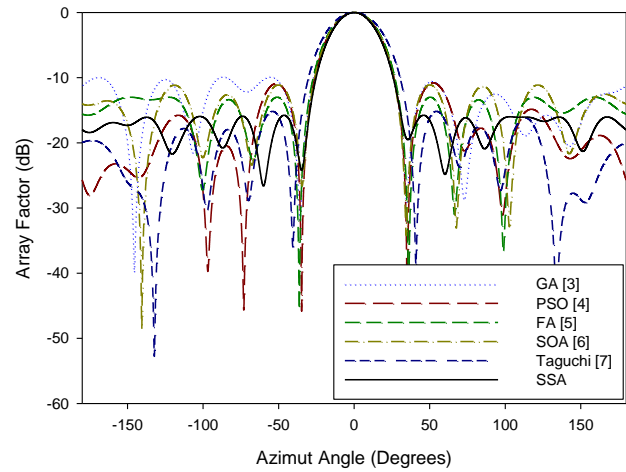

Fig. 3: Radiation pattern of 8-elements circular array.

Table I demonstrates the HPBW and MSL values of the radiation patterns achieved by SSA and other comparison algorithms. According to Fig. 3 and Table I, the MSL and HPBW results obtained by SSA are better than GA [3], PSO [4], FA [5], SOA [6] and Taguchi [7] methods.

TABLE I
COMPARISON OF THE MSL AND HPBW VALUES FOR 8-ELEMENTS CAA DESIGN

Methods	MSL (dB)	HPBW (degrees)
SSA	-15.78	29.90
GA [3]	-9.81	32.22
PSO [4]	-10.80	31.68
FA [5]	-12.99	32.76
SOA [6]	-11.11	31.68
Taguchi [7]	-15.17	36.72

In the second example, circular antenna arrays with 10 elements are considered. The maximum iteration number of SSA is 1000. The radiation patterns obtained by SSA, GA [3], PSO [4], FA [5], SOA [6] and Taguchi [7] are shown in Fig. 4.

Along with the values obtained with SSA, the MSL and HPBW values of GA [3], PSO [4], FA [5], SOA [6] and Taguchi [7] methods are listed for comparison in Table II. The MSL value of radiation pattern achieved by SSA is -15.35 dB. As can be clearly seen from the Figure 4 and Table II, SSA has obtained better MSL value than other optimization methods compared. Also, if we examine the HPBW value, it is seen that the value achieved with SSA is better than the results of Taguchi [7] method.
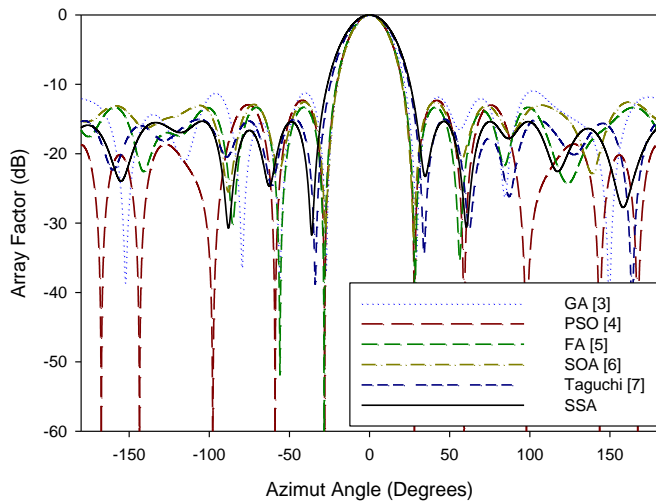
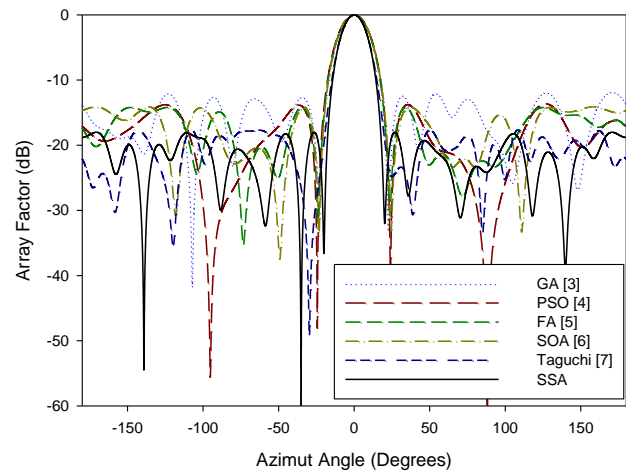Fig. 4: Radiation pattern of 10-elements circular array.

Fig. 5: Radiation pattern of 12-elements circular array.

The convergence curves obtained for 8, 10 and 12 element circular antenna arrays design are given in Fig. 6.

TABLE II
COMPARISON OF THE MSL AND HPBW VALUES FOR 10-ELEMENTS CAA DESIGN

Methods	MSL (dB)	HPBW (degrees)
SSA	15.35	29.11
GA [3]	-10.85	25.56
PSO [4]	-12.30	24.48
FA [5]	-13.30	24.84
SOA [6]	-12.50	24.12
Taguchi [7]	-15.03	29.16

TABLE III
COMPARISON OF THE MSL AND HPBW VALUES FOR 12-ELEMENTS CAA DESIGN

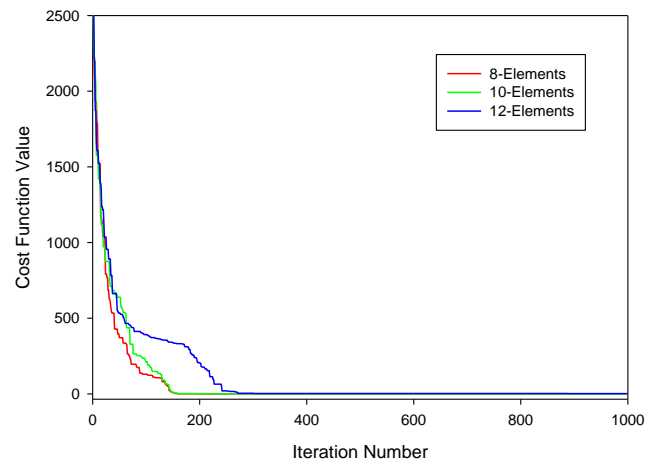| Methods	MSL (dB)	HPBW (degrees)
SSA	-18.01	16.86
GA [3]	-11.80	20.52
PSO [4]	-13.67	20.88
FA [5]	-14.20	20.52
SOA [6]	-14.11	20.34
Taguchi [7]	-17.68	16.92

Fig. 6: The convergence curve of CAA with 8-elements, 10-elements and 12-elements.

Table IV tabulates the amplitudes and positions values of the circular antenna array with 8, 10, and 12elements.

V. CONCLUSION

In this study, the position and amplitude values of the non-uniform circular antenna arrays having 8, 12, and 20 isotropic elements are optimized by SSA method. The radiation pattern with low MSL and narrow HPBW values are obtained with the proposed SSA algorithm. The results show that SSA is successful in achieving radiation pattern with low MSL and narrow HPBW for circular antenna array synthesis. Generally, the MSL and HPBW values obtained with SSA are better than the other compared algorithms. In addition, by making changes in the algorithm and creating hybrid structures, better results can be obtained in later studies.

In the last example, the SSA technique is used for optimization of the circular antenna array with 12 elements. The number of maximum iteration is has been set to 1000 to find optimum solution. The radiation pattern obtained after optimizing the position and amplitude values of the circular arrays with SSA is shown in Fig. 5. MSL and HPBW values of the radiation patterns are given in Table III comparatively. As can be clearly seen from Table III, the MSL and HPBW values obtained by SSA are better than that obtained by other compared algorithms.

TABLE IV
THE AMPLITUDE AND POSITION VALUES OF NON-UNIFORM CIRCULAR ARRAY WITH 8-ELEMENTS, 10-ELEMENTS, AND 12-ELEMENTS

Number of Elements	Amplitude Values [$I_1, I_2, I_3, ...I_M$]	Inter Element Spacing [$d_1, d_2, d_3, ...d_M$]
8-Elements (Fig. 3)	[0.9369 0.3191 0.3704 0.6591 0.8065 0.3922 1.0000 0.4209]	[0.3710 1.0107 0.3507 0.9704 0.5172 0.9543 1.4366 0.3050]
10-Elements (Fig. 4)	[0.9004 0.3341 0.4454 0.9175 0.9828 0.1128 0.3362 0.9605 0.4788 0.3346]	[0.3543 0.9178 0.3616 1.0000 0.5707 0.8815 0.6296 0.8216 0.3513 0.0010]
12-Elements (Fig. 5)	[0.5539 0.6489 0.2849 0.5421 0.3916 0.8903 0.9871 0.5434 0.6610 0.6229 0.5248 1.0000]	[0.5965 1.0456 0.6811 0.6726 0.8109 0.4747 0.5074 0.4959 0.9460 1.3183 1.0867 0.5625]

REFERENCES

[1] C. A. Balanis, *Antenna theory: analysis and design,* 3rd edn. Wiley, New York, 2005.

[2] J. R. Mailloux, *Phased array antenna handbook.* Artech House, Boston, 2005.

[3] M. A. Panduro, A. L. Mendez, R. Dominguez, G. Romero. "Design of non-uniform circular antenna arrays for side lobe reduction using the method of genetic algorithms." AEU Int. J. Electron Commun., vol.60.7, 2006, pp. 713–717.

[4] M. Shihab, Y. Najjar, N. Khodier. "Design of non-uniform circular antenna arrays using particle swarm optimization." J. Electr. Eng., vol. 59, 2008, pp. 216–220.

[5] A. Sharaqa, N. Dib. "Circular antenna array synthesis using firefly algorithm." Int. J. RF Microw. Comput. Eng., vol.24, 2014, pp. 139–146.

[6] K. Guney, S. Basbug. "A parallel implementation of seeker optimization algorithm for designing circular and concentric circular antenna arrays." Appl. Soft Comput. vol.22, 2014, pp. 287–296.

[7] B. Babayigit, E. Senyigit. "Design optimization of circular antenna arrays using Taguchi method." Neural Computing & Application, vol. 28, 2017, pp.1443-1452.

[8] A. Hamza, H. Attia, "Fast Beam Steering and Null Placement in an Adaptive Circular Antenna Array." IEEE Antennas and Wireless Propagation Letters, vol. 19, 2020, pp. 1561-1565.

[9] A. Das, D. Mandal, S.P. Ghoshal, R. Kar. "Moth flame optimization based design of linear and circular antenna array for side lobe reduction." International Journal of Numerical Modelling: Electronic Networks, Devices and Fields, vol. 32, 2019, pp.1-15.

[10] D. Jamunaa, F. N. Hasoon, G. K. Mahanti. "Symbiotic organisms search optimisation algorithm for synthesis of phase-only reconfigurable concentric circular antenna array with uniform amplitude distribution." International Journal of Electronics Letters, 2019, pp. 1-12.

[11] A. E. Taser, K. Guney, E. Kurt. "Circular Antenna Array Synthesis Using Multiverse Optimizer." International Journal of Antennas and Propagation, 2020.

[12] A. Das, D. Mandal, R. Kar. "An optimal circular antenna array design considering mutual coupling using heuristic approaches." International Journal of RF and Microwave Computer-Aided Engineering, 2020, pp. 1-14.

[13] H. R. E. H Bouchekara. "Electric Charged Particles Optimization and its application to the optimal design of a circular antenna array." Artificial Intelligence Review, 2020, pp. 1-36.

[14] S. Mirjalili, A. H. Gandomi, S. Z. Mirjalili, S. Saremi, H. Faris, S. M. Mirjalili. "Salp Swarm Algorithm: A bio-inspired optimizer for engineering design problems." Advances in Engineering Software, vol. 114, 2017, pp. 163-191.

[15] H. Faris, M. Mafarja, A. Heidari, I. Aljarah, A. Al-Zoubi, S. Mirjalili, et al. "An efficient binary salp swarm algorithm with crossover scheme for feature selection problems. " Knowledge-Based Systems, vol. 154, 2018, pp. 43–67.

[16] R. Abbassi, A. Abbassi, A. Heidari, S. Mirjalili. "An efficient salp swarm-inspired algorithm for parameters identification of photovoltaic cell models." Energy Conversion and Management, vol. 179, 2019, pp. 362–372.

[17] E. E. Elattar, S. K. ElSayed. "Probabilistic energy management with emission of renewable micro-grids including storage devices based on efficient salp swarm algorithm." Renewable Energy, vol. 153, 2020, pp. 23-35.

[18] X. Zhao, P. Wu, X. Yin. "A quadratic penalty item optimal variational mode decomposition method based on single-objective salp swarm algorithm." Mechanical Systems and Signal Processing, vol. 138, 2020, p. 106567.

[19] W. Liu, R. Wang, J. Su. "An Image Impulsive Noise Denoising Method Based on Salp Swarm Algorithm." International Journal of Education and Management Engineering, vol. 10, 2020, p. 43.

Ali DURMUŞ was born in Kayseri, Turkey in 1980. He received the B.Sc., M.Sc. and Ph.D. degrees, all in Electrical and Electronics Engineering, from Erciyes University, Kayseri Turkey in 2003, 2005, and 2016 respectively. He served as a lecturer at the Department of Electricity and Energy, Erciyes University from 2010 to 2018.   Currently he is an assistant professor at the Department of Electricity and Energy, Kayseri University. His research interests are antennas, antenna arrays, meta-heuristic algorithms, and computational electromagnetics.

Optimizing Connected Target Coverage in Wireless Sensor Networks Using Self-Adaptive Differential Evolution

O. GOKALP

Abstract—**Wireless Sensor Networks (WSNs) are advanced communication technologies with many real-world applications such as monitoring of personal health, military surveillance, and forest wildfire; and tracking of moving objects. Coverage optimization and network connectivity are critical design issues for many WSNs. In this study, the connected target coverage optimization in WSNs is addressed and it is solved using the self-adaptive differential evolution algorithm (SADE) for the first time in literature. A simulation environment is set up to measure the performance of SADE for solving this problem. Based on the experimental settings employed, the numerical results show that SADE is highly successful for dealing with the connected target coverage problem and can produce a higher performance in comparison with other widely-used metaheuristic algorithms such as classical DE, ABC, and PSO.**

Index Terms—**Connected Target Coverage, Metaheuristics, Optimization, Self-Adaptive, Wireless Sensor Networks.**

I. INTRODUCTION

A WIRELESS SENSOR Network (WSN) is one of the most widely used advanced communication technologies and have numerous application areas such as personal health monitoring [1], military surveillance [2], forest wildfire monitoring [3], air pollution monitoring [4], and moving object tracking [5].

As one of the main design issues in WSN, a sensor deployment plan that places individual sensors in a given region should be provided. A good deployment plan will be useful for coverage maximizing, connectivity maximizing, energy efficiency, and lifetime optimization [6]. Coverage is a fundamental property of every WSN that a network cannot detect events in its environment and may become useless without a sufficient sensing area. Therefore, it is important to increase the total coverage ratio as much as possible. Coverage problems can be divided into two classes, namely area coverage and target coverage that the former aims to cover the whole area of interest, whereas the latter aims to cover some specific points.

OSMAN GOKALP, is with Department of Computer Engineering, Ege University, Izmir, Turkey,(e-mail: osman.gokalp@ege.edu.tr).

https://orcid.org/ 0000-0002-7604-8647

Connectivity is another critical requirement for WSNs, and without it, it is not possible to transfer information, no matter how high the coverage rate is. Two sensors are considered as connected if they can communicate with each other (e.g. send and receive data) either directly or via other sensor nodes. Fully connected networks require the existence of at least one path between any node and the sink node. Sometimes, intermittent connectivity is allowed when mobile sinks are provided to move and collect data from disconnected nodes [7].

As optimal sensor deployment problem for coverage is a hard optimization task, there have been so many studies proposed using metaheuristic algorithms such as Genetic Algorithm [8]–[11], Particle Swarm Optimization (PSO) [12]–[14], Artificial Bee Colony [15], Differential Evolution (DE) [16], [17], and Ant Colony Optimization [18]. However, the main drawback of optimization algorithms is the need for parameter tuning for each problem instance that is dealing with. Because of the fact that offline parameter tuning is an optimization problem itself and is mostly a time-consuming task [19], adaptive tuning or parameter control techniques can be used to overcome this issue.

In this study, self-adaptive differential evolution (SADE) [20], which is one of the main adaptive metaheuristic algorithms in continuous optimization domain, is used to solve the connected target coverage optimization in WSNs for the first time in the literature. The effectiveness of SADE has been analyzed with an experimental study that is based on a simulation environment set up. In addition, the performance of SADE has been compared with other metaheuristic optimization algorithms in the literature. The results obtained showed the effectiveness of using SADE for the purpose of solving the connected target coverage problem for WSNs.

The organization of the remaining sections of this paper is as follows. Section II formulates the connected target coverage problem in WSNs. Then, after reviewing the classical DE and SADE algorithms briefly, Section III defines how to use the SADE algorithm to solve this problem. After that, Section IV clearly explains the simulation environment that has been used to analyze the performance of the algorithm. Finally, Section V concludes the paper and gives some future work directions.

II.   PROBLEM DEFINITION

Let $T = \{t_1 t_2, \dots, t_n\}$ is a set of targets, $S = \{s_1 s_2, \dots, s_k\}$ is a set of sensors. Also, all sensors are identical with each other and each one is capable of sensing objects within its sensing range, r_s. Assume that the elements of S and T are placed on an obstacle-free 2D Euclidean plane. When a target t_i is positioned at (x_i, y_i) and a sensor s_j is positioned at (x_j, y_j). Coverage of target t_i by sensor s_j is calculated as:

$$c(t_i, s_j) = \begin{cases} 1, if\ d(t_i, s_j) \leq r_s \\ 0,\ otherwise \end{cases} \quad (1)$$

Where, $d(t_i, s_j)$ is the Euclidean distance between target t_i and sensor s_j, i.e. $\sqrt{(x_i - x_j)^2 + (y_i - y_j)^2}$.

A target is accepted as covered if it is sensed by at least one sensor:

$$cov(t_i) = \begin{cases} 1,\ if\ \sum_{j=1}^{k} c(t_i, s_j) \geq 1 \\ 0,\ otherwise \end{cases} \quad (2)$$

Another important property of each sensor is its communication range r_c that two sensors can communicate with each other only if the distance between them is within the r_c as:

$$con(s_i, s_j) = \begin{cases} 1, if\ d(s_i, s_j) \leq r_c \\ 0,\ otherwise \end{cases} \quad (3)$$

A solution $S = \{s_1 s_2, \dots, s_k\}$ that offers a deployment plan for all sensors is valid if it is connected, i.e. there is at least one communication path between all pairs of sensors.

The goal of the problem is to find a valid (connected) solution that maximizes the target coverage ratio which is expressed as below:

$$CR = \frac{\sum_{i=1}^{n} cov(t_i)}{n} \quad (4)$$

Fig 1 demonstrates the example of WSN deployment with 3 sensors and 5 targets. Sensors s_1 and s_2 are connected with each other since they are positioned inside their r_c. On the other hand, sensor s_3 is not connected with s_1 and s_2, because both of them are outside of its r_c. So, this is an example of an unconnected WSN deployment plan. In addition, 3 of the 5 targets are covered since they are located within r_s of at least one of the sensors, whereas the remaining 2 are uncovered as they cannot meet this condition.

III.   SOLVING THE PROBLEM WITH SADE

A. Review of DE and SADE Algorithms

DE [21] is a population-based metaheuristic algorithm that is used to solve continuous optimization problems. Each individual (solution) in the population is a vector of real numbers $\vec{X}_i = x_1, x_2, \dots, x_D$, where $i = 1,2, \dots, NP$ is a solution index, NP is the size of a population, and D is a dimension of a problem. The initial population is generally constructed randomly within the given upper and lower bounds. Then,
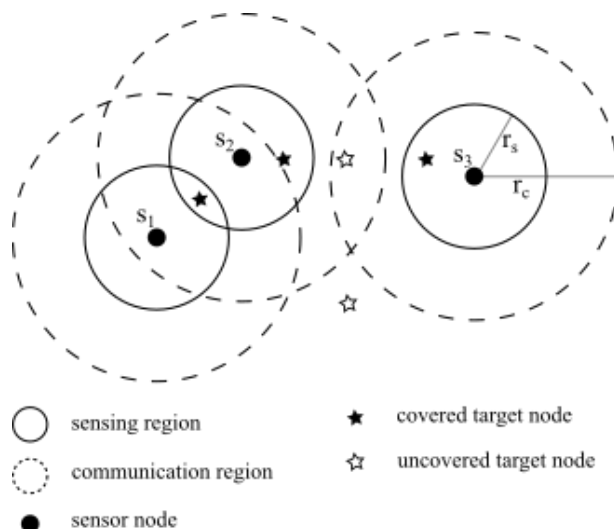

Fig.1. A WSN deployment example with 3 sensors and 5 targets

at each iteration of the search, the following operations are done in order:

- **Mutation**: A mutant solution $\vec{V}_i$ is generated for each individual $\vec{X}_i$, which is also called a target vector, using a mutation strategy. In the basic DE algorithm, DE/rand/bin strategy is applied as follows:

$$\vec{V}_i = \vec{X}_{r1} + F(\vec{X}_{r2} - \vec{X}_{r3}) \quad (5)$$

  Where i is the solution index, F is the differential weight, and $r1, r2$, and $r3$ are random solution indices that are different from each other as well as from i. Therefore, NP must be at least 4 to employ this strategy in the DE algorithm.

- **Crossover**: In crossover operation, each dimension j of the target vector i is tried to be changed and the trial vector $\vec{U}_i$ is generated as follows:

$$\vec{U}_{i,j} = \begin{cases} \vec{V}_{i,j},\ if\ r_{i,j} \leq COR\ or\ j = I \\ \vec{X}_{i,j}, otherwise \end{cases} \quad (6)$$

  Where, $I \in [1, D]$ is the randomly selected dimension index which is used to guarantee the change of at least one of the dimensions, COR is the crossover rate, $r_{i,j}$ is a random number that is selected uniformly in [0,1].

- **Selection**: A trial solution is replaced with the target solution if its fitness value is better:

$$\vec{X}_i = \begin{cases} \vec{U}_i, if\ (\vec{U}_i) \leq f(\vec{X}_i) \\ \vec{X}_i,\ otherwise \end{cases} \quad (7)$$

The self-adapted differential evolution algorithm (SADE) algorithm [20] maintains multiple DE mutation strategies to address optimization problems in different characteristics. Specifically, it includes DE/rand-to-best/2/bin, DE/rand/2/bin, and DE/current-to-rand/1 strategies, which are shown in (8) – (10), respectively, in addition to DE/rand/1/bin strategy, which was previously shown in (5).

$$\vec{V}_i = \vec{X}_i + F(\vec{X}_{best} - \vec{X}_i) + F(\vec{X}_{r1} - \vec{X}_{r2}) + F(\vec{X}_{r3} - \vec{X}_{r4}) \quad (8)$$
$$\vec{V}_i = \vec{X}_{r1} + F(\vec{X}_{r2} - \vec{X}_{r3}) + F(\vec{X}_{r4} - \vec{X}_{r5}) \quad\quad (9)$$
$$\vec{V}_i = \vec{X}_i + K(\vec{X}_{r1} - \vec{X}_{r2}) + F(\vec{X}_{r3} - \vec{X}_{r4}) \quad\quad (10)$$

SADE can select among these 4 strategies adaptively using success and failure memory tables that store successful and unsuccessful applications. That is, the more the strategy leads to an improvement over the current best solution, the more it has a chance to be selected again at later iterations. Furthermore, SADE can also adaptively decide parameter COR by maintaining a list that stores the successful applications of the parameter values. Then, new values of the COR are generated randomly by setting the median value of the list as a mean value of a normal distribution. As for parameter F, the parameter value is determined randomly by using a normal distribution with mean=0.5 and standard deviation=0.3. The interested reader should refer [20] to see other implementation details of this algorithm.

B. Designing Problem-dependent Parts of the Algorithm

Although SADE is a general-purpose numerical optimization method, the structure of solution representation and the fitness function evaluation subjects are left to the algorithm designer. Therefore, this section clearly explains how these algorithm components are designed to solve connected target coverage optimization problems for WSNs.

1) Representation of solutions

A solution to the problem should provide the locations of each individual sensor. In this study, the solution representation is designed as in Fig. 2, where S_i represents the sensor i and x_i and y_i represent the 2D Euclidean coordinates of that sensor. So, the problem dimension $D = 2 \times k$, where k is the total number of sensors.
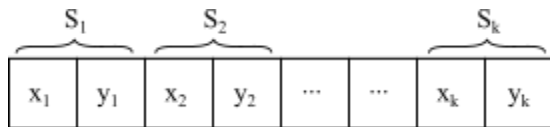

Fig.2. The solution representation

2) Fitness function evaluation

The fitness function evaluates the quality of a solution according to a given problem. In this study, the objective is to maximize the target coverage while preserving the overall network connectivity. So, the fitness function (maximization) is designed to handle these two conditions as in (11):

$$fit = W_1 \times CR + W_2 \times (1.0/CC) \quad (11)$$

Where CR is the coverage ratio, CC is the connected component count (the number of unconnected sub-WSNs), W_1 and W_2 are the weighting factors. As it can be seen from the formula, higher values of CR are rewarded, whereas higher values of CC are penalized. Actually, the maximum fitness value is 2.0 and it is obtained when the full coverage of target points (e.g. $CR = 1.0$) and full connectivity (e.g. $CC = 1$) are both achieved.

The solution will be useless if it does not provide full connectivity, regardless of how high coverage it provides. So,

in order to ensure that the connectivity is achieved first, the fitness function is divided into two phases. In the first phase, the weight settings of $W_1 = 0.0$ and $W_2 = 1.0$ are used for making the algorithm work for only the connectivity purpose. After the connectivity is obtained, the weight settings of $W_1 = 1.0$ and $W_2 = 1.0$ are used for making the algorithm focus on increasing the coverage rate while preserving the connectivity.

IV. SIMULATION RESULTS

A. Simulation Environment

To analyze the performance of SADE for solving the connected target coverage optimization problem in WSNs, the following simulation environment was set up on a computer with Intel® Core™ i7 6700 3.40 GHz CPU using a single core:

- simulation area boundaries: 100 x 100 unit^2
- k (# of sensors): 50, n (# of targets): 100
- deployment of targets: random
- r_s (sensing range): 8
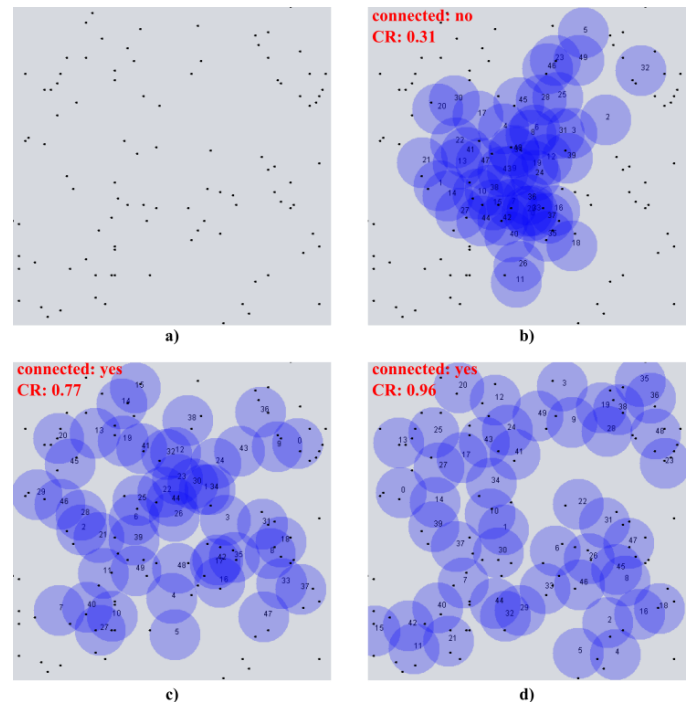- r_c (sensing range): {6, 8, 10, 12, 14}

Fig.3. An example simulation steps for r_c=12. a) initial random positions of target points b) sensor positions after 500 FEs c) sensor positions after 50,000 FEs d) sensor positions after 250,000 FEs

For the implementation of the SADE algorithm, the guidelines in [20] were followed and the NP was set to 50. In addition, the maximum number of function evaluations (FEs) were set to $k \times 5,000$ for each run of the algorithm.

Fig. 3 shows an example of simulation steps with $r_c = 12$. Fig. 3-a shows the positions of target points that were placed randomly in the simulation area. Then, the sensor positions that were produced by the SADE algorithm at different FEs counts are shown in Fig. 3 b-d. It is seen that in earlier iterations of the algorithm, connectivity was not achieved yet. As the iterations passed, the connectivity was provided, and CR was improved.

B. Numerical Results

In this section, the numerical simulation results that were obtained with the SADE algorithm to solve the target coverage problem are provided and discussed. For this purpose, coverage and connectivity performances of the algorithm were measured with different r_c values.

The results obtained for 10 independent runs are presented in Table 1 that CR (Avg.) gives the average coverage rate, CR (S.D.) gives the standard deviation of coverage rates, and "# of succ." gives how many times the algorithm could produce a feasible solution (i.e. fully connected deployment plan).

It is seen from the table that the algorithm is very successful at producing connected solutions with 10/10 success rate, regardless of the communication ranges. The simulation results also reveal that as the communication range is increased the algorithm can produce solutions with higher CR values because it can cover more target points without violating the connectivity constraint. Indeed, when $r_c = 6$, which implies $r_c < r_s$, the CR is around 0.37. It increases to 0.57 when $r_c = r_s$ and can achieve 0.91 with $r_c \geq 1.5 \times r_s$.

TABLE I
SIMULATION RESULTS FOR VARIOUS COMMUNICATION RANGE VALUES

$r_c = 6$	CR (Avg.)	0.37
	CR (S.D.)	0.04
	# of succ.	10/10
$r_c = 8$	CR (Avg.)	0.57
	CR (S.D.)	0.04
	# of succ.	10/10
$r_c = 10$	CR (Avg.)	0.75
	CR (S.D.)	0.03
	# of succ.	10/10
$r_c = 12$	CR (Avg.)	0.91
	CR (S.D.)	0.03
	# of succ.	10/10
$r_c = 14$	CR (Avg.)	0.99
	CR (S.D.)	0.01
	# of succ.	10/10

C. Comparison with Other Optimization Algorithms

This section compares the performance of the SADE algorithm with other common metaheuristic algorithms in the continuous optimization domain. For this purpose the classical version of DE, which uses DE/rand/1/bin strategy, Artificial Bee Colony (ABC) [22], and Particle Swarm Optimization (PSO) [23].

In the experimental work, the population sizes of these 3 algorithms are determined as $NP = 50$, as they will be the same with the SADE algorithm. Also, the results were collected after 10 independent runs per algorithm with the same simulation environment that was defined in Section IV-A. After some preliminary testing, the following parameter values were used for the algorithms compared. For the DE algorithm, $COR = 0.3$ and $F = 0.5$; for ABC algorithm, $limit = (dim \times NP/2)$; and for PSO algorithm $w = 1.0/(2.0 * log_2)$, $c1 = c2 = 0.5 + log_2$, and $K = 3$.

Using the experimental setting above, the computational results obtained are presented in Table 2. One of the major findings is that SADE and PSO are both good at meeting the connectivity condition by producing 10/10 success rates for each r_c value. However, SADE outperforms PSO in terms of coverage rates in all cases. The results also reveal that SADE outperforms basic DE in terms of both CR and success rates. It can be seen that ABC can produce high CR values which are close to SADE, however, this is only valid for higher r_c values. Indeed, the ABC algorithm could not produce feasible solutions with $r_c \leq r_s$. As for the processing times of the algorithms, it is seen that SADE, DE, ABC, and PSO spend around 6.48 s., 6.53 s., 5.36 s., and 9.22 s., respectively. These results suggest that the SADE, DE, and ABC can produce results faster than PSO. Together, the results indicate that the SADE algorithm is preferable to solve the connected target coverage problem in comparison with its competitors that are considered in this experimental study.

TABLE II
COMPARISON THE PERFORMANCE OF SADE WITH OTHER COMMON METAHEURISTICS

		SADE	DE	ABC	PSO
$r_c = 6$	CR (Avg.)	**0.37**	0.28	N/A	0.22
	CR (S.D.)	0.04	0.02	N/A	0.03
	# of succ.	**10/10**	5/10	0/10	**10/10**
	Time (Avg. s.)	6.71	6.91	5.38	8.86
$r_c = 8$	CR (Avg.)	**0.57**	0.40	N/A	0.32
	CR (S.D.)	0.04	0.04	N/A	0.05
	# of succ.	**10/10**	8/10	0/10	**10/10**
	Time (Avg. s.)	6.54	6.87	5.85	9.50
$r_c = 10$	CR (Avg.)	**0.75**	0.53	0.71	0.42
	CR (S.D.)	0.03	0.03	0.09	0.06
	# of succ.	**10/10**	**10/10**	7/10	**10/10**
	Time (Avg. s.)	6.42	6.28	5.30	9.02
$r_c = 12$	CR (Avg.)	0.91	0.65	**0.93**	0.55
	CR (S.D.)	0.03	0.03	0.01	0.05
	# of succ.	**10/10**	**10/10**	**10/10**	**10/10**
	Time (Avg. s.)	6.35	6.30	5.27	8.89
$r_c = 14$	CR (Avg.)	**0.99**	0.76	**0.99**	0.67
	CR (S.D.)	0.01	0.02	0.01	0.06
	# of succ.	**10/10**	**10/10**	**10/10**	**10/10**
	Time (Avg. s.)	6.39	6.29	5.02	9.81

V. CONCLUSION

This paper uses the SADE algorithm to solve the connected target coverage optimization problem in WSNs for the first time in the literature. For this purpose, a fitness function with two stages that consider both connectivity and coverage rate is developed. To measure the performance of the SADE algorithm for solving this problem, the simulation environment was built, and the numerical results were obtained. Based on the experimental settings employed, the numerical results show that SADE is highly successful for dealing with the connected target coverage problem and can provide better performance in comparison with other common metaheuristic algorithms such as classical DE, ABC, and PSO.

Future work might extend this study by considering other variants of self-adaptive differential evolution algorithms such as [24] and [25]. In addition, the problem can be generalized to k-connected coverage variant in which targets must be covered by at least k sensors.

REFERENCES

[1] A. Milenković, C. Otto, and E. Jovanov, "Wireless sensor networks for personal health monitoring: Issues and an implementation," *Computer Communications*, vol. 29, no. 13–14, pp. 2521–2533, Aug. 2006.

[2] L. Lamont, M. Toulgoat, M. Deziel, and G. Patterson, "Tiered wireless sensor network architecture for military surveillance applications," in *The Fifth International Conference on Sensor Technologies and Applications, SENSORCOMM*, 2011, pp. 288–294.

[3] M. A. Jan, P. Nanda, X. He, and R. P. Liu, "A Sybil attack detection scheme for a forest wildfire monitoring application," *Future Generation Computer Systems*, vol. 80, pp. 613–626, Mar. 2018.

[4] W. Yi *et al.*, "A Survey of Wireless Sensor Network Based Air Pollution Monitoring Systems," *Sensors*, vol. 15, no. 12, pp. 31392–31427, Dec. 2015.

[5] Chih-Yu Lin, Wen-Chih Peng, and Yu-Chee Tseng, "Efficient in-network moving object tracking in wireless sensor networks," *IEEE Transactions on Mobile Computing*, vol. 5, no. 8, pp. 1044–1056, Aug. 2006.

[6] S. Abdollahzadeh and N. J. Navimipour, "Deployment strategies in the wireless sensor network: A comprehensive review," *Computer Communications*, vol. 91–92, pp. 1–16, Oct. 2016.

[7] I. Khoufi, P. Minet, A. Laouiti, and S. Mahfoudh, "Survey of deployment algorithms in wireless sensor networks: coverage and connectivity issues and challenges," *International Journal of Autonomous and Adaptive Communications Systems*, vol. 10, no. 4, pp. 341–390, 2017.

[8] Yourim Yoon and Yong-Hyuk Kim, "An Efficient Genetic Algorithm for Maximum Coverage Deployment in Wireless Sensor Networks," *IEEE Transactions on Cybernetics*, vol. 43, no. 5, pp. 1473–1483, Oct. 2013.

[9] T. E. Kalayci and A. Uğur, "Genetic Algorithm-Based Sensor Deployment with Area Priority," *Cybernetics and Systems*, vol. 42[1] T. E, no. 8, pp. 605–620, Nov. 2011.

[10] S. Mnasri, A. Thaljaoui, N. Nasri, and T. Val, "A genetic algorithm-based approach to optimize the coverage and the localization in the wireless audio-sensors networks," in *2015 International Symposium on Networks, Computers and Communications (ISNCC)*, 2015, pp. 1–6.

[11] S. K. Gupta, P. Kuila, and P. K. Jana, "Genetic algorithm approach for k -coverage and m -connected node placement in target based wireless sensor networks," *Computers & Electrical Engineering*, vol. 56, pp. 544–556, Nov. 2016.

[12] X. Wang, S. Wang, and D. Bi, "Virtual Force-Directed Particle Swarm Optimization for Dynamic Deployment in Wireless Sensor Networks," in *Advanced Intelligent Computing Theories and Applications. With Aspects of Theoretical and Methodological Issues*, Berlin, Heidelberg: Springer Berlin Heidelberg, 2007, pp. 292–303.

[13] Q. Ni, H. Du, Q. Pan, C. Cao, and Y. Zhai, "An improved dynamic deployment method for wireless sensor network based on multi-swarm particle swarm optimization," *Natural Computing*, vol. 16, no. 1, pp. 5–13, Mar. 2017.

[14] X. Wang, S. Wang, J.-J. Ma, X. Wang, S. Wang, and J.-J. Ma, "An Improved Co-evolutionary Particle Swarm Optimization for Wireless Sensor Networks with Dynamic Deployment," *Sensors*, vol. 7, no. 3, pp. 354–370, Mar. 2007.

[15] C. Ozturk, D. Karaboga, and B. Gorkemli, "Artificial bee colony algorithm for dynamic deployment of wireless sensor networks," *Turkish Journal of Electrical Engineering & Computer Sciences*, vol. 20, no. 2, pp. 255–262, 2012.

[16] S. Kundu, S. Das, A. V. Vasilakos, and S. Biswas, "A modified differential evolution-based combined routing and sleep scheduling scheme for lifetime maximization of wireless sensor networks," *Soft Computing*, vol. 19, no. 3, pp. 637–659, Mar. 2015.

[17] N. Qin and J. Chen, "An area coverage algorithm for wireless sensor networks based on differential evolution," *International Journal of Distributed Sensor Networks*, vol. 14, no. 8, p. 155014771879673, Aug. 2018.

[18] W.-H. Liao, Y. Kao, and R.-T. Wu, "Ant colony optimization based sensor deployment protocol for wireless sensor networks," *Expert Systems with Applications*, vol. 38, no. 6, pp. 6599–6605, Jun. 2011.

[19] A. E. Eiben, R. Hinterding, and Z. Michalewicz, "Parameter control in evolutionary algorithms," *IEEE Transactions on Evolutionary Computation*, vol. 3, no. 2, pp. 124–141, Jul. 1999.

[20] A. K. Qin, V. L. Huang, and P. N. Suganthan, "Differential Evolution Algorithm With Strategy Adaptation for Global Numerical Optimization," *IEEE Transactions on Evolutionary Computation*, vol. 13, no. 2, pp. 398–417, Apr. 2009.

[21]   R. Storn and K. Price, "Differential Evolution – A Simple and Efficient Heuristic for global Optimization over Continuous Spaces," *J. Global Optim.*, vol. 11, no. 4, pp. 341–359, 1997.

[22]   D. Karaboga and B. Basturk, "A powerful and efficient algorithm for numerical function optimization: artificial bee colony (ABC) algorithm," *J. Global Optim.*, vol. 39, no. 3, pp. 459–471, Oct. 2007.

[23]   M. Zambrano-Bigiarini, M. Clerc, and R. Rojas, "Standard Particle Swarm Optimisation 2011 at CEC-2013: A baseline for future PSO improvements," in *2013 IEEE Congress on Evolutionary Computation*, 2013, pp. 2337–2344.

[24]   J. Zhang and A. C. Sanderson, "JADE: Self-adaptive differential evolution with fast and reliable convergence performance," in *2007 IEEE Congress on Evolutionary Computation, CEC 2007*, 2007, pp. 2251–2258.

[25]   R. Tanabe and A. Fukunaga, "Success-history based parameter adaptation for Differential Evolution," in *2013 IEEE Congress on Evolutionary Computation, CEC 2013*, 2013, pp. 71–78.

BIOGRAPHIES

OSMAN GOKALP was born in 1987. He received the B.S., M.S. and Ph.D. degrees in computer engineering from Ege University in 2010, 2012 and 2018. From 2011 to 2012, he was a research assistant in Yasar University - Department of Software Engineering. Since 2014, he has been a research assistant in Ege University - Department of Computer Engineering. His main research interests include evolutionary computing, metaheuristics and optimization.

Consistency and Comparison of Monomodal Multi-Temporal Medical Image Registration-Segmentation and Mathematical Model for Glioblastoma Volume Progression

E. IRMAK

Abstract—Tumor volume progression analysis and tumor volume measurement are very common tasks in cancer research and image processing fields. Tumor volume measurement can be carried out in two ways. The first way is to use different mathematical formulas and the second way is to use image registration method. In this paper, using 3D medical image registration-segmentation algorithm, multiple scans of MR images of a patient who has brain tumor are registered with different MR images of the same patient acquired at a different time so that growth of the tumor inside the patient's brain can be investigated. Tumor volume progression analysis and tumor volume measurement are performed using image registration technique and the results are compared with the results of tumor volume measurement by mathematical formulas. For the first patient, grown brain tumor volume is found to be 10345 mm³, diminished brain tumor volume is found to be 15278 mm³ and unchanged brain tumor volume is found to be 20876 mm³. Numerical results obtained by image registration model proves that medical image-registration method is not only between the true ranges but also is very close to the best mathematical formula. Medical image registration-segmentation are implemented to 19 patients and satisfactory results are obtained The results are compared with the results obtained from mathematical methods. An advantageous point of medical image registration-segmentation method over mathematical models for brain tumor investigation is that grown, diminished, and unchanged brain tumor parts of the patients are investigated and computed on an individual basis in a three-dimensional (3D) manner within the time.

Index Terms— *Brain tumor growth, Medical image registration, Medical image segmentation, Tumor volume computing.*

I. INTRODUCTION

A. Brain Tumors, Imaging and Importance

BRAIN TUMORS have been announced as one of the most fatal cancers in the western population [1].

EMRAH IRMAK, is with Department of Electrical and Electronics Engineering University of Alanya Alaaddin Keykubat University, Antalya, Turkey, (e-mail: emrah.irmak@alanya.edu.tr)

https://orcid.org/0000-0002-7981-2305

Moreover, Kohler et al. [2] declared that probability of occurrence of primary tumors of the nervous system or brain is 25 per 100,000. By almost a third are malignant and the remaining are benignant or some kind of benignant [3]. World Health Organization (WHO) has introduced a grading scheme which categorizes brain tumors between I and IV. Glioblastoma (WHO grade IV) is known as the most fatal and the most frequent brain tumor which shows very rapid growth [4]. Although treatment methods such as surgery, radiation, chemotherapy are available for treatment of glioblastoma average survival time is 15 months because of the infiltrating nature of glioblastoma [5]. That is why the special care should be given to treatment of glioblastoma. Actually treatment of glioblastoma becomes one of the most challenging fields in oncology [4]. There is a thriving attention and application of glioblastoma progression analysis in clinical diagnostics and analysis. Various researchers have showed that MRI is superior to CT for diagnostic brain imaging [6–9]. Magnetic resonance imaging is a standard and non-invasive technique. The readers who are interested in image processing using glioblastoma MRI images can examine the paper by K. Kaplan et al. [10]. MRI is widely available in clinics. Consequently, MRI in combination with other imaging modalities based studies is more feasible and rational in a clinical point of view. Nevertheless, it should be kept in mind that for a final decision and diagnosis, biopsy and histology are necessary despite the all suitability and practicability of non-invasive imagings. Thanks to the big amount of data, the principal focus of this paper will be on MRI and glioblastoma tumor volume calculation.

It is quite obvious that glioblastoma is a notably deadly disease today and even today's treatment modalities are all around insufficient in curing or even controlling. Glioblastomas are comparatively resistant to X radiation in comparison with other tumor types. Scientists have introduced that most brain tumor recurrence are located within the primary tumor area [11–13]. Although there are studies on measuring the volume of the brain tumor, the definition of tumor volume is still based on time consuming, highly subjective manual outlining by radiologists, clinicians etc. [3]. Today's treatments for glioblastoma ordinarily need tumor removal using surgical

methods followed by irradiation of the tumor source.

B. Literature Survey

Various researchers have studied tumor volume investigation by both measuring and growth analysis [14–19]. Tumor volume measurement is done by a lot of techniques such as 3D I-scan, ultrasonic 3D scanning system, correlation, diameter, height, area calculation etc. These techniques can be mainly categorized into two groups; medical image processing based models and mathematical models [15, 16].

For mathematical models, tumor volume calculation was achieved by using various mathematical formulas [14, 17, 18]. Guthoff [20], for example, made use of area of sphere phenomena, however the usage of that methods were not sustainable now that it was found to be too complicated. Char et al. [14] searched growth rate using an exponential growth model with tumor volume formula. Difference in tumor size with respect to time was considered as growth rate. Li et al. [17] considered the tumor volume as a part of spheroid intersected by a sphere with a very detailed formula. Many researchers believed the change in tumor diameter to be model for the whole brain tumor volume [21–23]. These researchers found it enough to measure only one dimension of the tumor. On the other hand, some researchers measured average of two dimensions [24, 25]. Others considered the volume to be proportional to area and measured tumor area from measurements of two perpendicular diameters. E. Richtig et al. [18] investigated that tumor volume, calculated by the easy to use formula of the half volume of a rotation ellipsoid, rotated around the y-axis, is a better than tumor diameter or tumor height.

For medical image processing based models, a wide range of medical image techniques have been presented with the developments in medical image processing field over the years. As these techniques were independently studied, a large body of research is evolved. As far as it goes there is a wide range of techniques. However, now that every method is designed for a specific application rather than specific types of problems, categorizations and comparison of techniques with each other become difficult. Fortunately, measurement was made using medical image segmentation, medical image registration and the combination of segmentation and registration. Medical image registration with segmentation is very important for monitoring glioblastomas growth during therapy as well as glioblastoma tumor volume measurement. Since the year of 2000, a growing interest and application of medical image processing can be seen from the large number of scientific papers [26–29]. See Figure 1 for frequency of publications in medical image registration field between years 2000 to 2014. Brock et al. [30] used a deformable registration method for tumor registration. The drawback was the substantial processing time. Kaus et al. [31] explored a surface-based registration technique and implemented on human brain. The author achieved a processing time of a few seconds however manually selecting control point was quite complicated and tedious. Maxwell's demons registration was used with lesion growth model by Cuadra et al. [32]. Bloch et al. [33] applied

morphology operators to brain diagnosis. They made use of fuzzy set framework for brain MR images and showed several methods of registration of information. Wavelet based methods are getting increase in medical image registration for brain tumor analysis as well. Quite a lot of studies can be found about registration of medical images using wavelet methods [34–39]. Neural network methods are also very popular in medical image registration field to investigate brain tumor volume analysis using MR images with brain tumor. For example, Ozyurt et al. [28] proposed deep convolutional neural network model to detect glioblastoma (malignant tumor) from brain MRI images. Pohl et al. [40] is a good source about the registration of medical images which have slowly evolving brain tumors. They presented a registration technique that includes registration and segmentation together. Bauer et al. [41] prepared a good survey about medical image registration techniques for the brain tumor volume investigation using MR images. Angelini et al. [42] used affine registration to compute and compare intensity difference maps directly for tumor growth.

C. Motivation

The motivation of this research paper is to design computer aided diagnosis (CAD) system for brain tumor volume measurement and brain tumor screening. Today, brain tumor volume is generally measured by measuring the length and width of the brain using a caliper which is time consuming and prone to manual errors. Although measuring length and width of brain tumor is possible, height measuring is quite problematic because when measuring tumor height, there mainly exists inaccuracy which causes the largest error to volume results. The difficulty is determination where to position the caliper for measuring a precise height measurement. The proposed method is fully automatic by using the software techniques. That is why the proposed method can solve the mentioned problems regarding to measuring the brain tumor volume successfully with the minimum number of errors. There are also other image processing methods for brain tumor volume measurement. The proposed method is superior to other methods because it does not only measure the tumor volume but also growing, diminishing and unchanged tumor parts.

The rest of this paper is organized as follows. Introduction to brain tumors and brain tumor volume investigation, calculation (Section 1), Materials and Methods for brain tumor investigation and calculation (Section 2), Experimental Results using various methods with comparison to medical image registration method (Section 3), Conclusion (Section 4).

II. MATERIALS AND METHODS

A. Mathematical Models for Tumor Volume Progression Analysis

For tumor volume evaluation, there exist important mathematical models. Various studies show that three dimensional fundamental shape of brain tumor is hemi-ellipsoid [43]. Three dimensions of the tumor measurement are necessary for tumor volume calculations. These are: *length (L), width (W),*

height (H). Measurement of tumor volume is a very common task in brain cancer research.

Conventional ellipsoid volume is known as;

$$V = \frac{\pi}{6} * (length) * (width) * (height) \qquad (1)$$

Although measuring length and width of brain tumor is possible, height measuring is quite problematic. Because when measuring tumor height, there mainly exists inaccuracy which causes the largest error to volume results. The difficulty is determination where to position the caliper for measuring a precise height measurement [44]. That is why some authors have reduced essential number of dimensions in order to measure tumor volume. John P. Feldman et al. [44] explored a new mathematical method for tumor measurement which uses just two dimensions; length and width. There are other researchers who use two or even one dimension for measuring brain tumor. Table-I shows a lot of mathematical formulas which have been used for tumor volume calculation up to now.
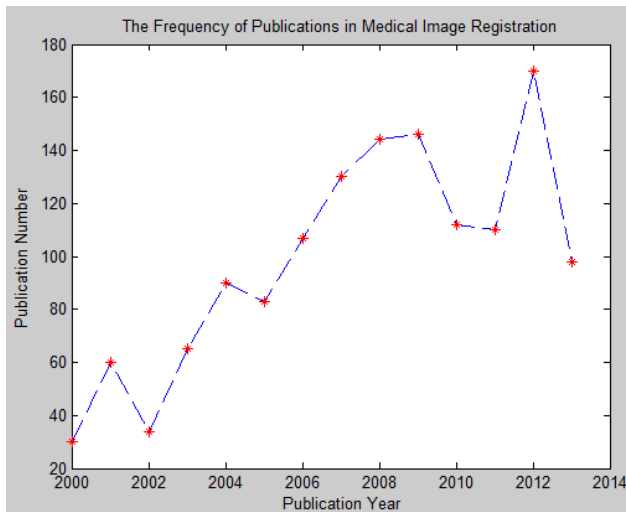
Fig.1. Frequency of papers in Medical Image Registration obtained via ISI

M. M. Tomayko and C.P. Reynolds [45] showed that tumor volume calculation using three-dimensional formula results in the most accurate tumor volume. All the tumor volume measurement formulas are reasonable good at estimating brain tumor but the formula *π/6*(length)*(width)*(height)* stood out as the best.

B. *Medical Image Registration-Segmentation Based Models*

Image registration is a leading-edge for image processing and biomedical engineering fields. Therefore, accurate alignment of the useful information from two or more images is very useful for clinical purposes. Besides, preoperative and intraoperative medical image registration is a critical process for image-guided therapy.

To summarize registration process, Figure 2 is an ideal illustration of how process works. Image which is not changed during registration is called fixed image, the image which is changed, i.e. transformed during registration is called moving image. The purpose of a similarity metric is to return a value

indicating how well two images match [46]. Role of optimizer is to define search strategy for the process. Interpolator takes pixel intensities to the new coordinate system according to the geometric transformation that has been found. Interpolator measures the value of intensity difference between the images in the new positions.

TABLE I
TUMOR VOLUME MEASUREMENT FORMULAS

| Formula Used	Volume Type	Assumption
$\frac{\pi}{6} * L * W * H$	Ellipsoid	3 Dimensions are proportional wrt tumor growth
$\frac{\pi}{6} * L * W^2$	Ellipsoid	H = W
$\frac{\pi}{6} * [\frac{L*W}{2}]^3$	Ellipsoid	$H = \frac{L^2*W^2}{8}$
$\frac{\pi}{6} * (L * W)^{\frac{3}{2}}$	Ellipsoid	$H = \sqrt{L * W}$
$0.4 * L * W^2$	Spheroid	$H = \frac{L^2*W^2}{\pi}$
$\frac{4}{3} * \pi * (\frac{L+W}{2})^3$	Spheroid	$r = \frac{L+W}{2}$
$\frac{4}{3} * \pi * (\frac{L}{2})^3$	Spheroid	$r = \frac{L}{2}$
$L * W * H$	Rectangular Solid	3 Dimensions are proportional wrt tumor growth
$L * W^2$	Rectangular Solid	H = W
$\frac{1}{2} * L * W * H$	Ellipsoid	$\pi = 3$
$\frac{1}{2} * L * W^2$	Ellipsoid	H = W
$L * W$	Areal	Area proportional to volume
$\frac{\pi}{4} * L * W$	Areal	Area proportional to volume
L	Diameter	Diameter to be representative to volume
$\frac{L + W}{2}$	Diameter	Diameter to be representative to volume
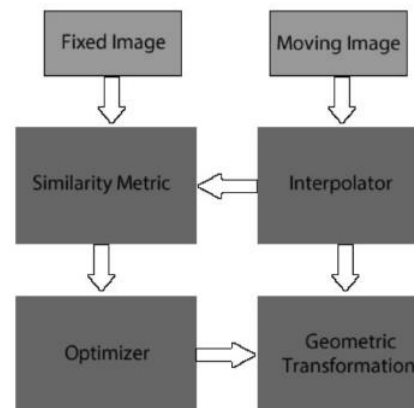
Fig.2. Visual representation of image registration

2.1 Geometrical Transformation

Image registration process has a variety of characteristics. Transformation type is one of the basic characteristic of the image registration in order to properly overlay fixed and moving images. In this section of the paper procedure of selecting the transformation type for our specific application is explained. Affine transformation is an efficient transformation type for this problem now that an affine transformation is composed of a combination of a translation, a rotation, a scale and a shear change. Possible misalignment for MR images taken at different type with the same sensors are translation, rotation scale and shear change.

It is convenient to start by considering linear functions *x, y* and transformations defined by *x* and *y* functions. These transformations might be applied to a point *P(x,y)* within a plane. All linear transformations *T* might be represented using following equations:

$$x' = ax + by + e \qquad (2)$$

$$y' = cx + dy + f \qquad (3)$$

The point *Q(x′,y′)* is called image of *P* under the transformation *T*. It is written as, *Q = T(P)*. Two equations can be written in matrix form as follow:

$$\begin{bmatrix} x' \\ y' \end{bmatrix} = \begin{bmatrix} a & b \\ c & d \end{bmatrix} \begin{bmatrix} x \\ y \end{bmatrix} + \begin{bmatrix} e \\ f \end{bmatrix} \qquad (4)$$

Two equations can also be written as $Q = MP + \vec{v}$, where M and $\vec{v}$ are:

$$M = \begin{bmatrix} a & b \\ c & d \end{bmatrix}, \qquad \vec{v} = \begin{bmatrix} e \\ f \end{bmatrix} \qquad (5)$$

Therefore the product of the matrix *M* and point *P* yields *MP*, and the addition of vector $\vec{v}$ and product *MP* results in a point that is geometrically the transportation of the point by the magnitude and orientation of the vector.

2.2 Similarity Measure

The purpose of using the similarity metric is to measure how similar the two images look to each other. Sum of squared differences (SSD) similarity metric is used as the similarity metric in this study. This metric is commonly used in monomodal intensity based image processing tasks. If the registered images are similar to each other, SSD is a proper similarity metric. In monomodal intensity based image processing processes the registered images are generally similar to each other.

2.2.1 Sum of Squared Differences (SSD)

If A is the Fixed Image and B Moving Image, then the SSD is expressed as follows:

$$SSD = \frac{1}{N} \sum_{i}^{N} |A(I) - B'(I)|^2 , \forall i \in A \cap B' \qquad (6)$$

In this equation *A(i)* is Fixed Image pixel intensity value, *B′(i)* is Moving Image pixel intensity value and *N* is number of pixels of the images.

It was assumed that the fixed image and the moving image are partially similar to each other. They differ from each other's just because of some misalignments and the target is to minimize those misalignments. In theory, when those misalignments are completely corrected, the measure of similarity value (SSD) becomes zero. SSD is used in this study now that brain MR image registered belongs to the same patients which means the registered images are similar to each other except of the misalignments.

2.3 Optimizer

The function of optimizer is to minimize the value of the similarity metric. Therefore, the optimization process ends when the value of the similarity measure is minimum. Consequently, the registration process can be expressed mathematically as follows:

$$min_T D[A(i), T(B(i))] \qquad (7)$$

where

D = Similarity Metric (Cost Function)
$A(i)$ = Fixed Image
$B(i)$ = Moving Image
T = Transformation

2.3.1 Regular Step Gradient Descend Optimizer

Regular Step Gradient Method which was found by Cauchy (1847) is used as the optimization type at this study. This method is very commonly used in medical image registration problems thanks to its simplicity. Cauchy was the first to make use of the negative gradient direction in 1847 for minimization problems. In this method an initial trial point X_1 is chosen, which is iteratively moved along the steepest descent direction until the minimum point is found. Theoretically this method will not terminate unless a stationary point is found. We calculate the difference function at all points in a small (say, 3x3) neighborhood of X_k and takes as the next guess X_{k+1} that point which minimizes the difference function.

2.3.2 Color Based Image Segmentation of Grown, Diminishing and Unchanged Tumor Parts using L*a*b* Color Space

In CIE L*a*b* color space, the vertical axis $L*$ stands for ''Lightness or Luminosity'' and its range is 0-100. The first horizontal axis which is represented by $a*$ stands for colors fall along the red-green axis. The idea is that a color cannot be both red and green [47]. In practice its range is from -128 to +127 (256 levels). The $a*$ axis is red at one end (indicated by +a), and green at the other end (indicated by -a). The other horizontal axis which is represented by $b*$ stands for colors fall along the blue-yellow axis. The idea is again that a color cannot be both blue and yellow. In practice its range is from -128 to + 127 (256

levels). The $b*$ axis is yellow at one end (indicated by +b), and blue at the other end (indicated by -b). The origin of each axis is 0. A value of 0 or very low numbers of both $a*$ and $b*$ will define a neutral or near neutral. $a*$ and $b*$ layers contain color information whereas $L*$ layer contains luminosity (lightness) information [48].

Considering all the properties and advantages of *CIE L*a*b** up to now, it can be concluded that the difference between the two points in the *CIE L*a*b** color space is same with the human visual system. Therefore, after image registration process, obtained medical images are converted to *CIE L*a*b** from *RGB* color space. Conversion from *XYZ* color space to CIE *L*a*b** color space is achieved using the equation 8-9.

$$\begin{pmatrix} L^* = 116f\left(\frac{Y}{Y_n}\right) - 16 \\ a^* = 500\left[f\left(\frac{X}{X_n}\right) - f\left(\frac{Y}{Y_n}\right)\right] \\ b^* = 200\left[f\left(\frac{Y}{Y_n}\right) - f\left(\frac{Z}{Z_n}\right)\right] \end{pmatrix} \tag{8}$$

where,

$$f(t) = \begin{cases} t^{1/3}, & t > \left(\frac{6}{29}\right)^3 \\ \frac{1}{3}\left(\frac{29}{6}\right)^2 t + \frac{4}{29}, & otherwise \end{cases} \tag{9}$$

X, Y and Z are the coordinates of *XYZ* color space. X_n, Y_n, and Z_n are *XYZ* tristimulus values of the reference white point. The subscript n stands for ''normalized''. The reason for partition off $f(t)$ function is to prevent an infinite slope at $t = 0$.

2.3.3 Color Differences, Delta E Differences and Tolerances
In this study color difference is used to segment grown, diminishing and unchanged tumor parts from rest of the image and from each other as well after images are registered. Color difference is a well-advised technique to compute difference (distance) between two colors in color based image segmentation science. Color difference is a kind of metric which actually provides Euclidean distance. Delta E was defined by The International Commission on Illumination (CIE) and represented by *ΔE* which generally indicates color difference. The higher the *ΔE*, the bigger the difference between two colors in comparison. Theoretically, for average human vision a *ΔE* less than 1 is said to be indistinguishable on the condition that colors are not adjacent to each other. This means that color difference of less than 1 is hardly distinguishable by average human vision. a *ΔE* value between 3 and 6 is supposed to be moderate [47]. *ΔE* is computed using equation 10.

$$\Delta E = \sqrt{(L_2^* - L_1^*)^2 + (a_2^* - a_1^*)^2 + (b_2^* - b_1^*)^2} \tag{10}$$

(L_1^*, a_1^*, b_1^*) and (L_2^*, a_2^*, b_2^*) are two points having three components: *L*, a*, b** in three dimensional *CIE L*a*b* color space*.

Tolerance means that how a set of colors is close to a specified reference point. Now that the distance in *L*a*b** color space is perceptually uniform, tolerance will be defined as the set of colors whose difference to the reference point is smaller than noticeable-difference threshold. This tolerance value will specify the cluster of similar colors, i.e. pixel values. Tolerance value is a quality control for segmenting colors from each other, hence shows difference (distance) for color and lightness.

The whole process including image registration and image segmentation is summarized as follows:

Proposed Algorithm:
Step 1: Read the patient's MR image with brain tumor taken at a previous time and save as Fixed Image. Read the patient's MR image with brain tumor taken at a different time and save as Moving Image.
Step 2: Register Fixed and Moving Images using similarity metric and optimizer defined previously.
Step 3: Save Fused (registered) image.
         Repeat Steps 1-3 for all tumor associated MR scans of the patient brain.
Step 4: Convert Fused medical images from *RGB* color space to *CIE L*a*b** color space using equations 8-9. In *CIE L*a*b** color space, the vertical axis $L*$ stands for ''Lightness or Luminosity''. The first horizontal axis which is represented by $a*$ stands for colors fall along the red-green axis. The other horizontal axis which is represented by $b*$ stands for colors fall along the blue-yellow axis.
Step 5: Draw free-hand irregularly shaped region to specify a color (i.e. anatomic parts: grown tumor, diminishing tumor or unchanged tumor).
Step 6: Compute Color Difference (Delta E) for every pixel in the image between that pixel's color and the average *CIE L*a*b** color of the drawn region using equation 10.
Step 7: Specify the Tolerance Value according to sensitivity your work needs. Tolerance value is a quality control for segmenting colors from each other, hence shows difference (distance) for color and lightness. This is a number that indicates how close to that color would the user like to be. The algorithm then will find all pixels within that computed Delta E of the color of the drawn region.
Step 8: Categorize each pixel using nearest neighbor idea which tells that the smallest distance means similar colors, hence similar anatomic parts.
Step 9: Create new image that segment the original image by color. Green color shows tumor which has been growing with time. Magenta color, on the other hand, shows tumor which has been diminishing parts with time and lastly white color shows unchanged brain tumors.
Step 10: Compute the area of each color (each anatomic part) in segmented image.
Repeat Steps 4-10 for all Fused (registered) images.

Step 11: Add all the results came from Step 10 to compute volume of grown brain tumor, diminished brain tumor and unchanged brain tumor.

III. EXPERIMENTAL RESULTS

The dataset that is used in this study is a publicly available dataset [49] and is known as RIDER Neuro MRI project from The Cancer Imaging Archive (TCIA) database [50]. This is a cancer research project which aims to collect as much as possible brain MR images of the patients with tumors in the brain. This dataset includes 70,220 MR images taken from 19 patients with recurrent glioblastoma.

Figure 3(left) (Fixed Image) and right (Moving Image) are MR images of a patient brain that has brain tumor. Tumors are marked with red arrows in the associated images. These MR images are taken at two different times. Figure 3(left) and (right) are just one scan of the patient acquired at different times. However, registration process has been applied to all scans which have brain tumor. In this patient 30 scans of the patient brain have brain tumor. Slices thickness between scans is 1mm which is a perfect thickness for tumor analysis. It has been investigated experimentally how the brain tumor grows, specifically which part of the brain tumor grows, diminishes, or un-changes with time.
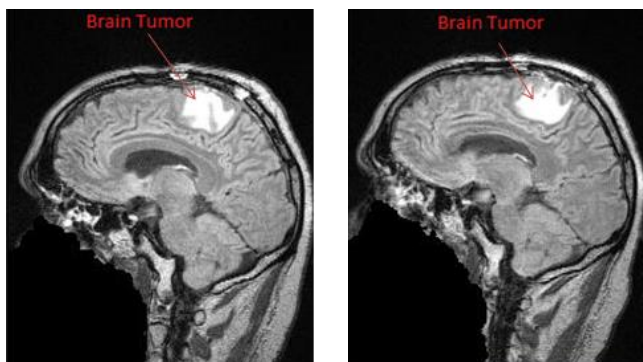
Fig.3. Fixed Image (left) and Moving Image (right)
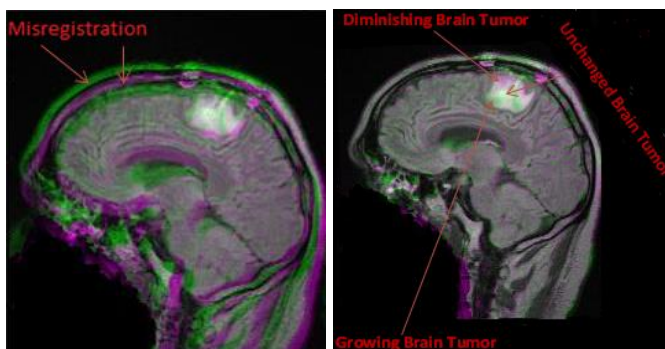
Fig.4. Overlapping (left) and Registration Result (right)

Figure 4(left) is just overlapping of two scans. Misregistration of the scans is quite obvious. Misregistration between two scans is marked with red arrows as well. Figure 4(right) is registration result. In this figure, it can be seen that distortions which is called misregistration is removed. The remaining variations are changes which are of interest; they are therefore not distortions; they are tumor changes which are desired to be detected. These important changes are marked with red arrows. Green parts show tumor which has been growing with time. Magenta parts, on the other hand, shows tumor which has been diminishing parts with time and lastly white parts are unchanged brain tumors. This process has been applied to all 30 scans and results can be seen in Figure 5 and Figure 6.

Segmented tumor after registration process is individually indicated in Figure 5(left). Figure 5(right) is filtering result of segmented tumor image. Figure 5(right) is necessary to compute area (hence volume) of diminished tumor part, growing tumor part and unchanged tumor part on an individual basis.
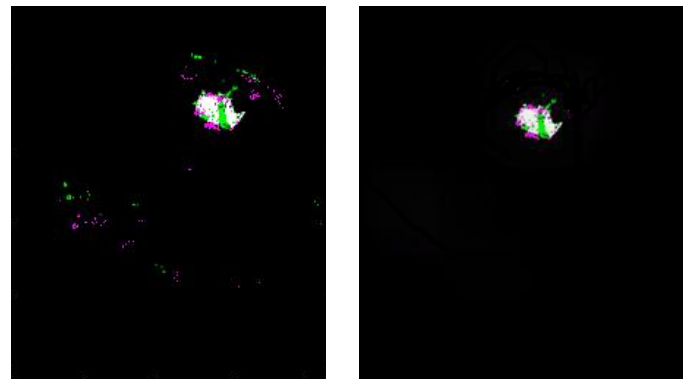

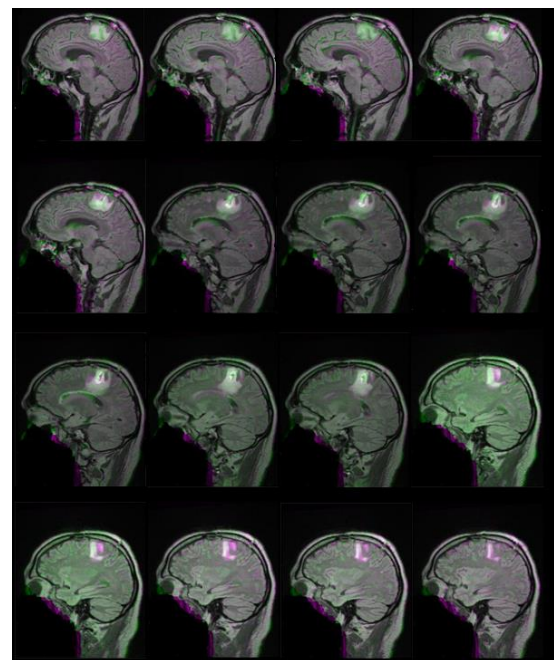Fig.5. Segmented Tumor Before (left) and After Filtering (right)

Fig.6. Segmented Tumor (first patient)

Scores related to SSD metric is tabulated in Table II. When the iteration number increases the better match is achieved. Our rule is that the registration is better when the SSD is lower. Looking at the Table II it is seen that the best match is found at the Iteration Number 86. At 86th iteration number the value of SSD is 286.2024 whereas SSD number starts with 1627.2952 at 1st iteration number. However, the time required for the

registration process increases when the number of iterations increase. Hence registration process takes longer time when iteration number increases.

As stated before the process explained until this point has been implemented to all tumor associated part of the brain. For first patient this number was 30 scans. For demonstration, result of 16 scans is shown in Figure 6 and corresponding tumors are shown in Figure 7.
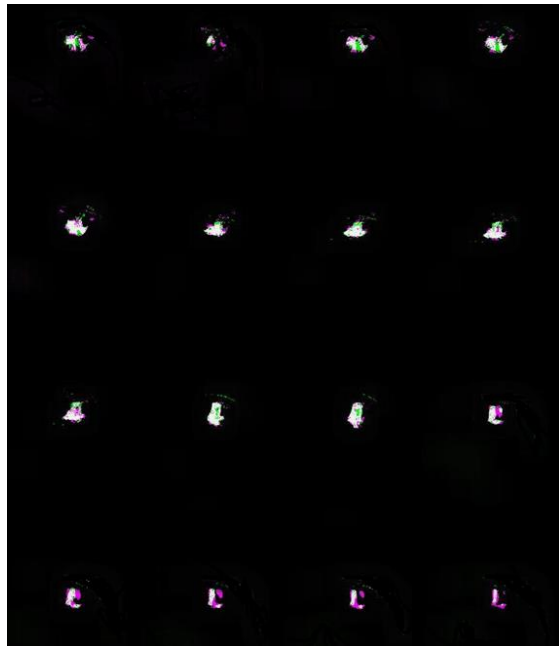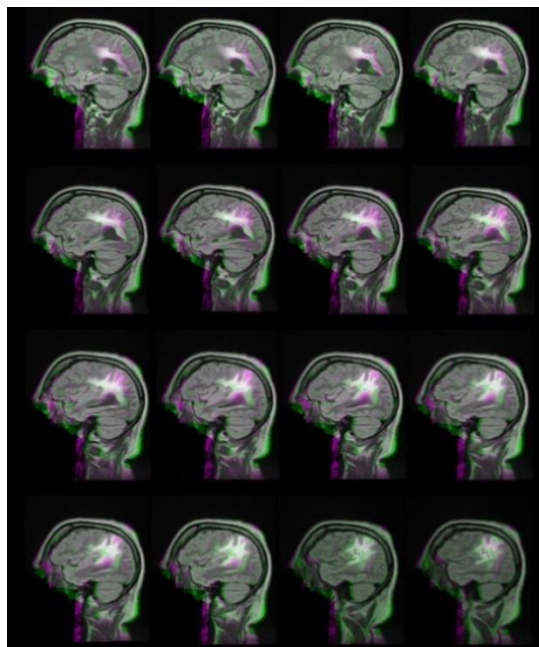

Fig.7. Segmented Tumor (first patient)

Fig.8. Segmented Tumor (second patient)

Results for the second patient are shown in Figure 8 and Figure 9. For second patient, number of scans which are tumor associated part of the brain was 24. Registration process has been applied to 24 scans. For demonstration, result of 16 scans is shown in Figure 8 and corresponding tumors are shown in Figure 9.

TABLE II
SSD RESULTS WITH RESPECT TO ITERATION NUMBER

| Iter.	SSD	Iter.	SSD	Iter.	SSD	Iter.	SSD
1	1627.2952	26	321.2599	51	286.8984	76	287.2046
2	1268.3555	27	317.4207	52	286.8578	77	286.6178
3	1584.4344	28	314.0301	53	286.6623	78	286.5840
4	5242.0876	29	310.8376	54	286.6876	79	286.5539
5	2098.3634	30	307.9623	55	286.7207	80	286.6160
6	1851.5011	31	305.6251	56	286.6427	81	286.5475
7	1525.9047	32	303.2605	57	286.5345	82	286.7101
8	1354.2674	33	300.5287	58	286.5914	83	286.6453
9	834.4523	34	298.3436	59	286.3135	84	286.7862
10	665.7449	35	296.8114	60	286.6338	85	286.8951
11	617.4345	36	294.9558	61	286.2620	86	286.2024
12	584.5832	37	293.3388	62	286.3391	87	CONVERGE
13	550.9578	38	292.7274	63	286.7855	88	CONVERGE
14	520.9090	39	290.8807	64	287.3632	89	CONVERGE
15	489.3432	40	291.0479	65	290.5421	90	CONVERGE
16	461.6606	41	294.3186	66	286.9279	91	CONVERGE
17	432.3264	42	301.4828	67	286.4376	92	CONVERGE
18	409.9917	43	302.8219	68	286.2334	93	CONVERGE
19	386.5456	44	290.8027	69	286.2593	94	CONVERGE
20	386.8915	45	287.8876	70	286.3713	95	CONVERGE
21	484.6777	46	287.7257	71	286.3901	96	CONVERGE
22	579.0272	47	287.5535	72	286.4022	97	CONVERGE
23	433.4253	48	287.3056	73	286.4613	98	CONVERGE
24	338.2038	49	287.1376	74	286.8364	99	CONVERGE
25	325.1858	50	287.1037	75	286.6227	100	CONVERGE
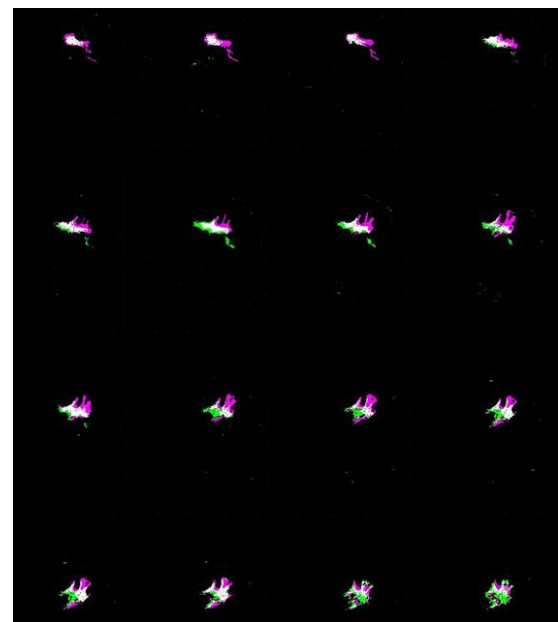
Fig.9. Segmented Tumor (second patient)

Table III shows volume measurement results for both mathematical models and medical image registration model. Table III is comparison of the proposed method with other

standard methods. For tumor volume evaluation, there exist important mathematical models. Various studies show that three dimensional fundamental shape of brain tumor is hemi-ellipsoid. Table III shows results for 12 mathematical formula and medical image registration-segmentation method. Through these mathematical formulas $\pi/6*L*W*H$ is the most used formula for tumor size variation volume measurement. Results of mathematical formulas can vary from formula to formula. Results of tumor volume vary between 72654 mm³ and 16474 mm³. Through these mathematical formulas $\pi/6*L*W*H$ is the most used formula for tumor size variation volume measurement and with this formula result is found to be 36659 mm³. Medical image registration-segmentation result is found to be 36154 mm³. This proves that medical image-registration

method is not only between the true ranges but also is very close to the best formula. In reality medical image registration-segmentation formula gives better result than all mathematical formulas including $\pi/6*L*W*H$ formula. The reason is that all mathematical formulas make some assumption when measuring tumor volume. However medical image registration-segmentation method does not make any assumption. It computes each MR scan with 1 mm thickness and adds all results to compute volume. This gives the most real volumes for tumor. Besides, growing tumor part, diminishing tumor part and unchanged tumor part are also possible just for medical image registration-segmentation method.

TABLE III
TUMOR VOLUME MEASUREMENT RESULT

Formula Used	Previous Tumor Volume (mm³)	Current Tumor Volume (mm³)	Growing Tumor Volume (mm³)	Diminishing Tumor Volume (mm³)	Unchanged Tumor Volume (mm³)	Difference (mm³)
Medical Image Registration-Segmentation Method	36154	31221	10345	15278	20876	(-) 4933
$\frac{\pi}{6} * L * W * H$	36659	31653	N/A	N/A	N/A	(-) 5006
$\frac{\pi}{6} * L * W^2$	34709	27689	N/A	N/A	N/A	(-) 7020
$\frac{\pi}{6} * \left[\frac{L*W}{2}\right]^3$	46678	41601	N/A	N/A	N/A	(-) 5077
$\frac{\pi}{6} * (L*W)^{\frac{3}{2}}$	46689	41673	N/A	N/A	N/A	(-) 5016
$0.4* L * W^2$	28033	21177	N/A	N/A	N/A	(-) 6856
$\frac{4}{3} * \pi * \left(\frac{L+W}{2}\right)^3$	34543	29762	N/A	N/A	N/A	(-) 4781
$\frac{4}{3} * \pi * \left(\frac{L}{2}\right)^3$	72654	45652	N/A	N/A	N/A	(-) 27012
$L * W * H$	70049	60483	N/A	N/A	N/A	(-) 9566
$L * W^2$	66322	52909	N/A	N/A	N/A	(-) 13423
$\frac{1}{2} * L * W * H$	35024	30241	N/A	N/A	N/A	(-) 4783
$\frac{1}{2} * L * W^2$	33166	26454	N/A	N/A	N/A	(-) 6712
$L * W$	20987	15654	N/A	N/A	N/A	(-) 5333
$\frac{\pi}{4} * L * W$	16474	12288	N/A	N/A	N/A	(-) 4186

TABLE IV
TUMOR SIZE VARIATION RESULTS FOR 19 PATIENTS USING MEDICAL IMAGE REGISTRATION-SEGMENTATION METHOD

Patient Number	Previous Tumor Volume (mm³)	Current Tumor Volume (mm³)	Growing Tumor Volume (mm³)	Diminishing Tumor Volume (mm³)	Unchanged Tumor Volume (mm³)	Difference (mm³)
1. Patient	36154	31221	10345	15278	20876	(-) 4933
2. Patient	24356	21967	3924	6313	18043	(-) 2389
3. Patient	37234	38644	15432	14022	23212	(+) 1410
4. Patient	18465	20087	2223	601	17864	(+) 1622
5. Patient	23987	29647	10002	4342	19645	(+) 5660
6. Patient	34123	31076	9109	12156	21967	(-) 3047
7. Patient	26781	25816	9081	10046	16735	(-) 965
8. Patient	21647	19087	184	2744	18903	(-) 2560
9. Patient	42790	44718	14873	12945	29845	(+) 1928
10. Patient	20043	25098	10055	5000	15043	(+) 5055
11. Patient	34981	30241	7903	12643	22338	(-) 4740
12. Patient	22132	27457	10048	4723	17409	(+) 5325
13. Patient	30483	35654	10531	5360	25123	(+) 5171
14. Patient	38654	33376	11411	16689	21965	(-) 5278
15. Patient	27908	31209	10319	7018	20890	(+) 3301
16. Patient	17592	20982	4237	847	16745	(+) 3390
17. Patient	23879	18231	2485	8133	15746	(-) 5648
18. Patient	30675	26783	11110	15002	15673	(-) 3892
19. Patient	29876	33832	13748	9792	20084	(+) 3956

Results for 19 patients' brain tumor size variation volumes using medical image registration-segmentation method are demonstrated in Table IV.

IV. CONCLUSION

A useful and effective application of medical image registration-segmentation is offered in this paper with comparison of mathematical based methods. Intensity-based medical image registration phenomenon is used in this study. Sum of squared differences metric is used as similarity metric and regular step gradient descent optimizer is used as optimization technique. $L*a*b$ color space image segmentation is used to segment each part of tumor. Tumor growthiness inside the patient's brain is successfully investigated. For the first patient, results are shown in Figure 6 and Figure 7. Grown brain tumor volume is found to be 10345 mm³, diminished brain tumor volume is found to be 15278 mm³ and unchanged brain tumor volume is found to be 20876 mm³. Process is applied to another patient and results are shown in Figure 8, Figure 9. For the second patient, grown brain tumor volume is found to be 11657 mm³, diminished brain tumor volume is found to be 14657 mm³ and unchanged brain tumor volume is found to be 18076 mm³. Technique is implemented to 19 patients and satisfactory results are obtained and demonstrated in Table IV. A very useful aspect of medical image registration-segmentation method for brain tumor investigation is that grown, diminished, and unchanged brain tumor parts of the patients are investigated and computed on an individual basis in a three-dimensional manner within the time. On the other hand, there is no possibility of mathematical based methods to computer grown, diminished and unchanged tumor parts. Mathematical based methods can compute previous tumor volume and next tumor volume. Most mathematical based methods are reasonable for tumor volume measurement but medical image registration is more accurate because it measures actual volume without making any assumptions.

Besides the advantages of the proposed method it also has some restriction. For instance, the input size of the MR images in the dataset must be the same for the registration algorithm to work successfully. In addition, it is still a challenge for the proposed method to deal with low-resolution images. In the future work in this area, the pre-processing image enhancement method may be added to the proposed algorithm. Tumor volume measurement for other organs of the body may be another future work using the proposed method in this paper.

REFERENCES

[1] L.M. DeAngelis, "Brain tumors", Med. Prog. N Engl J Med., 114(1), 2001, 114–123.
[2] B. A. Kohler et al., "Annual report to the nation on the status of cancer, 1975–2007, featuring tumors of the brain and other nervous system", J. Natl. Cancer Inst. 103(9), 2011, 714-736.
[3] G. Mazzara, R. Velthuizen, J. Pearlman, H. Greenberg, H. Wagner, "Brain tumor target volume determination for radiation treatment planning through automated MRI segmentation", Int J Radiat Oncol Biol Phys. 59(1), 2004, 300–312.
[4] F.K. Landeghem et al., "Post-mortem studies in glioblastoma patients treated with thermotherapy using magnetic nanoparticles", Biomaterials. 30(1), 52–57.
[5] D. Krex et al., "Long-term survival with glioblastoma multiforme" Brain, 130(10), 2007, 2596–2606.

[6] R.B. Seither, B. Jose, K.J. Paris, R.D. Lindberg, W.J. Spanos, "Results of irradiation in patients with high-grade gliomas evaluated by magnetic resonance imaging", Am. J. Clin. Oncol., 18(4), 1995, 297–299.

[7] J.M. Caudrelier et al., "MRI definition of target volumes using fuzzy logic method for three-dimensional conformal radiation therapy", Int. J. Radiat. Oncol. Biol. Phys. 55(1), 2003, 225–233.

[8] R.K. T. Haken et al., "A quantitative assessment of the addition of MRI to CT-based, 3-D treatment planning of brain tumors", Radiother. Oncol. 25(2), 1992, 121–133.

[9] E.C. Halperin, G. Bentel, E.R. Heinz, P.C. Burger, "Radiation therapy treatment planning in supratentorial glioblastoma multiforme: an analysis based on post mortem topographic anatomy with CT correlations", Int. J. Radiat. Oncol. Biol. Phys., 17(6), 1989, 1347–1350.

[10] K. Kaplan, Y. Kaya, M. Kuncan, H. M. Ertunc, "Brain tumor classification using modified local binary patterns (LBP) feature extraction methods", Medical Hypotheses, 139 (2020), 109696.

[11] V.S. Khoo, E.J. Adams, F. Saran, J.L. Bedford, J.R. Perks, A.P. Warrington, M. Brada, "A comparison of clinical target volumes determined by CT and MRI for the radiotherapy planning of base of skull meningiomas", Int. J. Radiat. Oncol. Biol. Phys., 46(5), 2000, 1309–1317.

[12] P. Sminia, R. Mayer, "External beam radiotherapy of recurrent glioma: radiation tolerance of the human brain", Cancers (Basel). 4(2), 2012, 379–399.

[13] R.K. Ten Haken, B.A. Fraass, A.S. Lichter, L.H. Marsh, E.H. Radany, H.M. Sandler, "A brain tumor dose escalation protocol based on effective dose equivalence to prior experience", Int. J. Radiat. Oncol. Biol. Phys. 42(1), 1998, 137–141.

[14] D.H. Char, S. Kroll, T.L. Phillips, "Uveal melanoma: growth rate and prognosis", Arch. Ophthalmol. 115(8), 1997, 1014–1018.

[15] J.M. Romero, P.T. Finger, R.B. Rosen, R. Iezzi, "Three-dimensional ultrasound for the measurement of choroidal melanomas", Arch. Ophthalmol. 119(9), 2001, 1275–1282.

[16] T. Grasbon, S. Schriever, J.P. Hoops, A.J. Mueller, "3D-Ultraschall Erste Erfahrungen bei verschiedenen Augenerkrankungen", Der Ophthalmol. 98(8), 2001, 88–93.

[17] W. Li, E.S. Gragoudas, K.M. Egan, "Tumor basal area and metastatic death after proton beam irradiation for choroidal melanoma", Arch. Ophthalmol. 121(1), 2003, 68–72.

[18] E. Richtig, G. Langmann, K. Müllner, G. Richtig, J. Smolle, "Calculated tumour volume as a prognostic parameter for survival in choroidal melanomas", Eye (Lond). 18(6), 2004, 619–623.

[19] Y. Liu, S.M. Sadowski, A.B. Weisbrod, E. Kebebew, R.M. Summers, J. Yao, "Patient specific tumor growth prediction using multimodal images", Med. Image Anal. 18(3), 2014, 555–566.

[20] R. Rask, P.K. Jensen, "Precision of ultrasonic estimates of choroidal melanoma regression" 233(1995), 1995, 777–782.

[21] H. Rubin, P. Arnstein, B.M. Chu, "Tumor progression in nude mice and its representation in cell culture", J. Natl. Cancer Inst. 77(5), 1986, 1125–1135.

[22] H. Rubin, B.M. Chu, P. Arnstein, "Selection and adaptation for rapid growth in culture of cells from delayed sarcomas in nude mice", Cancer Res. 47(2), 1987, 486–492.

[23] S. Karpagam, S. Gowri, "Brain tumor growth and volume detection by ellipsoid-diameter technique using MRI data", Int. J. Comput. Sci. 9(2012), 2012, 121–126.

[24] M.F. Dempsey, B.R. Condon, D.M. Hadley, Measurement of tumor "size" in recurrent malignant glioma: 1D, 2D, or 3D?, AJNR Am. J. Neuroradiol. 26 (2005) 770–776.

[25] A. Talkington, R. Durrett, Estimating tumor growth rates in vivo, V (2014) 1–27.

[26] T. Pala, A.Y. Camurcu, "Design of decision support system in the setastatic colorectal cancer data set and its application", Balkan Journal of Electrical and Computer Engineering 4(1), 2016, 12-16.

[27] H.S. Nogay, T.H. Akinci, "A convolutional neural network application for predicting the locating of squamous cell carcinoma in the lung", Balkan Journal of Electrical and Computer Engineering 6(3), 2018, 207-210.

[28] F. Ozyurt, E. Sert, E. Avci and E. Dogantekin, Brain tumor detection based on Convolutional Neural Network with neutrosophic expert maximum fuzzy sure entropy, Measurement, 147, 106830.

[29] S.E.A. Muenzing, B. Ginneken, K. Murphy, J.P.W. Pluim, "Supervised quality assessment of medical image registration: Application to intra-patient CT lung registration", Med. Image Anal. 16(8), 2012, 1521–1531.

[30] K.K. Brock, L.A. Dawson, M.B. Sharpe, D.J. Moseley, D.A. Jaffray, "Feasibility of a novel deformable image registration technique to facilitate classification, targeting, and monitoring of tumor and normal tissue", Int. J. Radiat. Oncol. Biol. Phys. 64(4), 2006, 1245–1254.

[31] M.R. Kaus, S.K. Warfield, A. Nabavi, P.M. Black, F.A. Jolesz, R. Kikinis, "Automated segmentation of MR images of brain tumors", Radiology, 218(2), 2001, 586–591.

[32] J.P. Thirion, "Image matching as a diffusion process: an analogy with Maxwell's demons", Med. Image Anal. 2(3), 1998, 243–260.

[33] I. Bloch, O. Colliot, O. Camara, T. Géraud, "Fusion of spatial relationships for guiding recognition, example of brain structure recognition in 3D MRI", Pattern Recognit. Lett. 26(4), 2005, 449–457.

[34] B. Alfano, M. Ciampi, G. De Pietro, "A wavelet-based algorithm for multimodal medical image fusion", Int. Conf. Semant. Digit. Media Technol., Springer, 4816(2007), 2007, 117–120.

[35] K. Yuanyuan, L. Bin, T. Lianfang, M. Zongyuan, "Multi-modal medical image fusion based on wavelet transform and texture measure", Control Conf., 2007. Chinese, IEEE, 2007, 697–700.

[36] Q.P. Zhang, M. Liang, W.C. Sun, "Medical diagnostic image fusion based on feature mapping wavelet neural networks", Image Graph. (ICIG'04), Third Int. Conf., IEEE, 2004: pp. 51–54.

[37] Q.P. Zhang, W.J. Tang, L.L. Lai, W.C. Sun, K.P. Wong, "Medical diagnostic image data fusion based on wavelet transformation and self-organising features mapping neural networks, Mach. Learn. Cybern. 2004. Proc. 2004 Int. Conf., IEEE, 2004: pp. 2708–2712.

[38] G. Quellec, M. Lamard, G. Cazuguel, B. Cochener, C. Roux, "Wavelet optimization for content-based image retrieval in medical databases, Med. Image Anal. 14(2), 2010, 227–241.

[39] M. Havaei, A. Davy, D. Warde-Farley, A. Biard, A. Courville, Y. Bengio, C. Pal, P.M. Jodoin, H. Larochelle, "Brain tumor segmentation with deep neural networks", Med. Image Anal. 35(2017), 2017, 18–31.

[40] K.M. Pohl, E. Konukoglu, S. Novellas, N. Ayache, A. Fedorov, I.F. Talos, A. Golby, W.M. Wells, R. Kikinis, P.M. Black, "A new metric for detecting change in slowly evolving brain tumors: Validation in meningioma patients", Neurosurgery. 68(1), 2011, 225–233.

[41] S. Bauer, R. Wiest, L.-P. Nolte, M. Reyes, "A survey of MRI-based medical image analysis for brain tumor studies", Phys. Med. Biol. 58(13), 2013, R97–R129.

[42] E.D. Angelini, J. Delon, A.B. Bah, L. Capelle, E. Mandonnet, "Differential MRI analysis for quantification of low grade glioma growth", Med. Image Anal. 16(1), 2012, 114–126.

[43] K.F. Schmidt, M. Ziu, N.O. Schmidt, P. Vaghasia, T.G. Cargioli, S. Doshi, M.S. Albert, P.M. Black, R.S. Carroll, Y. Sun, "Volume reconstruction techniques improve the correlation between histological and in vivo tumor volume measurements in mouse models of human gliomas", J. Neurooncol. 68(2004), 2004, 207–215.

[44] J.P. Feldman, R. Goldwasser, "A mathematical model for tumor volume evaluation using two-dimensions", Journal Appl. Quant. Methods, 4(4), 2009, 455–462.

[45] M.M. Tomayko, C.P. Reynolds, "Determination of subcutaneous tumor size in athymic (nude) mice", Cancer Chemother. Pharmacol. 24(1989), 1989, 148–154.

[46] X. Du, J. Dang, Y. Wang, S. Wang, T. Lei, "A parallel nonrigid registration algorithm based on B-spline for medical images", Comput. Math. Methods Med. 2016.

[47] P.J. Baldevbhai, R.S. Anand, "Color Image Segmentation for Medical Images using L * a * b * Color Space", J. Electron. Commun. Eng., 1(2), 2012, 24–45.

[48] V.S. Rathore, M.S. Kumar, A. Verma, "Colour based image segmentation using L * A * B * colour space based on genetic algorithm", Int. J. Emerg. Technol. Adv. Eng. 2(6), 2012, 156–162.

[49] D. Barboriak, The cancer imaging archive, doi.org/10.7937/K9/TCIA.2015.VOSN3HN1.

[50] K. Clark, B. Vendt, K. Smith, J. Freymann, J. Kirby, P. Koppel, S. Moore, S. Phillips, D. Maffitt, M. Pringle, L. Tarbox, F. Prior, "The cancer imaging archive (TCIA): Maintaining and operating a public information repository", (2013) 1045–1057. doi:10.1007/s10278-013-9622-7.

BIOGRAPHY

Emrah IRMAK was born in 1988 in Mardin, Turkey. He received the B.Sc. degree and M.Sc. degree in Electrical and Electronics Engineering Department from Gaziantep University, Gaziantep, Turkey, in 2012 and 2014, respectively. Emrah Irmak received the Ph.D. degree in Electrical and Electronics Engineering Department from Karabuk University, Karabuk, Turkey in 2018. He studied as a research assistant in Biomedical Engineering Department in Karabuk University between 2012 and 2019. He is currently an Assistant Professor in Electrical and Electronics Engineering Department in Alanya Alaaddin Keykubat University, Antalya, Turkey. His research interests include medical image processing, signal processing and deep learning.

Numerical Method for Calculations of the Multi-Dielectric Fields Based on Flux Density in High Voltage Power Transformer Apparatus

N. PAMUK

Abstract—**This paper deals with a "combination method" in which the charge simulation method is combined with finite element method, for electric field calculation. The proposed method has the advantages of both charge simulation method and finite element method, while making up of their disadvantages. In the combination method, field is divided into two regions, one covered by the charge simulation method and the other by the finite element method. These two regions are combined using the continuous conditions for potentials and dielectric flux densities at the boundary. The new method could be applied to non-enclosed multi-dielectrics fields, space charge fields, fields with leakage current and so on. Examples of calculation have revealed that the method affords satisfactory calculation accuracy in application to high voltage power transformer apparatuses.**

Index Terms—**Finite element analysis, Optimization, Charge simulation method, Electric field distribution, Power transformer apparatus.**

I. INTRODUCTION

THE ELECTRIC field calculation method has made a marked advance with the recent development of the computer, providing many fine results in various fields including the high voltage technique. As the major numerical electric field calculation methods, there are a charge simulation method, a finite difference method and a finite element method [1-2-3]. Each method has its own advantages and disadvantages [4-5]. For efficient calculation, the desirable method should be used according to an application field. Combining several calculation methods allows their advantages to be used and their disadvantages to be removed. This combination method can be applied to more extensive fields and will contribute to efficient calculation in many points such as accuracy and calculation time [6-7].

In order to obtain such calculation method, the author has developed the so-called combination method where the charge simulation method and the finite element method are combined. This paper describes its principle and major features, and shows that the calculation results are accurately obtained through several examples. The combination method enables the calculation of an electric field which could not be solved with enough accuracy by individual calculation method [8-9]. For example, the combination method can be applied in non-enclosed field with multi-dielectrics, a space charge field, and a field with leakage current and so on. In addition, replacing the part of a field with another calculation method, the author can reduce the core memory requirement of computer and improve the calculation accuracy. In the following chapter, the combination method, and its calculation examples are described.

II. CHARGE SIMULATION METHOD AND FINITE ELEMENT METHOD

Making use of mathematical linearly, in the charge simulation method, Laplace equation is expressed as a superposition of particular solutions such as point charges and ring charges [10]. Giving a boundary conditions, and using a concept of a potential coefficient, the author get equation 1.

$$P \times Q = \emptyset \qquad (1)$$

In equation 1, P is a potential coefficient matrix determined by coordinates of contour point and charge point. Q is a charge vector. Ø is a potential vector of contour points. In general, the number of this simultaneous linear equation is limited several 100's, because of computer capacity. P is in general an asymmetrical matrix without a zero component. The finite element method, which allows to divide the entire field into finite elements and to assume a potential approximation function valid in each element, gives the potentials $\emptyset_i$ of the node points of each element so that the electrostatic energy of the entire field may become minimum [11]. If the dielectric constant of a field is ε, the electrostatic energy function F is given by equation 2. From the minimum condition boundary is given by equation 3. The author can get finally the equation 4 as a simultaneous linear equations.

$$F = \int_V \frac{1}{2}\varepsilon(grad\emptyset)^2 \, dv \qquad (2)$$

$$\frac{\partial F}{\partial \emptyset_i} = 0 \qquad (3)$$

$$T \times \emptyset = B \qquad (4)$$

NİHAT PAMUK, is with Department of Electric Electronic Engineering, University of Zonguldak Bulent Ecevit University, Zonguldak, Turkey, (e-mail: nihatpamuk@beun.edu.tr / nihatpamuk@gmail.com).

https://orcid.org/0000-0001-8980-6913

In equation 4, T is a total matrix of element matrices. Ø is an unknown node potential vector. B is a constant vector. It is known that the T matrix is a band sparse and symmetric matrix. In the finite element method, the order of T matrix can reach several 1000's in order to solve the entire field, however, its band width is about 5 to 15, in general [12-13]. Although the charge simulation method and the finite element method are based on different principles, the similar systems of equations 1 and 4 are obtained. As shown in Table 1, both

the field calculations methods have complementary features each other [14]. The development of a new field calculation method, the combination of both the above methods, allows their features to be used and the new method will be applied to an extensive technical field. On the basis of this background, the combination method has been developed. If the author once form the coupling surface between charge simulation method and finite element method regions, the author can use this surface every time when the author calculate.

TABLE I
FIELD CALCULATION BY CHARGE SIMULATION METHOD AND FINITE ELEMENT METHOD

Features	Charge Simulation (CS) Method	Finite Element (FE) Method
Partial Field	The potential of a charge goes to zero at the infinite-point. This enables an open space (not enclosed) and a partial field to be calculated.	In general, this method is not appropriate for the calculation of a partial field.
Boundary Shape	Superposing the equipotential line by charges, essentially, this method is appropriate for a curved form rather than a straight line form.	This method, which uses a straight line form so long as making use of no isoparametric elements, is not appropriate for a curved shape.
Calculation Accuracy	Calculation accuracy is very high. Errors on the electrodes other than the contour points can become large.	An error occurs due to approximation by finite elements of the entire field. The error is a function of the number of elements.
Multi-Dielectric Field	As a rule, this method may be applied to the field with up to two dielectrics. The method is not appropriate for the field with more than two dielectrics.	This method is not limited by the number of dielectrics and is appropriate for a multi-dielectrics field.
Thin Electrode Field	This method is not appropriate for a thin electrode.	Appropriate in a desirable manner.
Space Charge Field	A singular point is required to be removed by taking charge distribution into consideration. Not easy.	The solution may be easily obtained. Because of an energy problem.
Others	Some experience is required concerning charge positions, contour point positions, etc.	This method may be universalized without experience. However, an automatic data generation program is necessary for input.

III. NUMERICAL COMBINATION METHOD APPROACH

In the combination method, entire field is separated into a "Charge Simulation (CS) method" region and a "Finite Element (FE) method" region. Naturally, the equation 1 applies to the (CS) region, while the equation 4 applies to the (FE) region. On the coupling surface of both regions, the entire field is combined on condition of the continuity of potential and dielectric flux density. On the coupling surface, boundary conditions are given to both regions each other. If unknowns of the entire field are given as shown in Table 2.

TABLE II
UNKNOWN PARAMETERS

n_L	Number of charges in the (CS) region
n_G	Number of contour points given onto the coupling surface. (Number of charges given in the coupling surface)
n_G'	Number of potential nodes given onto the coupling surface
n_F	Number of nodes in the (FE) region

The author get the equation 5, since the coupling points given onto the coupling surface are common to both regions. Then, the total number N of unknowns is shown in equation 6.

$$n_G' = n_G \qquad (5)$$
$$N = n_L + n_F + (2.n_G) \qquad (6)$$

If all N unknowns are determined, the electric field concerning the (CS) region, may be calculated by n_L charges Q_L and n_G charges Q_G, while the electric field concerning the (FE) region may be calculated by n_F potentials ϕ_F and n_G potentials ϕ_G. On the other hand the given conditions are; n_L

from contour point conditions in the (CS) region, n_F from the equations of energy minimal conditions in the (FE) region, and (2 x n_G) from potential continuity and normal component continuity of dielectric flux density on the coupling points arrayed on the coupling surface. Then the number of given conditions is N and the equations may be solved. Fig. 1 shows the coupling surface, coupling points arranged on the coupling surface and coupling charges corresponding to each coupling point.
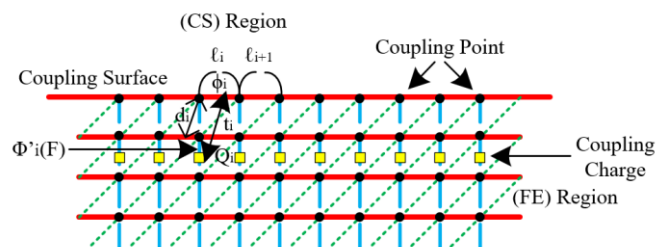

Fig.1. Coupling points and coupling charges

Let's consider the conditions which apply to coupling points. First, from the potential continuity, the author get the following equation 7. Using the potential coefficient P(i, j) and the unknown charge Q_j, $\phi_{i(CS)}$ may be expressed as follows equation 8.

$$\phi_{i(CS)} = \phi_{i(FE)} \qquad (i = 1 \sqcap n_G) \qquad (7)$$

$$\phi_{i(CS)} = \sum_{j=1}^{n_L + n_G} P(i,j).Q_J \qquad (i = 1 \sqcap n_G) \qquad (8)$$

$\phi_{i(FE)}$ is unknown itself. From the condition that the normal

components of dielectric flux density have continuity at the coupling points. The author get the equation 9. Further, the equation 10 is valid if the dielectric boundary is used as the coupling surface, while the equation 11 is valid if the inside of the same dielectrics is used as the coupling surface. $E_{ni(CS)}$ and $E_{ni(FE)}$ may be expressed as follows by equations 12 and 13.

$$D_{ni(CS)} = D_{ni(FE)} \qquad (i = 1 \square\ n_G) \qquad (9)$$

$$E_{ni(CS)} = \left[\frac{\varepsilon_{(FE)}}{\varepsilon_{(CS)}} \right] . \quad E_{ni(FE)} \qquad (10)$$

$$E_{ni(CS)} = E_{ni(FE)} \qquad (11)$$

$$E_{ni(CS)} = \sum_{j=1}^{n_L + n_G} F_n(i, j).Q_j \qquad (12)$$

$$E_{ni(FE)} = -\left(\frac{\phi_{i(FE)} - \phi'_{i(FE)}}{d_i} \right) \qquad (13)$$

In the equations 9 through 13, n indicates a normal direction, while $F_{n\ (i,j)}$ in the equation 12 is the field coefficient of the direction n. d_i is the distance to a potential difference approximation point in the i-th coupling point, which is shown in Fig. 1. In Fig.1, the distance t from a coupling point to a coupling charge is generally expressed as a function of the distance ℓ between coupling points. Thus, the author get the equation 14. In equation 14, k is a constant.

$$t_i = k.\ell_i \qquad (14)$$

Fig. 2 shows the combination matrix constructed in such manner and the configuration of simultaneous linear equations. In the matrix of Fig. 2, the portions indicated by oblique lines are asymmetrical matrices without zero component. The entire combination matrix is asymmetric and a bad-status matrix with many zero elements.
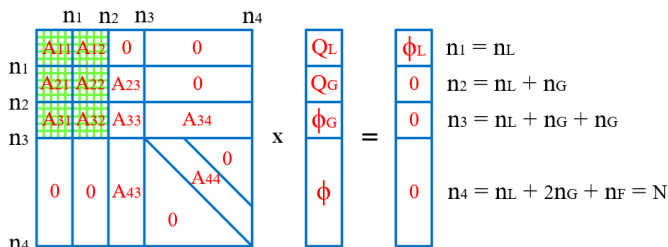
Fig.2. Combination matrix and configuration of simultaneous linear equations

IV. DISCUSSION

The combination method is applied to the two dimensional two-dielectric field where a cylinder and a grounded plane are used as electrodes as shown in Fig. 3 and calculation results are examined. The cylinder potential is to be 100% and the plane potential is to be 0% [15]. First, the dielectric field boundary is considered to be a coupling surface for both the calculation method regions and the dielectric field constant ratio is to be 1.0 - 3.0 [16]. Nine (n_L) infinite line charges were

arranged in the high voltage power transformer apparatus cylinder electrode and calculation was made by setting the coupling point conditions as a parameter. A program is available so that, in each element in the (FE) region, first and second polynomials may be used as a potential approximation function. To make the element in (FE) region, an automatically grid generation program was introduced.
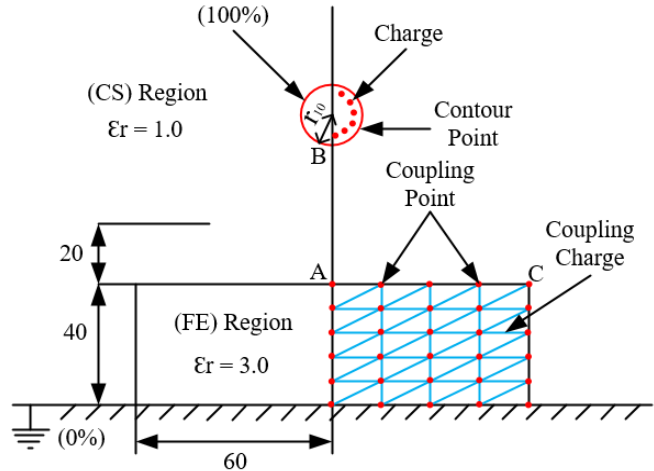
Fig.3. Calculation example of 2D-dimensional and 2D-dielectric field

Table 3 shows calculation results of the potential and electric field strength of the point A and electric field strength of the point B in high voltage power transformer apparatus. Calculation results using charge simulation method by 330 charges on the same electrode configuration are shown in this table for comparison. Calculation results of the potential and electric field strength of the point A (in Fig. 3) and of the electric field strength of the point B when k in the equation 14 is equal to 1 and ℓ_i/ℓ_{i+1} is equal to 1.0 in Fig. 1.

TABLE III
CALCULATION RESULTS USING CHARGE SIMULATION METHOD

n_G	Potential at point A	Electric field strength at point A	Electric field strength at point B
8	29.60264 (pu)	2.57639 (pu)	5.89505 (pu)
12	28.60814 (pu)	2.62808 (pu)	5.98226 (pu)
16	28.19811 (pu)	2.65422 (pu)	5.95752 (pu)
20	27.97338 (pu)	2.66892 (pu)	5.99580 (pu)
24	27.83155 (pu)	2.67823 (pu)	6.00434 (pu)
28	27.73378 (pu)	2.68464 (pu)	6.01023 (pu)
32	27.66252 (pu)	2.68931 (pu)	6.01452 (pu)
36	27.60785 (pu)	2.69288 (pu)	6.01782 (pu)
40	27.56525 (pu)	2.69566 (pu)	6.02038 (pu)
44	27.53046 (pu)	2.69793 (pu)	6.02249 (pu)
48	27.50130 (pu)	2.69981 (pu)	6.02426 (pu)
52	27.47723 (pu)	2.70137 (pu)	6.02572 (pu)
56	27.45629 (pu)	2.70272 (pu)	6.02700 (pu)
60	27.43821 (pu)	2.70388 (pu)	6.02810 (pu)
64	27.42243 (pu)	2.70489 (pu)	6.02906 (pu)
By (CS) method 330 charges	27.23134 (pu)	2.71510 (pu)	6.04001 (pu)

Error of potential at point A is shown in Fig. 4. Error of field strength at point A is shown in Fig. 5. Figs. 4 and 5 show calculation errors indicated as a function of the number n_G of

coupling points. As the number of coupling points increase, calculation errors decrease.
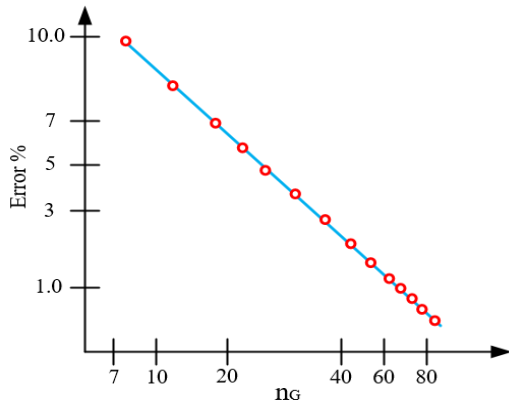

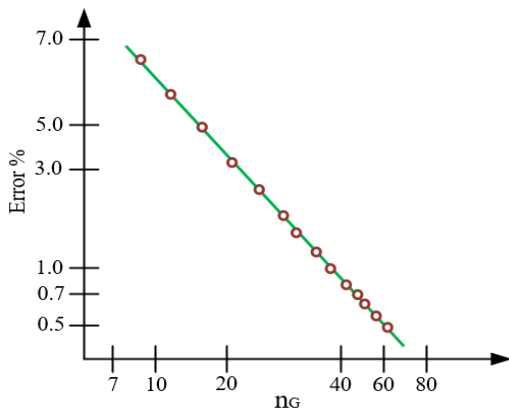Fig.4. Error of potential at point A

Fig.5. Error of field strength at point A

Fig. 6 shows that the electric field strength at the point A is indicated as a function of the number of elements in the finite element method region. The calculation results by using first and second order polynomials in (FE) region is shown for comparison.
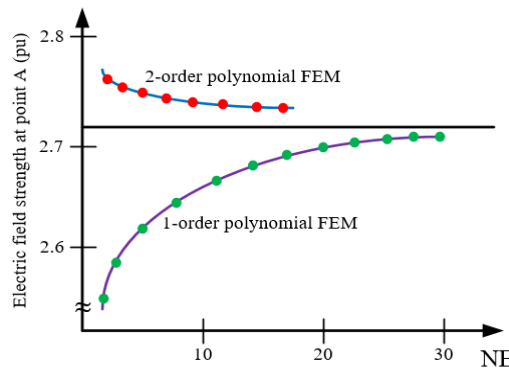

Fig.6. Field strength as function of (NE)

Fig. 7 shows the electric field strength of the point A as a function of k in equation 14, where n_G is kept constant. If n_G is to be 64 and the coupling points are distributed in geometrical progression, it is revealed that calculation errors are not more than 0.2% for the potential and 0.1% for the electric field strength at the point A. The above calculation results reveal that calculation accuracy is a function of the number n_G of

coupling points and if the author apply this method to high voltage technique, the author can get satisfactory calculation results. The point C in Fig. 3 is a singular point and it is assumed that calculation errors increase in the vicinity of the point C.
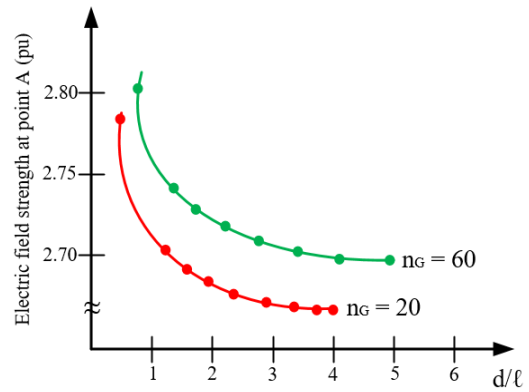
Fig.7. Field strength as function of (d/ℓ)

Fig. 8 shows an example of equipotential lines of 2D dimensional electric field. The solid lines are obtained by using the coupling surface X, while the dotted lines are obtained by using the dielectric boundary as the coupling surface. The dotted lines show discontinuity at the equipotential line at point P.
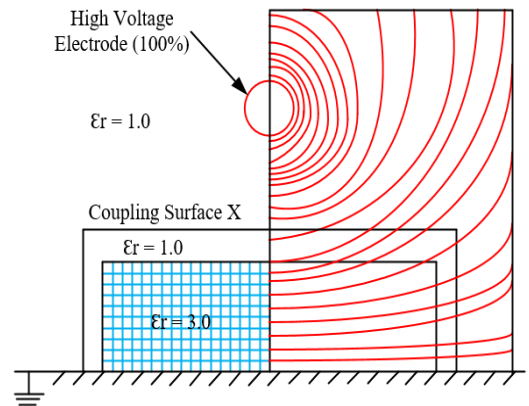
Fig.8. Equipotential lines of 2D dimensional electric field

Fig. 9 shows a mesh in (FE) region. Fig. 10 shows a dielectric two flat plate field.
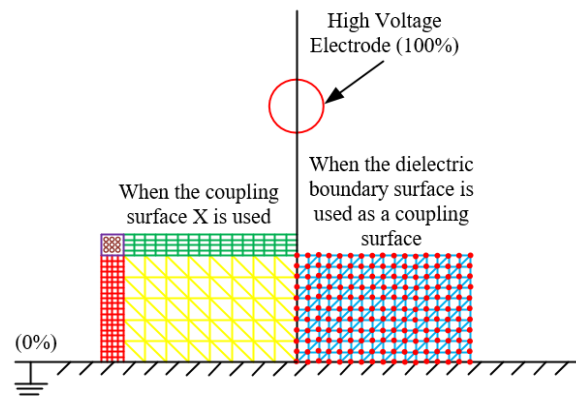
Fig.9. Mesh of elements in FE method
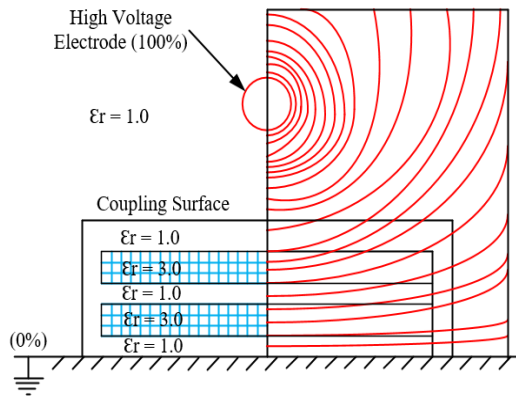
Fig.10. Calculation example dielectric flat-plate field

It is obviously shown that once formed the coupling surface between (CS) and (FE) region may be applied to various kinds of fields. Even if there are space charges or surface charges, namely the Poisson field, the combination method can be easily applied. As shown in Fig. 11, the equipotential lines are evidently distorted if space charges are distributed in the thin space on the dielectric plate.
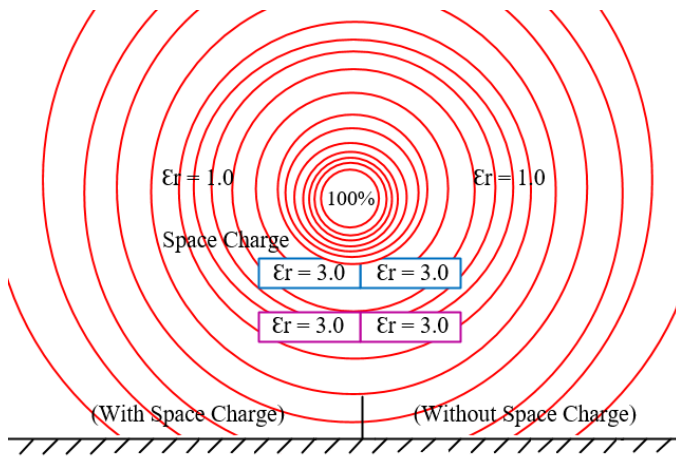

Fig.11. Calculation example of space charge field

In that case, F' is used as an energy functional that is valid in the (FE) region. F' may be expressed as follows by equation 15. In equation 15, ρ is the charge gratuity. The combination method may be also applied to a field with surface or volume leakage current.

$$F' = \iiint \left(\frac{1}{2} \varepsilon.(grad\phi)^2 - \rho\phi \right) dv \qquad (15)$$

Finally, Fig. 12 shows calculation results of equipotential lines when the combination method is applied to an axisymmetric three (3D) dimensional electric field. The principles of the coupling surface are the same as those in the two (2D) dimensional electric field. Ring charges are used in the (CS) region. The calculation of three (3D) dimensional axisymmetric multi dielectric field in the high voltage power transformer apparatus as shown in Fig. 12. The Fig. 12 consists of four dielectric fields of air, glass, insulating oil and oil-impregnated paper and is non-enclosed field in the high voltage power transformer. Therefore, it is difficult to solve

the electric field by the optimization theory based on charge simulation method or the finite element method, if they are used individually.
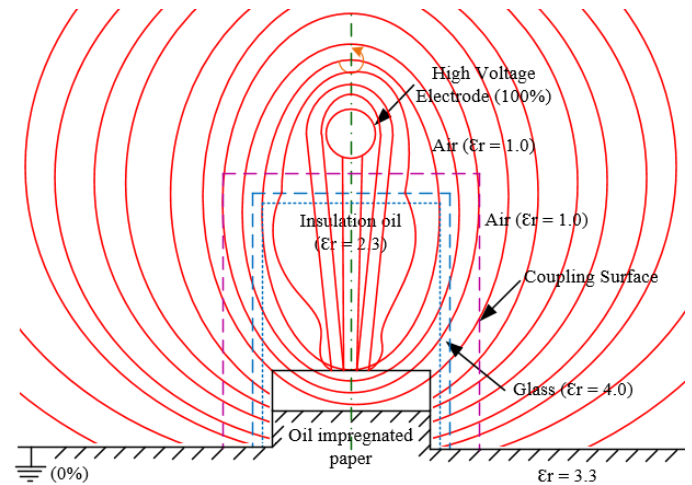
Fig.12. Calculation of 3D dimensional axisymmetric multi dielectric field

V. CONCLUSION

As described above, the so-called combination method that combines the optimization theory based on charge simulation method and the finite element method has the following features. Calculation accuracy required to the high voltage power transformer apparatuses is fully met. Calculation accuracy depends on the relationship of the number of coupling points placed on the coupling surface between the (CS) and (FE) region. Using a high order polynomials allows high accuracy to be obtained in less coupling points. The coupling surface is proper to not only a dielectric boundary but also any other space. If a dielectric boundary is complicated, it is recommended for easier calculation that any other space should be used as the coupling surface. This method may be applied to non-enclosed field, a complicated dielectric field, a space-charge field, etc. If the coupling surface is once formed, the combination method can be applied easily to any other field to be calculated.

REFERENCES

[1] M.M. Abouelsaad, M.A. Abouelatta, A.E.R. Salama. "Genetic algorithm-optimized charge simulation method for electric field modelling of plate-type electrostatic separators." IET Science, Measurement & Technology, vol. 7. 1, 2013, pp 16-22.

[2] K. Nishimura, K. Nishimori. "Arrangement of fictitious charges and contour points in charge simulation method for electrodes with 3D asymmetrical structure by immune algorithm." Journal of Electrostatics, vol. 63. 6-10, 2005, pp 743-748.

[3] N.H. Malik. "A review of the charge simulation method and its applications." IEEE Transactions on Electrical Insulation, vol. 24. 1, 1989, pp 3-20.

[4] X. Liu, Y. Cao, E. Wang. "Numerical simulation of electric field with open boundary using intelligent optimum charge simulation method." IEEE Transactions on Magnetics, vol. 42. 4, 2006, pp 1159-1162.

[5] A. Ranković, M.S. Savić. "Generalized charge simulation method for the calculation of the electric field in high voltage substations." Electrical Engineering, vol. 92. 2, 2010, pp 69-77.

[6] W. Krajewski. "Numerical modelling of the electric field in HV substations." IEE Proceedings-Science, Measurement and Technology, vol. 151. 4, 2004, pp 267-272.

[7]   S. Nikolovski, P. Maric, Z. Baus. "Electromagnetic field calculation of transformer station 400/110Kv Ernestinovo using the CDEGS software." Journal of Electrical Engineering-Bratislava, vol. 58. 4, 2007, pp 207-213.

[8]   T. Lu, H. Feng, Z. Zhao, X. Cui. "Analysis of the electric field and ion current density under ultra-high-voltage direct current transmission lines based on finite element method." IEEE Transactions on Magnetics, vol. 43. 4, 2007, pp 1221-1224.

[9]   D. Stefanini, J.M. Seifert, M. Clemens, D. Weida, "Three Dimensional FEM Electrical Field Calculations for EHV Composite Insulator Strings." IEEE International Power Modulator and High Voltage Conference, 23-27 May 2010. Atlanta, GA, USA, 2010.

[10] C. Lu, Z. Yang, J. Bai, Y. Cao, X. He. "Three dimensional immersed finite element method for anisotropic magnetostatic/electrostatic interface problems with nonhomogeneous flux jump." International Journal for Numerical Methods in Engineering, vol. 121. 10, 2020, pp 2107-2127.

[11] L.J. Gomez, M. Dannhauer, L.M. Koponen, A.V. Peterchev. "Conditions for numerically accurate TMS electric field simulation." Brain Stimulation, vol. 13. 1, 2020, pp 157-166.

[12] A.T. Htet, G.B. Saturnino, E.H. Burnham, G.M. Noetscher, A. Nummenmaa, S.N. Makarov. "Comparative performance of the finite element method and the boundary element fast multipole method for problems mimicking transcranial magnetic stimulation (TMS)." Journal of Neural Engineering, vol. 16. 2, 2019, 024001.

[13] Q. Tan, Q. Xu, L. Chen, Y. Huang. "A new method to improve internal electric field distributions of pockels OVS." IEEE Sensors Journal, vol. 17. 3, 2017, pp 4115-4121.

[14] K.H. Lee, S.G. Hong, M.K. Baek, H.S. Choi, Y.S. Kim, I.H. Park. "Alleviation of electric field intensity in high voltage system by topology and shape optimization of dielectric material using continuum design sensitivity and level set method." IEEE Transactions on Magnetics, vol. 51. 3, 2015, pp 1-4.

[15] Y.N. Zhao, G.Q. Zhang, Z.Z. Guo, S. Cheng. "The mathematical model of electrical field distribution in optical voltage transformer." Procedia Engineering, vol. 29. 1, 2012, pp 2661-2666.

[16] S.L. Ho, N. Chen, W.N. Fu. "A moving mesh embedded algorithm in finite element method for optimal design of electromagnetic devices." IEEE Transactions on Magnetics, vol. 47. 10, 2011, pp 2947-2950.

BIOGRAPHY

NİHAT PAMUK is an Associate Professor, of Department of Electrical Electronics Engineering in Zonguldak Bulent Ecevit University. He received his bachelor's degree in electric electronics engineering department from Fırat University, Turkey, in 2005. He completed his MSc and PhD degrees all in electric electronics engineering department from Sakarya University, Turkey in 2009 and 2012 respectively. His research interests are power system analysis, power protection systems, high voltage transmission and switch gears devices, renewable energy, smart grids and power quality.

Design and Implementation of a Test Device for Determining the Capacity of Industrial Battery Banks

Z. ZÜREY, K. SABANCI, and S. BALCI

Abstract—**In this study, a test device is developed to measure the capacities and performances of high capacity battery banks and to detect broken cells. Batteries lose their performance over time due to their chemical properties, storage and usage conditions, production technologies. Some batteries may even become completely unusable long before the promised life cycle. Through this test device, the instant capacity of the battery banks is measured. Based on the data obtained, quantitative data such as state of health and nominal energy of the battery bank are calculating. It is determined whether the battery bank will meet the need according to its intended use. In this way, it is ensured to prevent possible losses by determining the battery cells or groups that need to be changed.**

Index Terms— **Battery capacity test device, industrial battery banks, buck converter, power electronics.**

I. INTRODUCTION

WITH THE developing technology, usage of the batteries is becoming widespread day by day. As storage elements, batteries are frequently used in electric vehicles (EVs), uninterrupted power supply (UPS) and renewable energy sources [1]. In addition, while the efforts to reduce the production costs of the batteries have been going on in recent years, their performance has been increasing gradually.

The world's energy needs were mostly met with fossil fuels. During this period, very important researches has been done on renewable energy sources, which do not have a negative impact

ZEKİ ZÜREY, is with Department of Electrical and Electronics Engineering University of Karamanoğlu Mehmetbey University, Karaman, Turkey, (e-mail: zurey.z@gmail.com).

https://orcid.org/0000-0003-4219-1274

KADİR SABANCI, is with Department of Electrical and Electronics Engineering University of Karamanoğlu Mehmetbey University, Karaman, Turkey, (e-mail: kadirsabanci@kmu.edu.tr).

https://orcid.org/0000-0003-0238-9606

SELAMİ BALCI, is with Department of Electrical and Electronics Engineering University of Karamanoğlu Mehmetbey University, Karaman, Turkey, (e-mail: sbalci@kmu.edu.tr).

https://orcid.org/0000-0002-3922-4824

on natural life [2]. Energy generation systems using renewable energy sources are generally used in mountainous areas where electricity transmission is difficult and expensive, on islands with their own electricity network, to meet the electrical energy needs of settlements [3]. As a result, battery banks are preferred for the purpose of temporarily storing electricity.

The most preferred application areas for energy storage systems installed with batteries are used in UPS systems for emergency and communication systems. The widespread use of energy sources such as photovoltaic and wind, the need for energy storage systems is increasing [2].

Another application area of the battery banks is UPS systems. It is inevitable to use UPS in critical systems. In critical applications, high capacity battery banks are used as backup energy sources to protect the system against power failure [4]. While using generator systems fed fossil fuel previously, the use of UPS systems with large battery banks has become widespread in parallel with the development of battery technology.

However, battery cells lose their health due to use. It may cause life-threatening and financial losses in case of failure or malfunction of the system it supplies energy. Disruption of the cell connected in series can cause imbalances in the parallel connection. Periodic tests are carried out to prevent such malfunctions. In these tests, cell voltages are checked one by one to detect broken cells [5].

One of the most common uses of battery banks is electric vehicles. The use of electric vehicles is increasing with great momentum. Although the search for alternatives continues, battery banks are used in today's electric vehicles for energy storage. It is not suitable for the range of vehicles to continue to be used in the electric vehicles of the battery banks on the electric vehicles, whose capacity has decreased below 70%.

However, these battery banks are still very valuable and can be used in many areas. As a matter of fact, energy storage facilities can be established on the basis of grids with used battery banks removed from electric vehicles.

Testing and monitoring the health of the battery banks is very important in terms of cost and work safety. With the test device developed, important data about the health of battery banks were obtained.

Schollet.al. (1971) got the first automatic battery tester

patent. This device has fixed load groups. Any of these load groups can be selected manually. In addition, instantaneous voltage and instantaneous current can be recorded by a mechanical recorder [6]. Berglund et. al. (1997) with the device they developed, aimed to test the low voltage batteries by discharging and charging them at 2400W rated power. There are two options for discharge. While the first option can be discharged for a long time with a low load, the second option can be discharged for a short time with a high load [7]. Bertnesset.al. (2000) tried a different method in the battery test. The device developed in this study determines a battery characteristic according to the values obtained in its tests and generates code according to this characteristic. According to this code produced, comments about battery health are made [8]. Brink et.al. (2000) studied a different battery characterization method. With the device they developed, they measured the terminal impedance of the battery under a few fixed loads. They tried to estimate the battery capacity by interpreting the data they obtained [9]. Anbuky et.al. (2005) developed a battery characterization method based on computation. In this method, the amount of voltage drop is taken into account when the battery is connected to a fixed load. This value is interpreted as a result of mathematical operations and information about battery capacity is obtained [10]. Coleman et.al. (2008) developed the dual pulse method to determine the AHC, SoC and SoH values of a battery. The first pulse balances the battery over its previous history. The second pulse determines the battery parameters. The new approach has been experimentally validated [11].

In previous studies, one of the fixed load options was preferred and the batteries were discharged. In some studies, short term tests were conducted. The results obtained were evaluated and estimations about battery capacity were made.

The datasheets of commercial companies are used when choosing a storage element with the desired technical specifications for storage unit installation for a system or device. After the storage unit is installed, the batteries are expected to meet certain criteria throughout the life of the system. However, due to their chemical structure, the batteries lose their health depending on the usage and duration of use. In this context, the health and performance of the batteries used in the industrial field should be at a minimum level for reasons such as both commercial and safety requirements. If the battery used is unable to meet the system requirements, it may lead to some malfunctions, system failure or even dangerous situations over time.

In this study, a fully automatic test device has been developed to measure the capacities and performances of the high capacity battery banks and to detect broken cells. With this test device, long term full tests were performed instead of the estimation and calculation methods and real results were obtained. In this way, problems arising from the chemical structures of the batteries and ignored in the calculations can be identified. In addition, thanks to the automated device, the test conditions were clearly determined. It can be shown as an example of the usage areas of the developed tester, electric cars, electric buses, electric motorcycles and bicycles, all

electric construction machines such as forklifts, mini loaders and excavators, battery banks used for UPS purposes, battery banks of small-scale solar power plants, battery banks used in micro grid applications.

II.   THEORETICAL EXPLANATION OF THE BUCK CONVERTER CIRCUIT

The Buck converter is a non-isolated DC to DC converter that reduces the output voltage below the input voltage. Non isolated DC to DC converters have a disadvantage that, although simple and widely used, the voltage conversion rates are limited. So, when high conversion rate is required, isolated DC to DC converters are used. The buck converters are simple. It requires only one switching component. Therefore, their efficiency is high and their costs are low. High efficiency can be achieved by the use of switching elements which consume less power and are controlled at higher frequencies. Parallel to the developments in electronics, BJT, MOSFET and IGBT are used as switching elements in dc-dc converters in recent years. However, IGBT and MOSFETs are preferred in high-power converter applications [12, 13]. Fig. 1 shows the basic diagram of the buck converter.
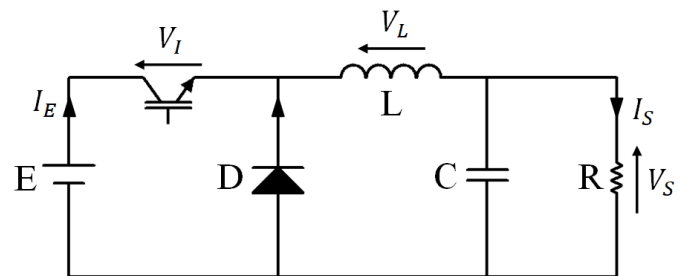

Figure. 1. Buck converter circuit

The input impedance of a DC to DC converter is the impedance seen at the input source. The output impedance is the output voltage response of the converter for the excitation of the current when the duty rate and the input voltage are constant [14]. R resistance represents load. L and C form a filter to limit oscillations on voltage and output current. Ideally, I_S and V_S are continuous [15]. When L is closed, the voltage drop on the inductor is:

$$V_L = E - V_S \qquad (1)$$

The current through the inductor increases linearly. As the diode is reverse-biased, no current flows over it. Typical waveforms of current and voltage in a converter are shown in Fig. 2 [15].

When the switch T is opened, the diode is forward biased. The voltage across the inductor is $V_L = -V_s$. The current I_L decrease. The energy stored in inductor form:

$$E_L = \frac{1}{2} L I_L^2 \qquad (2)$$

The rate of change of I_L can be calculated from:

$$V_L = L \frac{dI_L}{dt} \qquad (3)$$

with V_L equal to $E-V_s$ during the on-state and to $-V_S$ during the off-state. Therefore, the increase in current during the on-state is given by:

$$\Delta I_{L_{on}} = \int_0^{Ton} \frac{V_L}{L} \, dt = \frac{E-V_S}{L} t_{on=\alpha T} \quad (4)$$

where α is called the duty cycle with a value between 0 and 1. The decrease in current during the off-state is given by:

$$\Delta I_{L_{off}} = \int_{t_{on}}^T \frac{V_L}{L} \, dt = -\frac{V_S}{L} t_{off=(1-\alpha)T} \quad (5)$$

$$\Delta I_{L_{on}} + \Delta I_{L_{off}} = 0 \quad (6)$$

$$\frac{V_S}{E} = \alpha \quad (7)$$
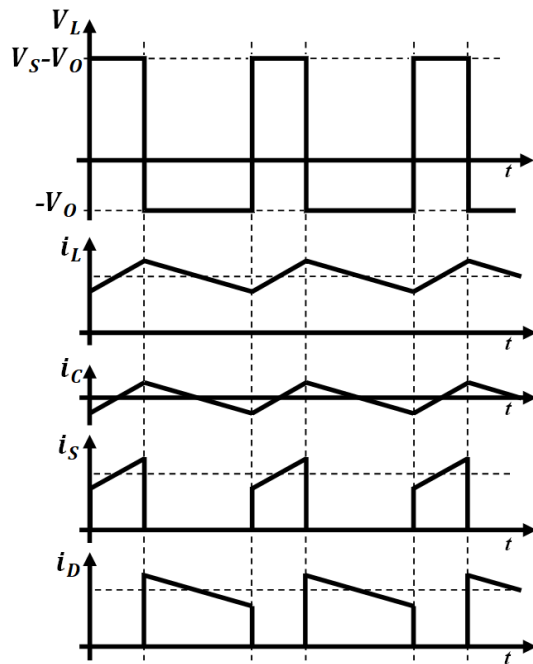
Figure. 2.   The basic waveforms of the buck converter circuit

III.   THE BASIC CIRCUIT STRUCTURE OF THE DESIGNED SYSTEM

In the buck converter circuit, the main purpose is to provide a constant level of voltage to the load by trimming the voltage with a controlled switching element. An LC filter and a diode parallel to this filter are used to damp oscillations caused by voltage clipping.

In the designed test device, it is aimed to load the battery bank with a constant current using a resistance group and a controlled switching element.

Although wire wound resistances are of small size, lightweight and very high power, they are not suitable for use in an environment where a battery bank is available since they reach very high temperatures. For this, 4 resistances of 1.5kW and 0.75Ω with aluminum heat sink are connected in parallel. Active cooling of the resistance group is provided by using a fan. In this way, the resulting temperature was kept below 50°C.

SQD300AA100 Darlington power transistor module is used as a switching element [16]. With this module of 1000V and 300A, switching is performed at a variable duty rate at a frequency of 1 kHz.

A diode module is connected in series to the circuit in order to prevent problems that may arise in case of incorrect connection of the battery bank. The circuit structure of the designed system is shown in Fig. 3.
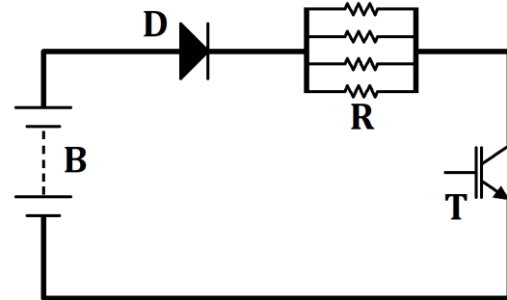

Figure. 3.   The basic circuit structure of the designed system

The block diagram of the operation of the developed tester is given in Fig. 4. A special control card is designed in the Altium Designer program for manage the system. This board is managed by the PIC18F46K22 microcontroller manufactured by Microchip. It is an 8-bit microcontroller that operates at a frequency of 64MHz. It has 10 bit analog to digital converter and 10 bit PWM resolution [17-19]. On the board, there is a driving circuit for the transistor module, 2 serial ports, analog and digital inputs and outputs, 4 relay outputs and real time clock.

A sensor is used to measure the voltage and current. A digital temperature sensor was used to monitor the temperature of the resistance group.

With the test device developed, it was aimed to test all battery banks consisting of different battery types. While some batteries are not expected to heat up during discharge, some batteries can be heated up immediately depending on their health and chemical structure. A temperature sensor has been used to prevent negativity in case of warming the battery bank.

An HMI LCD was used to enter parameters before starting the test and to display parameters such as voltage, current, temperature and time during the test. This LCD is the NX8048K070-011C model manufactured by Nextion. It is 7.0" and capacitive touch. Interface is created in Nextion Editor Program [20-22]. In addition, during the test, all parameters are recorded on a micro SD card so that they can be recorded and evaluated later.

IV.   PARAMETERS RELATED TO BATTERY TEST

The load test is performed to test that the battery bank can supply enough power and energy when needed. The load is designed to represent the expected conditions under which battery banks can be used [23]. The parameters used to determine the health of a battery are described below.

State of Charge (SOC): Indicates the instantaneous capacity of the battery. In this way, the user can calculate how long the battery will supply the system with energy [24].
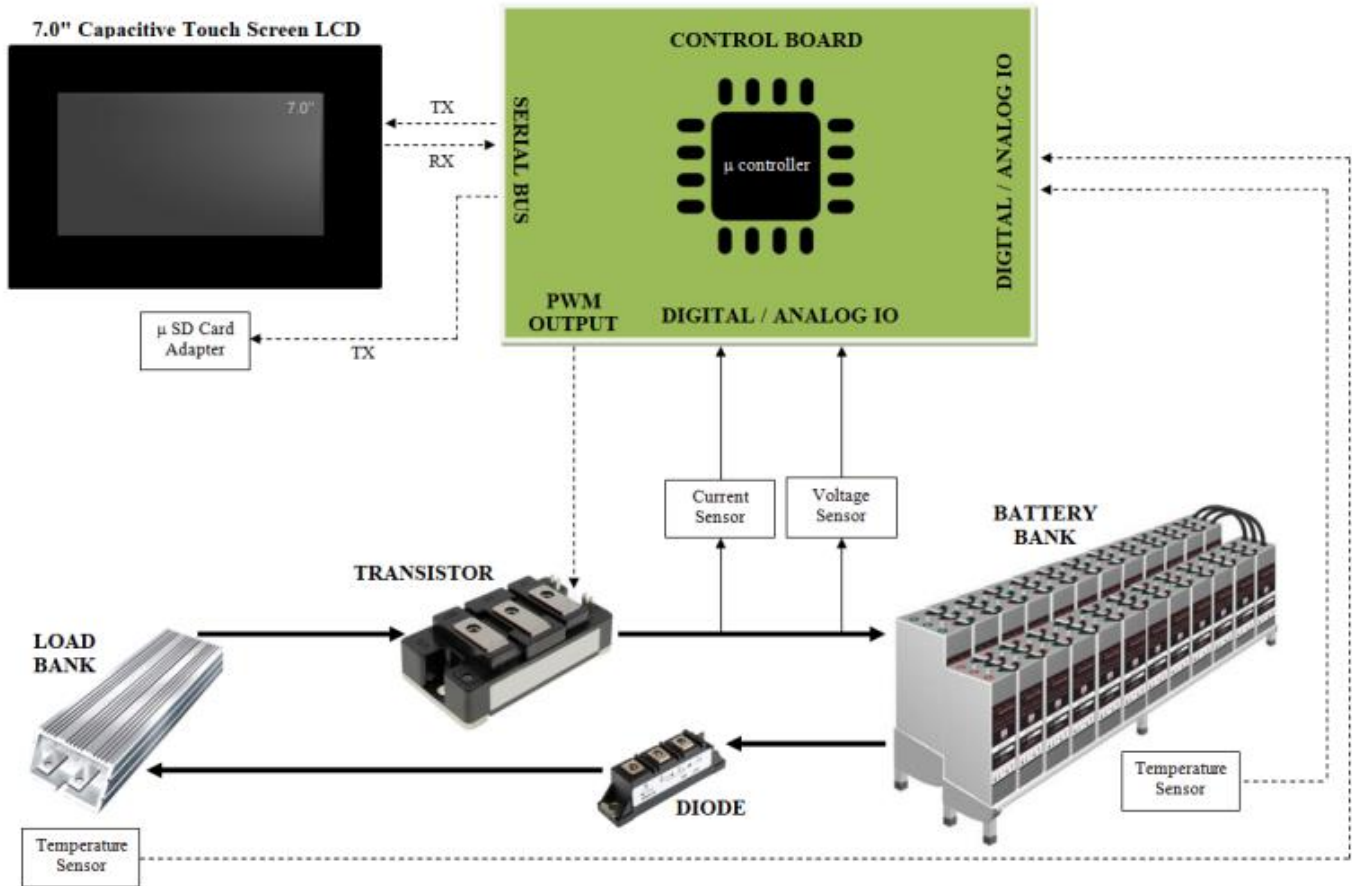
Figure. 4.   The block diagram of the operation of the test device

State of health (SOH): Defines the comparison of battery performance with its new form. It is not an absolute measurement [25].

Capacity or Nominal Capacity (Ah): Defines the energy drawn from the battery when it is discharged from full charge voltage to cut off voltage. It is calculated by multiplying the discharge current by the discharge time [26].

Energy or Nominal Energy (Wh): Defines the energy drawn from the battery when it is discharged from full charge voltage to cut off voltage. It is calculated by multiplying the discharge power by the discharge time [26].

Cycle Life: Indicates the maximum number of charge discharges of the battery, provided that it meets certain performance criteria [26].

V.   EXPERIMENTAL RESULTS AND DISCUSSIONS

Industrial banks, which have a cell voltage of 2V, were connected in series and battery banks were created. Many tests have been carried out with these battery banks. The data obtained from the tests are presented in Table 1.

As it is known, in load tests on batteries with lead acid chemistry, the amount of energy drawn and the voltage drop are directly proportional.

In tests 7 and 8, two battery banks with 118V charging voltage and 300Ah energy capacity were discharged at constant 20A. The voltage of both battery banks was reduced to 104V. As a result of the test process, 190Ah energy was drawn from the battery bank used in test number 7, while 180Ah energy was drawn from the battery bank used in test number 8. In this case, it is obvious that the battery bank used in the test number 8 is healthier.

Similarly, in tests 11 and 12, two battery banks with 112V charge voltage and 200Ah energy capacity were discharged at a constant 10A. The voltage of both battery banks has been reduced to 102V. As a result of the test process, 95Ah energy was drawn from the battery bank used in test number 11, while 70Ah energy was drawn from the battery bank used in test number 12. If a comparison is made, it can easily be said that the battery bank used in test number 12 is healthier. The voltage-time graph for tests 23 and 25 is presented in Fig. 5.

When a healthy battery is loaded with constant current, the voltage drop is expected to be very close to the line. In the graphic in the figure, a straight line is observed between 48V-45V as expected. However, a steeper and partially exponential curve is observed before 48V. This can be explained by the decrease in the life of both battery banks.

TABLE I.   Measurement data obtained with experimental test

Test No	Battery Bank Busbar Voltage (V)	Battery Bank Capacity (Ah)	Test Current (A)	Test Time (min)	Busbar Voltage at the End of the Test (V)	Drawn Energy (Ah)
1	120	200	10	720	104	120
2	120	200	10	700	104	116.6
3	120	200	10	615	106	102.5
4	120	200	10	600	106	100
5	120	200	10	600	108	100
6	118	200	10	600	103	100
7	118	300	20	570	104	190
8	118	300	20	540	104	180
9	118	200	10	600	104	100
10	118	200	10	540	107	90
11	112	200	10	570	102	95
12	112	200	10	420	102	70
13	112	200	8	630	105	84
14	112	200	10	450	105	75
15	112	200	8	570	106	76
16	112	200	8	600	106	80
17	110	200	10	500	102	83.3
18	110	200	10	420	102	70
19	110	200	10	360	102	60
20	110	100	10	300	104	50
21	50	200	10	620	42	103.3
22	50	200	10	560	42	93.3
23	50	200	10	600	45	100
24	50	200	10	540	45	90
25	50	200	10	420	45	70
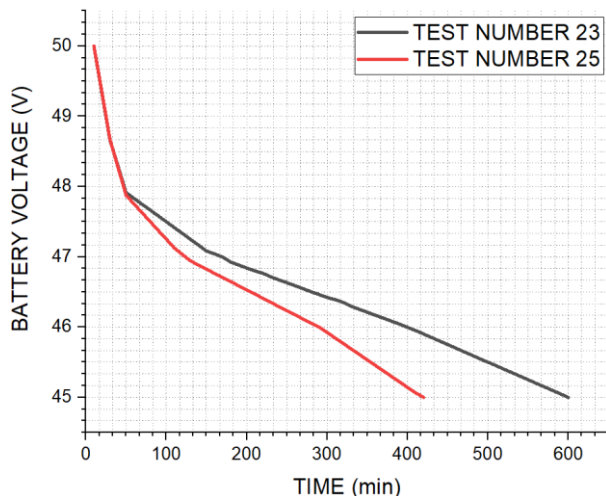
Figure. 5.   Voltage-time graph for tests 23 and 25

It can be seen that the battery bank used in the test number 25 reached a voltage of 45V 180 minutes ago. Battery banks have the same charge voltage, same capacity and are discharged at the same current. In this case, it can be said that the battery bank used in the test number 23 is healthier.

The oscilloscope view of the battery bank busbar voltage during the test is given in Fig. 6. At 115.75V battery voltage, a 21V fluctuation is observed from pick to pick during switching. This is an acceptable value and has no effect on the test result.

Figure. 6.   Battery voltage on test

When the tests given in the Table 1 are grouped and examined as a whole, it is observed that batteries with the same chemical structures and technical specifications give different results when subjected to the same tests. This clearly shows that batteries with the same characteristics perform differently over time. Through the developed tester, these changes in battery performances can be detected. If these tests are not carried out, it is quite difficult to detect batteries that are damaged or have lost performance.

VI.   CONCLUSION

In this study, the battery banks were discharged with a constant current in the tests performed with the developed test device. Instant parameters are reported during the test. Based on these data, technical parameters of battery banks were obtained.

Numerous experimental tests have been carried out with the battery banks created by connecting industrial type aqueous batteries with a cell voltage of 2V in series. The data obtained from the tests are presented in Table 1. Considering tests 21 and 22, both battery banks were discharged to the cut-off voltage. The SOH value of the battery bank number 21 can be calculated as 51.5% and the SOH value of the battery bank number 22 can be calculated as 46.5%. As expected, a straight curve is observed between 48V-45V on the voltage-time graph obtained for the tests 23 and 25 in this table. However, the formation of a steeper and partially exponential curve before 48V can be explained by the decrease in the life of both battery banks.

When these tests are not carried out, it is quite difficult to detect batteries that are connected to a system, that are damaged or have lost performance. It can result in data loss and financial losses in a UPS system, financial losses and serious injuries in systems connected to power transmission lines.

Many studies have been conducted that can test a single cell, specific to different battery structures. However, in large scale battery banks, it takes a lot of time to test each cell individually. The developed tester provides a great advantage thanks to its ability to test at high current and high voltage as well as to be adjusted for different battery structures and automatic operation.

The next step of the future study is to measure and report each cell voltage individually. In this way, broken cells can be easily detected.

REFERENCES

[1] I. Sefa, S. Balci, N. Altin, and S. Ozdemir, *Comprehensive analysis of inductors for an interleaved buck converter*. 2012, pp. DS2b.5-1.
[2] T. Blank, J. Badeda, J. Kowal, and D. Sauer, *Deep discharge behavior of lead-acid batteries and modeling of stationary battery energy storage systems*. 2012.
[3] E. Oguz, H. Çimen, and Y. Oğuz, "Simulation and Power Flow Control Using Switching's Method of Isolated Wind-Solar Hybrid Power Generation System with Battery Storage," *Balkan Journal of Electrical and Computer Engineering,* pp. 40-49, 09/01 2017, doi: 10.17694/bajece.334348.
[4] N. Altin, S. Balci, S. Ozdemir, and I. Sefa, "A comparison of single and three phase DC/DC converter structures for battery charging," in *2013 International Conference on Renewable Energy Research and Applications (ICRERA)*, 20-23 Oct. 2013 2013, pp. 1228-1233, doi: 10.1109/ICRERA.2013.6749939.
[5] M. Kiel, D.-U. Sauer, P. Turpin, M. Naveed, and E. Favre, "Validation of single frequency Z measurement for standby battery state of health determination," *INTELEC 2008 - 2008 IEEE 30th International Telecommunications Energy Conference,* pp. 1-7, 2008.
[6] H. K. Scholl, "Automatic battery tester with recording means for battery performance," ed: Google Patents, 1971.
[7] N. C. Berglund, T. J. Rosedahl, and S. W. Steele, "Battery capacity test and electronic system utilizing same," ed: Google Patents, 1997.
[8] K. I. Bertness, "Method and apparatus for auditing a battery test," ed: Google Patents, 2000.
[9] G. D. Brink and D. L. Burton, "Battery capacity test method and apparatus," ed: Google Patents, 2000.
[10] A. H. Anbuky and P. E. Pascoe, "Battery capacity measurement," ed: Google Patents, 2005.
[11] M. Coleman, W. G. Hurley, and C. K. Lee, "An Improved Battery Characterization Method Using a Two-Pulse Load Test," *IEEE Transactions on Energy Conversion,* vol. 23, no. 2, pp. 708-713, 2008, doi: 10.1109/TEC.2007.914329.

[12] M. B. Bayram, I. Sefa, and S. Balci, "A static exciter with interleaved buck converter for synchronous generators," *International Journal of Hydrogen Energy,* vol. 42, no. 28, pp. 17760-17770, 2017/07/13/ 2017, doi: https://doi.org/10.1016/j.ijhydene.2017.03.062.
[13] S. Ozdemir, S. Balci, N. Altin, and I. Sefa, "Design and performance analysis of the three-level isolated DC-DC converter with the nanocyrstalline core transformer," *International Journal of Hydrogen Energy,* vol. 42, no. 28, pp. 17801-17812, 2017/07/13/ 2017, doi: https://doi.org/10.1016/j.ijhydene.2017.02.158.
[14] F. Asadi and K. Eguchi, "On the extraction of input and output impedance of PWM DC-DC converters," *Balkan Journal of Electrical and Computer Engineering,* vol. 7, 04/30 2019, doi: 10.17694/bajece.468787.
[15] R. Bououd and S. Lassaad, *An overview of chopper topologies*. 2017, pp. 1-7.
[16] SANREX. "SQD300AA100 Transistor Module." https://www.digchip.com/datasheets/download_datasheet.php?id=919058&part-number=SQD300AA100 (accessed 2019).
[17] Altium. "Altium Designer." https://www.altium.com/altium-designer/ (accessed 2020).
[18] Microchip. "Microchip." https://www.microchip.com/ (accessed 2020).
[19] Microchip. "PIC18F46K22 Microcontroller." https://www.microchip.com/wwwproducts/en/PIC18F46K22#additional-features (accessed 2020).
[20] Nextion. "Home - Nextion." https://nextion.tech/ (accessed 2020).
[21] Nextion. "NX8048k070 - Nextion." https://nextion.tech/datasheets/nx8048k070/ (accessed 2020).
[22] Nextion. "Nextion Editor." https://nextion.tech/nextion-editor/#section1 (accessed 2020).
[23] Electropaedia. "Battery Testing." https://www.mpoweruk.com/testing.htm (accessed 2019).
[24] Electropaedia. "State of Charge (SOC) Determination." https://www.mpoweruk.com/soc.htm (accessed 2019).
[25] Electropaedia. "State of Health (SOH) Determination." https://www.mpoweruk.com/soh.htm (accessed 2019).
[26] M. Team, "A guide to understanding battery specifications," 2008.

BIOGRAPHIES

ZEKI ZUREY He was born in 1991. He received the B.S. degree in Electrical and Electronics Engineering (EEE) from Gazi University, Ankara, in 2014. He is a graduate student in the department of Karamanoğlu Mehmetbey University EEE. His research interests include power electronics circuits, electric vehicles, hardware design, programming, industrial electronics and agricultural electronics.

KADIR SABANCI He was born in 1978. He received his B.S. and M.S. degrees in Electrical and Electronics Engineering (EEE) from Selcuk University, Turkey, in 2001, 2005 respectively. In 2013, he received his Ph.D. degree in Agricultural Machineries from Selcuk University, Turkey. He has been working as Assistant Professor in the Department of EEE at Karamanoglu Mehmetbey University. His current research interests include image processing, data mining, artificial intelligent, embedded systems and precision agricultural technology.

SELAMI BALCI He received the B.S., M.S. and the Ph.D. degrees in electrical education from the Gazi University, Ankara, in 1997, 2010 and 2016, respectively. Since 2018, he is currently an assistant professor at the faculty of engineering, department of electrical and electronics engineering, Karamanoglu Mehmetbey University. His research interests include medium frequency power transformer, transformer design with the soft magnetic core material, transformer thermal analysis, inductor design, electromagnetic modeling with FEA software, and performance analysis of the power electronics circuits.

ISSN: 2147-284X   http://dergipark.gov.tr/bajece

Implementation of a Microcontroller-Based Chaotic Circuit of Lorenz Equations

Ş. Ç. YENER, R. MUTLU and E. KARAKULAK

Abstract— **Lorenz equations are commonly used in chaos education and studies. Simulation programs can be used to produce solutions of Lorenz equations and to examine its chaotic waveforms. However, sometimes a chaotic signal source can be needed. Such a circuit can be made using either analog or digital circuit components. Recently, a microcontroller-based circuit is suggested to obtain chaotic waveforms of Lorenz equations however only simulations are used to show proof of concept. Such a circuit needs experimental verification. In this paper, implementation and experimental verification of the microcontroller-based circuit which solves Lorenz equations in real-time and produces its chaotic waveforms are presented. Runge-Kutta method is used to solve the equation system. By using Proteus, the microcontroller-based chaotic circuit is simulated and designed. The presented design has been implemented using an Arduino Mega 2560 R3 microcontroller. The microcontroller sends the chaotic signals to the outputs of the circuit using digital-to-analog converters. The waveforms acquired experimentally from the implemented circuit match well with those obtained from Proteus simulations.**

Index Terms— **Chaotic circuits, Lorenz Equations, microcontroller based circuit implementation, Runge-kutta method**

I. INTRODUCTION

THE LORENZ system is a set of ordinary differential equations first studied by Edward Lorenz in 1963 [1]. The equation system can have chaotic solutions for a range of system parameter values. The Lorenz system is commonly used for chaos education and studies. The Lorenz equations can also be used to describe models for dynamos, BLDC electrical machines, electronic circuits, lasers, chemical processes, and osmotic instability [2]–[6]. The Lorenz system has strange attractors, i.e. some of its solutions presented in the phase plane look like number eight or a butterfly [7]–[9].

Analog circuit implementations of Lorenz system can be used for secure communications and cryptography [7], [9]–[14]. MOS realization of a Modified Lorenz Chaotic Systems is given in [14]. Memristor is also a promising circuit element for both analog and chaotic circuit applications thanks to its non-linear dynamics [15]–[19]. Programmable memristor-based chaotic systems can be found in [18], [20]–[22]. A full CMOS based memristive chaotic circuit is examined in [18] and made using a microcontroller-based circuit in [23]. In such a circuit, the chaos waveforms are obtained in a hybrid way not just in an analog way and the effect of different numerical solution methods such as Euler and Runge-Kutta on the bifurcation of the Lorenz system can be investigated easily [23]. This method is also applicable to the Lorenz system and the approach is presented only using simulations in [24]. However, experimental verification of the microcontroller-based circuit has not been done yet. In this paper, a microcontroller-based chaotic circuit of Lorenz equations is implemented. The circuit is made using cheap, rugged, easy-to-use components such as microcontroller Arduino Mega 2560 R3 microcontroller, two DAC0808 digital to analog converters, two LM 741 Opamps, and with a few passive components. The microcontroller solves the Lorenz equation system differential equations numerically and sends two of the solved state-variables out as binary numbers throughout the digital ports to the DACs and, then using the DACs and the opamp-based inverting amplifiers, obtains their waveforms.

To do this, first, the microcontroller-based circuit of Lorenz system is simulated with Proteus™. Some experience about chaotic waveforms is gained from the simulations and used to scale the state variables by adjusting the gains or the program constants. Then, the experimental circuit is assembled using cheap off-the shelves components on a breadboard and its chaotic waveforms in the time domain are obtained experimentally.

The remainder of this paper is organized as follows. The Lorenz equations are briefly told in the second section. The microcontroller-based circuit of Lorenz System is introduced, the circuit is simulated with Proteous™, and its time-domain waveforms and phase portraits are given in the third section. Its experimental results are given in the fourth section. The conclusions are given in the final section.

ŞUAYB ÇAĞRI YENER, is with Electrical and Electronics Engineering Department, Sakarya University, 54187, Sakarya, TURKEY, Turkey,(e-mail:syener@sakarya.edu.tr).

https://orcid.org/0000-0002-6211-3751

REŞAT MUTLU, is with Electronics and Communication Engineering Department, Namık Kemal University, Çorlu, Tekirdağ, TURKEY, (e-mail:rmutlu@nku.edu.tr).

https:// orcid.org/0000-0003-0030-7136

ERTUĞRUL KARAKULAK, is with Vocational school of Technical Sciences, Namık Kemal University, Tekirdag, TURKEY, (e-mail: ekarakulak@nku.edu.tr).

https://orcid.org/0000-0001-5937-2114

REŞAT MUTLU, is with Department o

II. LORENZ EQUATIONS

The following set of equations describes the Lorenz equations/system:

$$\frac{dx}{dt} = \sigma\left(y - x\right)$$

$$\frac{dy}{dt} = x\left(\rho - z\right) - y \qquad (1)$$

$$\frac{dz}{dt} = xy - \beta z$$

where x, y and z are the state variables, t is time. σ, ρ, and β are the Lorenz system parameters.
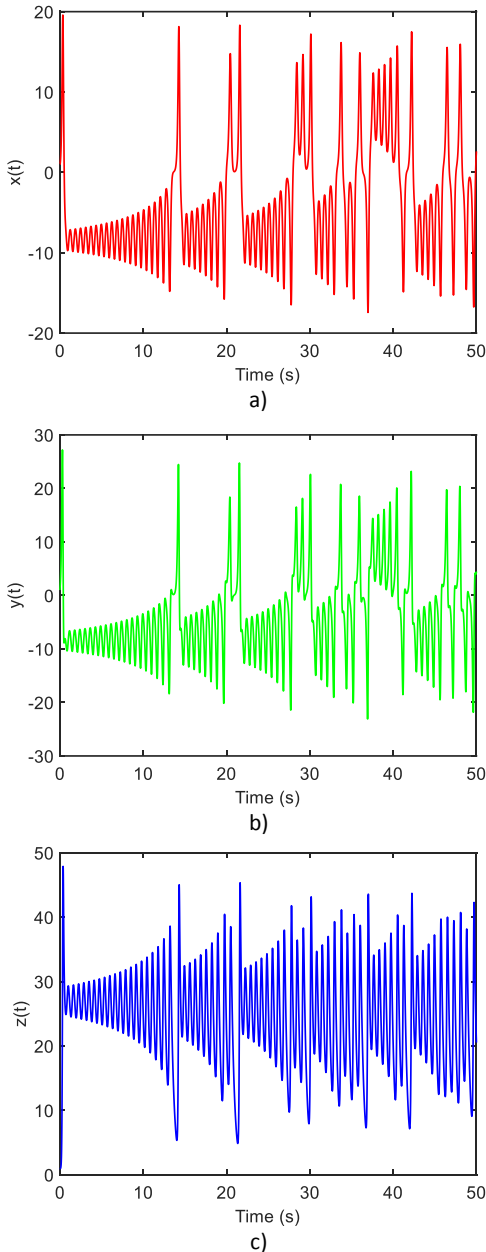
Fig. 1. State variables with respect to time for σ = 10, ρ = 28 and β = 8/3: a) x(t), b) y(t), and c) z(t).

The system parameters are normally assumed to be positive. The Lorenz equations show chaotic behavior for σ = 10, ρ = 28 and β = 8/3. The parameter values are also used in this

study.

The Lorenz system is simulated in Simulink™ toolbox of MATLAB ™ using Runge-Kutta method in the time domain and the results are shown in Fig. 1, Fig. 2, Fig. 3.
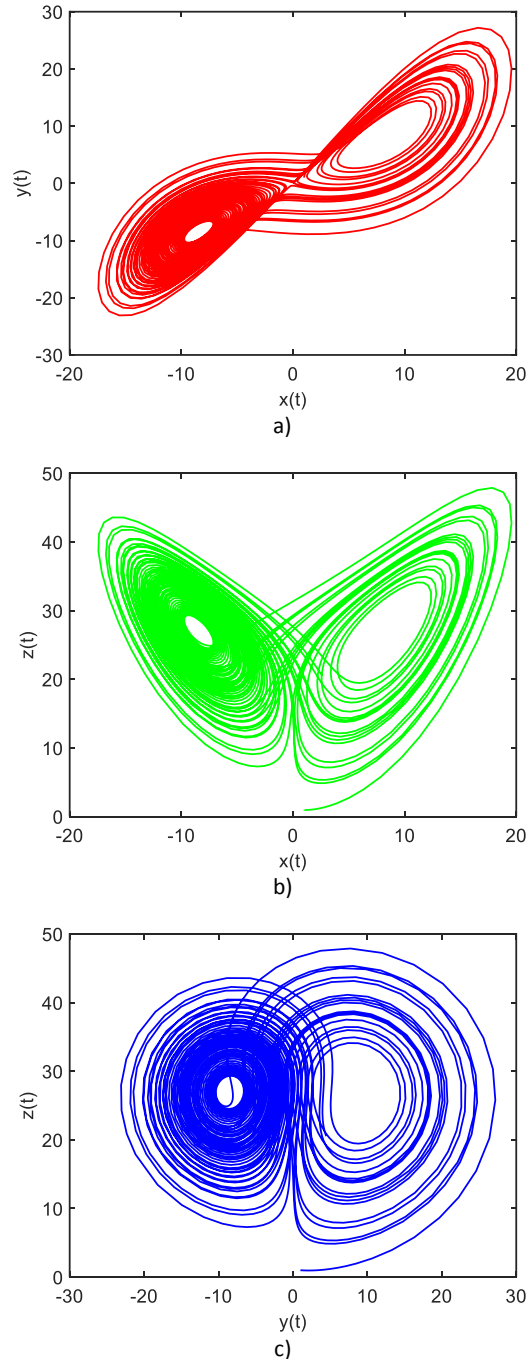
Fig. 2. Chaotic attractors obtained by Simulink simulation of the chaotic circuit equations for σ = 10, ρ = 28 and β = 8/3: a) y(t) vs. x(t), b) z(t) vs. x(t), and c) z(t) vs. y(t).

     http://dergipark.gov.tr/bajece
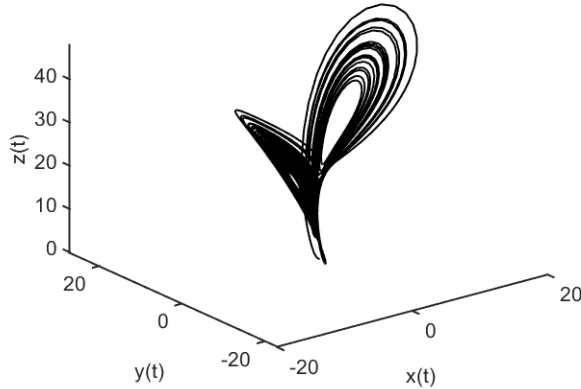
Fig. 3. Three-dimensional chaotic attractor view from Simulink simulation for σ = 10, ρ = 28 and β = 8/3.

III. MICROCONTROLLER-BASED CHAOTIC CIRCUIT AND ITS PROTEUS SIMULATIONS

In this section, Proteus^{TM} schematic of the microcontroller-based circuit of Lorenz system shown in Figure 1 is given. The circuit is made of an Arduino Mega 2560 R3 microcontroller, two DAC0808 digital to analog converters (DACs), and two LM741 Op-amp-based inverting amplifiers. State variables of the Lorenz equations, x, y, and z are solved numerically using Runge-Kutta method, only two of the state variables selected previously can be sent throughout the digital outputs to the DACs by the microcontroller due to the number of digital ports of the microcontroller. The circuit is simulated in Proteus. At the output of the inverting amplifiers fed by the DACs, the selected state-variables are obtained in time-domain as shown in Fig. 4. The output waveforms of the microcontroller-based chaotic circuit in the time domain are obtained from the Proteus simulations and they are shown in Fig. 5. Phase-portrait waveforms of the circuit are not given because of space considerations.
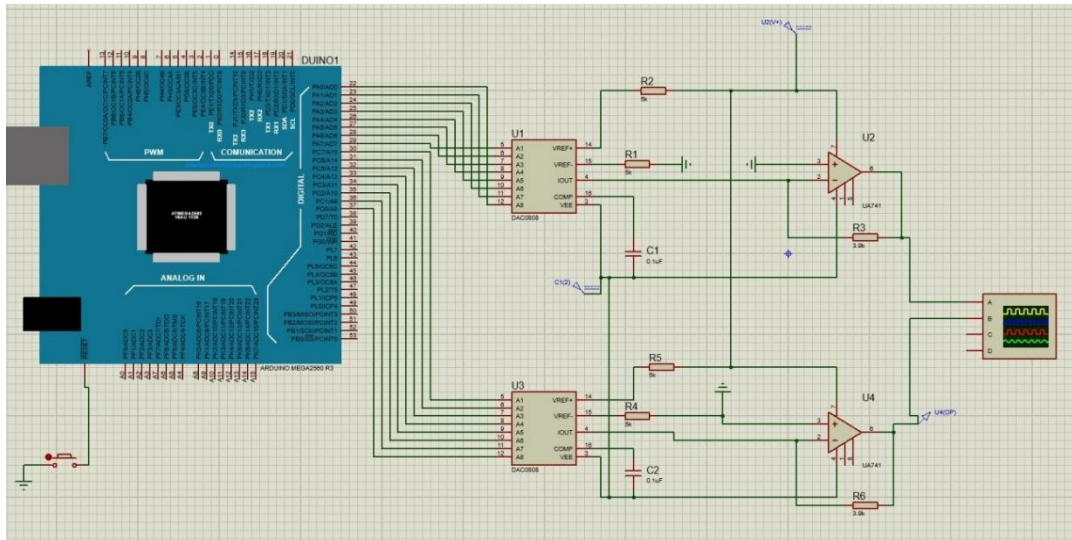
Fig. 4. Circuit schematic of the microcontroller-based circuit of Lorenz System drawn in Proteus.

IV. EXPERIMENTAL RESULTS

The experimental results of the circuit are given in this section. The circuit shown in Fig. 4 is assembled and a photograph of the implemented circuit is given in Fig. 6. Experimental waveforms are acquired by a 60 MHz digital oscilloscope simultaneously. The experimental waveforms and strange attractors which are obtained during chaotic operation are presented respectively in Fig. 7 and Fig. 8. The microcontroller-based chaotic system of Lorenz equations is clearly able to demonstrate chaotic behavior and its waveforms resemble well results of the computer simulations

as seen in Fig. 1, and Fig. 5. The butterfly shape of the strange attractors is also presented in Fig. 2.
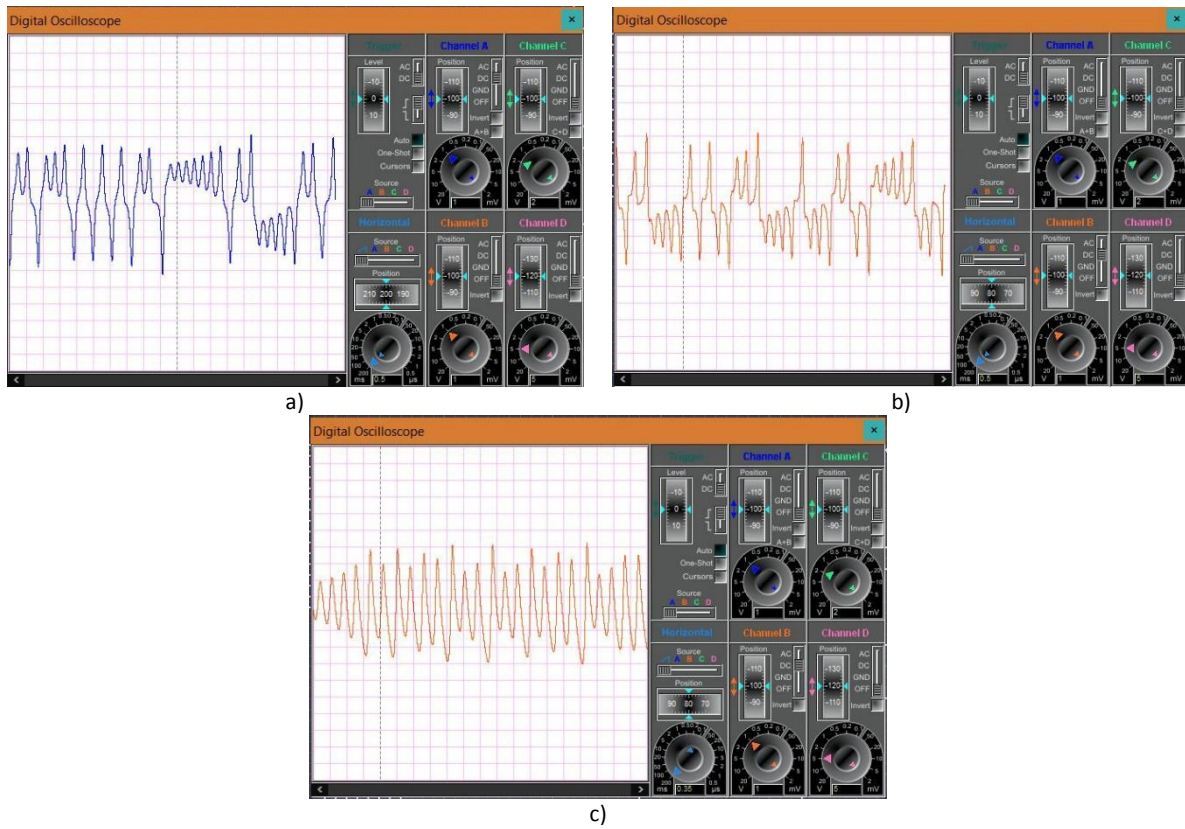
Fig. 5. Time domain waveforms of the microcontroller-based circuit obtained from the Proteus simulations: a) x(t), b) y(t) and c) z(t).
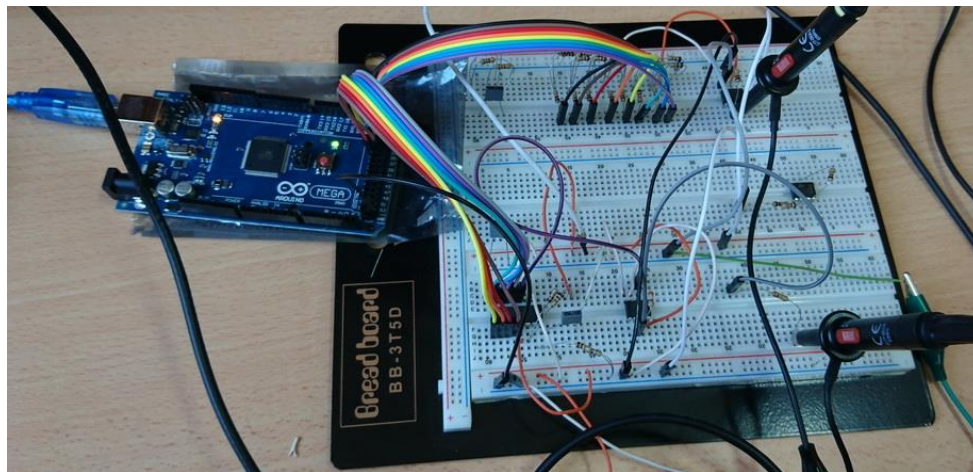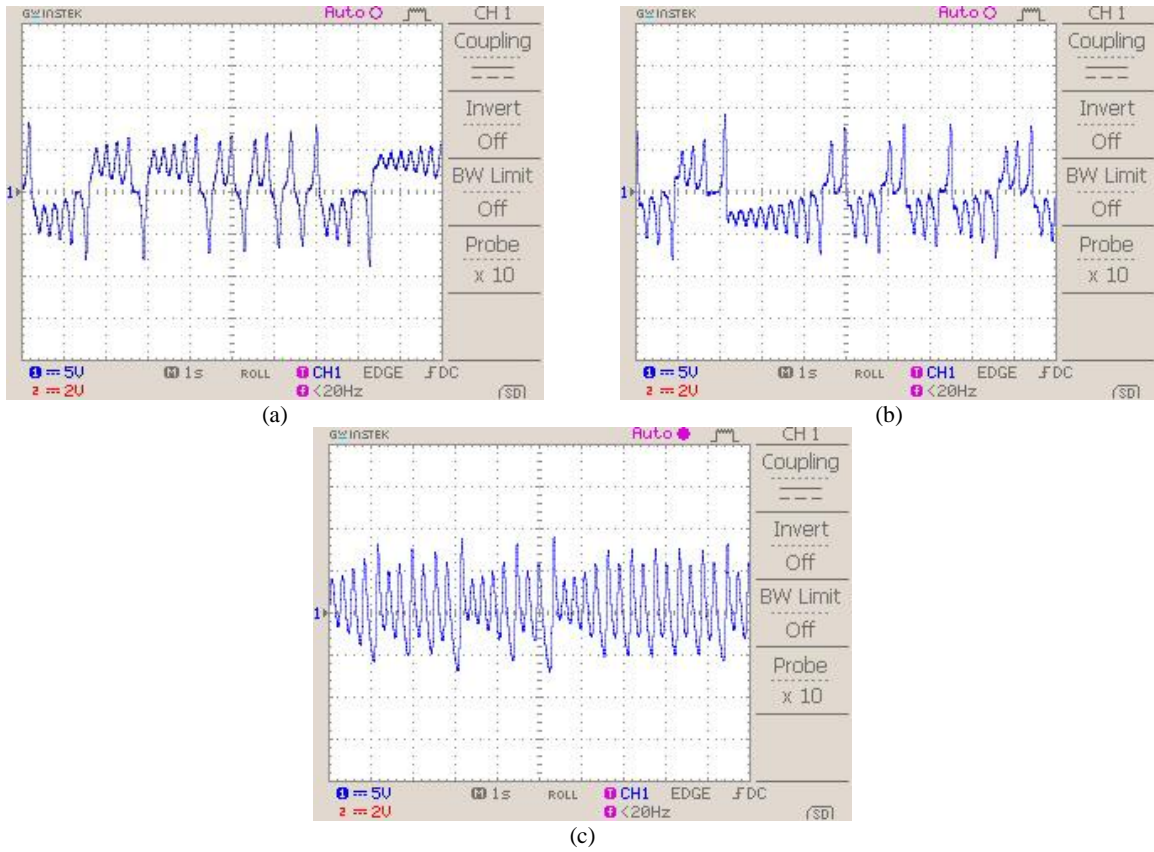

Fig. 6. Photograph of the implemented circuit.

(a)

(b)

(c)

Fig. 7. Chaotic time domain waveforms: a) x, b) y and c) z versus time.
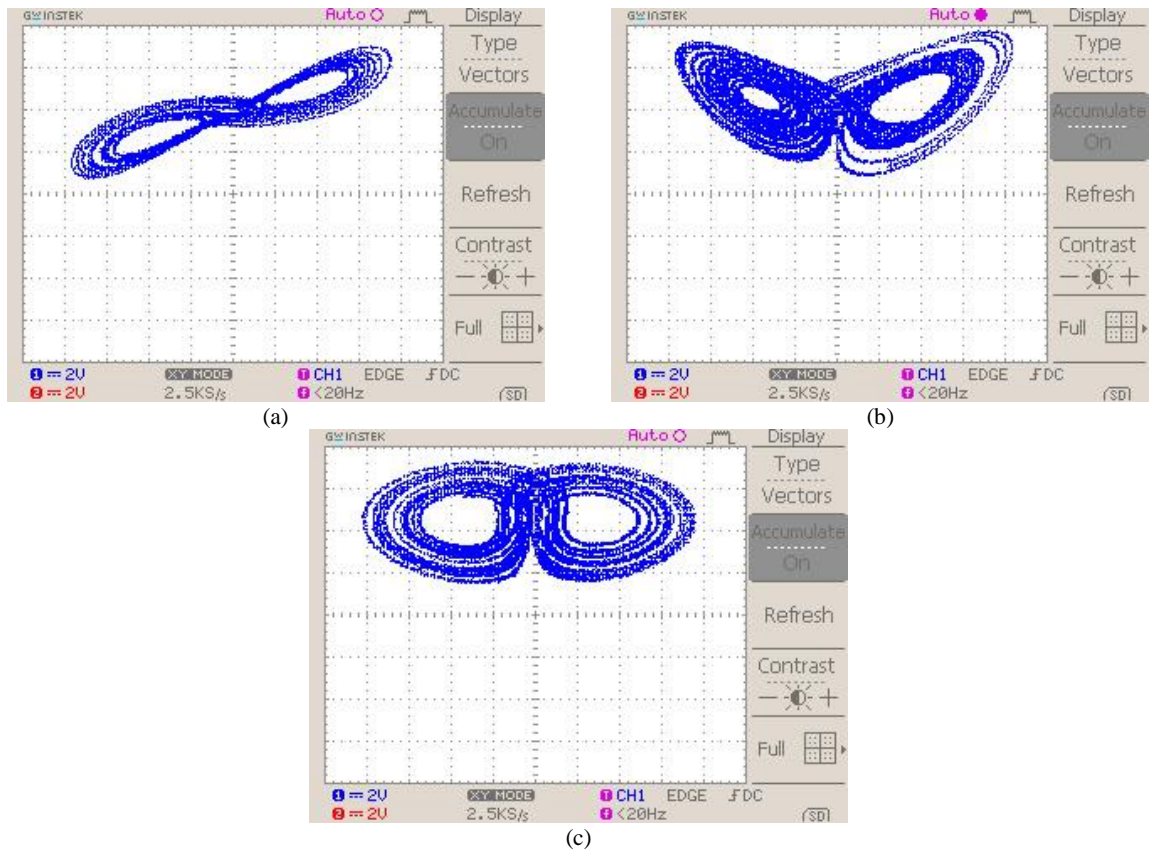

(a)

(b)

(c)

Fig. 7. Strange attractors obtained by experiments: a) x versus y, b) x versus z, and c) y versus z.

V. CONCLUSION

In this paper, an Arduino Mega 2560 R3 microcontroller-based circuit of Lorenz system is designed. The circuit is able to form chaotic signals of Lorenz equations at the outputs of its inverting amplifiers. If its program is modified properly to adjust the Lorenz system parameters perhaps by using potentiometers connected to analog inputs of the microcontroller, their effect on its chaotic behavior can be investigated easily. Such a circuit which is made of off-the shelves components can be used for educational and research purposes.

REFERENCES

[1]   E. N. Lorenz and E. N. Lorenz, "Deterministic Nonperiodic Flow," J. Atmos. Sci., vol. 20, no. 2, pp. 130–141, Mar. 1963.
[2]   H. Haken, "Analogy between higher instabilities in fluids and lasers," Phys. Lett. A, vol. 53, no. 1, pp. 77–78, May 1975.
[3]   E. Knobloch, "CHAOS IN THE SEGMENTED DISC DYNAMO," Phys. Lett., vol. 82A, no. 9, pp. 439–440, 1981.
[4]   N. Hemati, "Strange attractors in brushless DC motors," IEEE Trans. Circuits Syst. I Fundam. Theory Appl., vol. 41, no. 1, pp. 40–45, 1994.
[5]   D. Poland, "Cooperative catalysis and chemical chaos: a chemical model for the Lorenz equations," Phys. D Nonlinear Phenom., vol. 65, no. 1–2, pp. 86–99, May 1993.
[6]   S. I. Tzenov, "Strange Attractors Characterizing the Osmotic Instability," Jun. 2014.
[7]   K. Cho and T. Miyano, "Chaotic cryptography using augmented lorenz equations aided by quantum key distribution," IEEE Trans. Circuits Syst. I Regul. Pap., vol. 62, no. 2, pp. 478–487, Feb. 2015.
[8]   X. Zhang and Y. Qi, "Design of an assemble-type fractional-order unit circuit and its application in Lorenz system," IET Circuits, Devices Syst., vol. 11, no. 5, pp. 437–445, Sep. 2017.
[9]   S. H. Strogatz and A. V. Oppenheim, "Synchronization of Lorenz-Based Chaotic Circuits with Applications to Communications," IEEE Trans. Circuits Syst. II Analog Digit. Signal Process., vol. 40, no. 10, pp. 626–633, 1993.
[10] M. Kaur and V. Kumar, "Efficient image encryption method based on improved Lorenz chaotic system," Electron. Lett., vol. 54, no. 9, pp. 562–564, May 2018.
[11] K. M. Cuomo and A. V. Oppenheim, "Circuit implementation of synchronized chaos with applications to communications," Phys. Rev. Lett., vol. 71, no. 1, pp. 65–68, Jul. 1993.
[12] J. N. Blakely, M. B. Eskridge, and N. J. Corron, "A simple Lorenz circuit and its radio frequency implementation," Chaos An Interdiscip. J. Nonlinear Sci., vol. 17, no. 2, p. 023112, Jun. 2007.
[13] O. A. Gonzales, G. Han, J. P. de Gyvez, and E. Sanchez-Sinencio, "Lorenz-based chaotic cryptosystem: a monolithic implementation," IEEE Trans. Circuits Syst. I Fundam. Theory Appl., vol. 47, no. 8, pp. 1243–1247, 2000.
[14] A. G. Radwan, A. M. Soliman, and A. El-Sedeek, "MOS realization of the modified Lorenz chaotic system," Chaos, Solitons & Fractals, vol. 21, no. 3, pp. 553–561, Jul. 2004.
[15] S. C. Yener, R. Mutlu, T. Yener, and H. H. Kuntman, "Memristor-based timing circuit," in 2017 Electric Electronics, Computer Science, Biomedical Engineerings' Meeting, EBBT 2017, 2017, pp. 1–3.
[16] Y. Babacan, A. Yesil, and F. Gul, "The Fabrication and MOSFET-Only Circuit Implementation of Semiconductor Memristor," IEEE Trans. Electron Devices, vol. 65, no. 4, pp. 1625–1632, Apr. 2018.
[17] C. P. Uzunoglu, Y. Babacan, F. Kacar, and M. Ugur, "Modeling and Suppression of Chaotic Ferroresonance in a Power System by Using Memristor-based System," Electr. Power Components Syst., vol. 44, no. 6, pp. 638–645, Apr. 2016.
[18] Ş. Ç. Yener and H. H. Kuntman, "Fully CMOS memristor based chaotic circuit," Radioengineering, vol. 23, no. 4, 2014.
[19] erdem uçar, ertuğrul karakulak, and reşat mutlu, "ANN Circuit Application of Complementary Resistive Switches," Balk. J. Electr. Comput. Eng., vol. 7, no. 1, pp. 34–43, Jan. 2019.
[20] A. YESIL and Y. BABACAN, "Implementation of Electronically Controllable Memristor Based Chua Circuit," J. Inst. Sci. Technol., vol. 9, no. 1, pp. 121–129, Mar. 2019.
[21] S. Arık and R. Kılıç, "RECONFIGURABLE HARDWARE PLATFORM FOR EXPERIMENTAL TESTING AND VERIFYING OF MEMRISTOR-BASED CHAOTIC SYSTEMS," J. Circuits, Syst. Comput., vol. 23, no. 10, p. 1450145, Dec. 2014.
[22] F. R. Tahir, R. Ali, and L. Fortuna, "ANALOG PROGRAMMABLE ELECTRONIC CIRCUIT-BASED CHAOTIC LORENZ SYSTEM," Basrah J. Eng. Sci., vol. 14, no. 1, 2014.
[23] S. C. Yener, C. Barbaros, R. Mutlu, and E. Karakulak, "Implementation of Microcontroller-Based Memristive Chaotic Circuit," Acta Phys. Pol. A, vol. 132, no. 3–II, pp. 1058–1061, 2017.
[24] Ş. Ç. Yener, C. Barbaros, R. MUTLU, and E. Karakulak, "Design of a Microcontroller-Based Chaotic Circuit of Lorenz Equations," in International Conference on Science and Technology ICONST 2018 5-9 September 2018 Prizren - KOSOVO, 2018, pp. 612–615.

BIOGRAPHIES

ŞUAYB ÇAĞRI YENER was born in Sakarya, Turkey in 1982. He received B.Sc. degree from Sakarya University in Electrical and Electronics Engineering in 2004, M.Sc. and Ph. D. degree from Istanbul Technical University in Electronics and Communication Engineering in 2007 and 2014, respectively. He is currently an associate professor in Sakarya University. His main research interests are circuit design and electronic device modeling, electromagnetic compatibility, memristor-based circuits. He is the author or the co-author of more than 70 journal papers published or papers presented in national/international conferences.

REŞAT MUTLU was born in Tekirdağ, Turkey in 1973. He received B.Sc. degree from Yıldız Technical University in Electrical Engineering in 1995 and M.Sc. and Ph.D. degree from Rensselaer Polytechnic Institute in Electric Power Engineering in 1998 and 2004, respectively. He is currently an associate professor at Electronics and Telecommunication Engineering Department, Namik Kemal University, Tekirdag, Turkey. His main research interests are modeling of memristor and memristive systems, analog and computer memory applications of memristive systems, analysis and, modeling of memcapacitors, the teaching of the memristive systems.

ERTUĞRUL KARAKULAK was born in Tekirdağ, Turkey in 1979. He received B.Sc. degree from Sakarya University in Electronics Education in 2001, M.Sc degree in 2005 and Ph.D. degree from Trakya University in 2016. He is currently an assistant professor at the Electronics Department, Vocational School of Technical Sciences, Namik Kemal University. His research interests include memristor, resistive RAMs and microcontrollers.

Publication Ethics

The journal publishes original papers in the extensive field of Electrical-electronics and Computer engineering. To that end, it is essential that all who participate in producing the journal conduct themselves as authors, reviewers, editors, and publishers in accord with the highest level of professional ethics and standards. Plagiarism or self-plagiarism constitutes unethical scientific behavior and is never acceptable.

By submitting a manuscript to this journal, each author explicitly confirms that the manuscript meets the highest ethical standards for authors and coauthors

The undersigned hereby assign(s) to *Balkan Journal of Electrical & Computer Engineering* (BAJECE) copyright ownership in the above Paper, effective if and when the Paper is accepted for publication by BAJECE and to the extent transferable under applicable national law. This assignment gives BAJECE the right to register copyright to the Paper in its name as claimant and to publish the Paper in any print or electronic medium.

Authors, or their employers in the case of works made for hire, retain the following rights:

1. All proprietary rights other than copyright, including patent rights.
2. The right to make and distribute copies of the Paper for internal purposes.
3. The right to use the material for lecture or classroom purposes.
4. The right to prepare derivative publications based on the Paper, including books or book chapters, journal papers, and magazine articles, provided that publication of a derivative work occurs subsequent to the official date of publication by BAJECE.
5. The right to post an author-prepared version or an of ficial version (preferred version) of the published paper on an i nternal or external server controlled exclusively by t he author/employer, pr ovided that (a) such posting is noncommercial in nature and the paper is made available to users without charge; (b) a copyright notice and full citation appear with the paper, and (c) a link to BAJECE's official online version of the abstract is provided using the DOI (Document Object Identifier) link.

CONTENTS